

**ELECTROMAGNETIC AND STRUCTURAL COMPARISON OF
ULTRA-WIDEBAND ANTENNA RADOMES**

By

Bradley Michael Schroeder

Submitted to the graduate degree program in Aerospace Engineering and the Graduate Faculty of the University of Kansas in partial fulfillment of the requirements for Master's Degree

Chairperson: Dr. Emily Arnold

Dr. Richard Hale

Dr. Mark Ewing

Date Defended: 23 July 2020

The Thesis Committee for Bradley M. Schroeder certifies that this is the approved version of the following thesis:

**ELECTROMAGNETIC AND STRUCTURAL COMPARISON OF
ULTRA-WIDEBAND ANTENNA RADOMES**

Chairperson: Dr. Emily Arnold

Date Approved: 23 July 2020

Abstract

This work examines the electrical performance of a series of dielectric radome panels whose thickness is determined from a set of common loads. Specifically, existing radome designs on NASA's Gulfstream V (GV) aircraft are used for sizing to derive radomes sized with fiberglass and quartz using both monolithic and sandwich designs. The radome fairings currently on NASA's GV are primarily fabricated from S-2 glass/epoxy and include a small vent panel for mounting a 2 – 18 GHz Snow Radar antenna and a new outer moldline fairing for two MCoRDS antennas next to the Snow Radar antenna. A 2 – 18 GHz Ultra-Wideband (UWB) Snow Radar is particularly sensitive to the design of its protective radome due to its microwave operating frequencies. Though the Snow Radar horns are only located over the small vent covers, the MCoRDS panels are also analyzed over the 2 – 18 GHz range to provide a wider sampling of thicknesses. The goal of this work is to examine the existing and alternative radome designs for this UWB radar system to examine the system's electrical performance in the 2 – 18 GHz band and determine if the electrical performance improvements justify the added cost of designing radomes with quartz over S2-glass fibers.

Structural finite element analysis is performed to determine new laminate designs for each of the panel solutions. While the mechanical properties of the S2-glass/epoxy material are widely available, information regarding the quartz material is limited to manufacturer provided properties. Given that these quartz properties are not equally conservative to those used for S2-glass, a mechanical testing program is conducted. A small amount of quartz material was donated for this project; however, the material was beyond its shelf-life. Regardless, the material testing provides a possible lower bound on the mechanical properties, acknowledging that the amount of material provided allowed for an insufficient sample size for a proper statistical analysis of potential process variables. The tested coupon tensile strength and Young's modulus is ~70% and ~75%, respectively, of the provided manufacturer data. Given the high levels of delamination found in the failed coupons (indicating poor resin flow), it is assumed that the tested

mechanical properties are, in fact, conservative. The tested and manufacturer properties are both used in the sizing of the panels to provide bounds for the quartz panel solutions.

Following the structural sizing the electrical performance of each new radome design is determined through theoretical analysis using the Boundary Value Problem (BVP) approach. The theoretical transmissivity calculated using the BVP is verified through anechoic chamber measurements. The electrical testing performed for this analysis demonstrates the validity of using the BVP method for preliminary analysis for radome designs. Data collected from anechoic chamber testing shows good agreement with the overall transmissivity response determined by the BVP solution. In general, the BVP is capable of determining the electrical performance of a potential radome structure within 1 dB. Discrepancies between the BVP solution and the measurements are primarily attributed to the small size of the test panels and their close proximity to the antenna.

For the thinner vent cover design, the sandwich S2-glass exhibits the best performance with near unity transmissivity over the 2 – 12 GHz range. This represents the best UWB performance across all panels. As compared to the monolithic S2-glass and quartz designs, the sandwich S2-glass has upwards of ~2.5 dB and ~1.5 dB, respectively, improvement at some frequencies. The sizing of the MCoRDS radomes showed a thicker laminate is better suited for narrow band applications, for this instance in the Ku – band (8 – 12 GHz). The sandwich quartz panel has comparable transmissivity to the S2-glass sandwich over the 8 – 12 GHz band, however, the frequency band is shifted downward by about 1 GHz. Outside of the 8 – 12 GHz band, the quartz panel has ~ 1 dB improvement over the S2-glass panels (-1.5 dB vs. -2.5 dB).

Given the significantly higher cost for the quartz and the relatively good electrical performance of the S2-glass sandwich design, the fiberglass sandwich design is recommended for 2 – 18 GHz radomes. The thin sandwich design has near unity transmissivity in the 2 – 12 GHz band, and is the closest to providing UWB performance over the band of interest. In general, the quartz sandwich design only shows modest improvements over a S2-glass sandwich design. For 2 – 18 GHz applications, these results suggest it would be better to design a smaller footprint with a thinner sandwich structure that is bound by stiffeners

than to design a thicker sandwich without stiffeners. More specifically a symmetric sandwich made from four surface layers of S2-glass and core is recommended for the 2 – 18 GHz band.

Acknowledgements

I would like to thank my committee for their guidance through this testing. I appreciate their willingness to be on my committee and their generosity with their time. Whether in a formal classroom setting or during informal conversations their help was invaluable. I would also like to thank the Multifunctional Structures group of an aerospace OEM for donating the quartz material that made this trade study possible.

I would also like to thank the University of Kansas Civil, Environmental, and Architectural Engineering Department (CEAE) for allowing me to use their lab space and equipment to perform my tensile and compression tests. I would specifically like to thank Tristan Yount and Dr. Matt O'Reilly, a Graduate student and Professor in the CEAE department, respectively, for taking time out of their busy schedules to help perform my mechanical tests. Their help running the test stands was invaluable and allowed me to complete my testing in a timely manner.

I am especially grateful to William Vanskike, a PhD candidate in the KU Aerospace Engineering Department, for allowing me to assist with some of his composite coupon testing. Working with William on his testing provided me with the expertise I needed to be able to setup and perform my own testing.

Lastly, I would like to thank the material manufacturer for providing me with the mechanical properties for the quartz material. This allowed me to determine how the material was supposed to be cured, as well as the ideal material properties to make informed conclusions about the reduced mechanical performance of the material.

Table of Contents

1. Introduction.....	1
1.1. Background and Motivation	1
1.2. Radome Design Considerations	2
1.3. Following Chapter Summary.....	7
2. Mechanical Testing	9
2.1 Tensile Testing of Composite Materials.....	10
2.1.1 S2-glass/epoxy Tension Testing Results to Verify Calibration Testing.....	13
2.1.2 Results of S2-Glass/Epoxy Testing	14
2.1.3 Results of 0° Quartz Tensile Testing	16
2.1.4 Results of 45° Tensile Testing	20
2.1.5 Results of family testing.....	23
2.2. Compression Testing of Quartz Material	25
2.2.1 Results of Compressive Strength Testing	27
2.2.2 Results of Compressive Modulus Testing	28
2.3. Summary of Mechanical Testing	30
3. Structural Application for Quartz Material.....	33
3.1 Overview of the Current GV Designs	33
3.2 Loading Conditions for Structural Sizing.....	37
3.3 Material Properties	38
3.4 Analysis for the RF Transparent Vent Panel	43
3.4.1 Overview of Comparison between Glass and Quartz models	45
3.4.2 Analysis of the OML Carbon Fuselage Panel.....	50
3.4.3 Modifications to RF Transparent Vent Panel	52
3.4.4 Review of the Modified Horn Antenna Bracket.....	54
3.4.5 Review of the Vent Panel Metallic Doublers of the Dielectric Vent Panels	55
3.4.6 Review of Metallic Shims for Dielectric Horn Bracket	57
3.4.7 Results for the Perimeter Bolts of the Modified Designs	58
3.5 Review of the MCoRDS Antenna Radome and Coupling Structure.....	59
3.5.1 Overview of Comparison between Glass and Quartz Radome Designs.....	60
3.5.2 Sizing for the MCoRDS Dielectric Radome Panel	68
3.5.3 Sizing of Rib Structure	69
3.5.4 Perimeter Bolt Loads	70
3.6 Summary of Structural Analysis	72

4.	EM Characterization Using Boundary Value Problem.....	73
4.1	EM Analysis of Representative Panels.....	73
4.2	Theoretical Panel Transmissivity	74
4.3	Anechoic Chamber Measurements.....	78
5.	EM Analysis of Alternate Radome Panel Designs	83
5.1	EM Analysis of the Dielectric Vent Panel Designs.....	83
5.2	EM Analysis for the MCoRDS Radome Panels	86
6.	Conclusions and Recommendations	88
6.1	Conclusions.....	88
6.2	Recommendations and Future Work.....	89
7.	References.....	91
Appendix A.	MTS Calibration Testing.....	A-1
Appendix B.	Additional Results for 0° Testing.....	B-1
Appendix C.	Additional Results for 45° Testing.....	C-1
Appendix D.	Additional Results for 25/50/25 Testing	D-1
Appendix E.	Additional Results for Compression Testing.....	E-1
Appendix F.	Results for Tested Quartz Patran Analysis	F-1
Appendix G.	Results for Reported Quartz Patran Analysis.....	G-1
Appendix H.	Results for Pre-Preg Glass Patran Analysis	H-1
Appendix I.	Results for Sandwich Fiberglass Patran Analysis.....	I-1
Appendix J.	Tested Quartz MCoRDS Patran Analysis	J-1
Appendix K.	Reported Quartz MCoRDS Patran Analysis.....	K-1

List of Figures

Figure 1.1: Illustration of the Reflected and Transmitted Waves [Ref. 13]	3
Figure 1.2: Boundary Value Problem Example Calculations	6
Figure 2.1: Tension Testing Setup	11
Figure 2.2: Front View of Failure Mode for S2-glass/epoxy Coupons -2 (Top) and -3 (Bottom)	14
Figure 2.3: Front View of In-Date S2-glass/epoxy Coupon -1	14
Figure 2.4: Stress – Strain Curves for 0° Coupons	16
Figure 2.5: Side View of 0° Coupons (Coupons Numbered 1 – 5, Left to Right)	17
Figure 2.6: Surface Ply Failure (a, b) and Ultimate Failure (c, d) caused by Induced Bending in the Test Stand	17
Figure 2.7: Shear Stress – Strain Curves for 45° coupons	20
Figure 2.8: Final Failure of 45° Coupons (Coupons Number 1 – 5, Left to Right)	21
Figure 2.9: Failure in 45° Coupons	22
Figure 2.10: Stress - Strain Curves for the 25/50/25 Family Coupons	23
Figure 2.11: Top (a) and Side (b) Views of Failure Modes for 2/50/25 Testing	24
Figure 2.12: Compressive Test Fixture Components (a), Setup Front view (b) and Top View (c) ...	25
Figure 2.13: Side View of Compressive Strength Coupons (0° - left, 25/50/50 – right)	27
Figure 2.14: Strain Gage Setup for Compressive Young’s Modulus Testing	29
Figure 3.1: Location of Fuselage Panels on NASA GV Aircraft (not to scale) [Ref. 24]	34
Figure 3.2: Isometric View of Antenna Assembly on GV Fuselage Panel [Ref. 24]	34
Figure 3.3: Full RF Transparent Vent Panel and Horn Antenna Bracket [Ref. 24]	35
Figure 3.4: Exploded View of the GV Fuselage Fairing Assembly [Ref. 25]	36
Figure 3.5: Comparison of Maximum Deflection [Ref. 24]	45
Figure 3.6: Comparison of Maximum Principal Stress Distribution [Ref. 24]	47
Figure 3.7: Minimum Principal Stress Distribution [Ref. 24]	49
Figure 3.8: Comparison of Total Displacement for Full Assembly based on Load Case 3 [Ref. 25]	61
Figure 3.9: Comparison of Total Displacement of the Radome Panel based on Load Case 3 [Ref. 25]	62
Figure 3.10: MCoRDS Dielectric Radome Maximum Principal Stress for Load Case 3 [Ref. 25] ...	65
Figure 3.11: MCoRDS Dielectric Radome Minimum Principal Stresses for Load Case 3 [Ref. 25].	66
Figure 4.1: Multilayer Dielectric Wall for Boundary Value Analysis [Ref. 13]	75
Figure 4.2: Transmitted Power Produced from the BVP method	77
Figure 4.3: Infographic of the Anechoic Chamber Setup	79
Figure 4.4: Anechoic Chamber Setup	79
Figure 4.5: Time Domain Response	80
Figure 4.6: Peak S12 Response of the Test Results in the Time Domain	80
Figure 4.7: Measured Transmitted Power	81
Figure 5.1: BVP Analysis for Dielectric Ventilation Panel Designs	84
Figure 5.2: BVP Analysis including a Sandwich Quartz Design	86
Figure 5.3: BVP Results for the MCoRDS Sandwich Radomes	87

List of Tables

Table 2.1: Quartz/Epoxy Composite Material Properties [Ref. 20]	10
Table 2.2: Test Level Data for Quartz/Epoxy Composite, as provided by the Manufacturer [Ref. 21]	10
Table 2.3: Final Results of 0° In-Date S2-glass/epoxy Testing	15
Table 2.4: Final Results of 0° Testing	19
Table 2.5: Final Results for Shear Testing	22
Table 2.6: Final Results of Family Testing	24
Table 2.7: Final Results for Compressive Strength Testing	28
Table 2.8: Final Results for Compressive Modulus and Poisson’s Ratio Testing	29
Table 2.9: Final 0° Results	30
Table 2.10: Final 25/50/25 Family Results	31
Table 2.11: Final Shear Results	31
Table 3.1: Inertial Load Factor	37
Table 3.2: Aerodynamic Load Cases	37
Table 3.3: 6781 S-2 Glass/DPL 862 Resin Properties for Wet Layup [Ref. 24, 27]	38
Table 3.4: ACG S2-Glass 6781/MTM45-1 Epoxy Pre-Preg Properties [Ref. 22]	39
Table 3.5: 2024-T3 Aluminum Sheet Properties, RT, QQ-A-250/5 [Ref. 28]	40
Table 3.6: 6061-T6 Aluminum Sheet Properties, RT, QQ-A-200/8 [Ref. 28]	40
Table 3.7: MTM45-1/ 6781 S-2 Glass Properties [Ref. 22]	41
Table 3.8: Quartz Material Properties from Material Testing	42
Table 3.9: Quartz Material Properties as Reported [Refs. 20 and 21]	43
Table 3.10: Rohacell 71 WF Properties [Ref. 29]	43
Table 3.11: Maximum Deflection	46
Table 3.12: Principal Stresses	50
Table 3.13: Critical Stresses and Margins of Safety	51
Table 3.14: Stresses and Margins of Safety of Similar Elements	52
Table 3.15: Critical Stresses and Margins of Safety	52
Table 3.16: Stresses and Margins of Safety for Comparison	54
Table 3.17: Critical Stresses and Margins of Safety for Dielectric Horn Antenna Bracket	55
Table 3.18: Critical Stresses and Margins of Safety for the Metallic doublers	56
Table 3.19: Critical Stresses and Margins of Safety for Comparison of the Metallic doublers	57
Table 3.20: Critical Stresses and Margins of Safety for the Metallic Shims	57
Table 3.21: Critical Margins of Safety for OML Carbon Fuselage Panel	58
Table 3.22: Maximum Displacement for MCoRDS Radome Designs sized using Load Case 3	63
Table 3.23: Maximum Displacement for MCoRDS Radome Designs sized using Load Case 2	64
Table 3.24: Principal Stresses in the MCoRDS Radome Panels sized with Load Case 3	67
Table 3.25: Principal Stresses in the MCoRDS Radome Panels sized with Load Case 2	67
Table 3.26: Critical Stresses and Margins of Safety for the MCoRDS Radome Designs	68
Table 3.27: Critical Stress and Margin of Safety for Comparison	69
Table 3.28: Critical Stresses and Margins of Safety for the Rib Structure	69
Table 3.29: Margins of Safety for Critical Fasteners in Tested Quartz Design under Load Case 2 .	70
Table 3.30: Margins of Safety for Critical Fasteners in Tested Quartz Design under Load Case 3 .	71
Table 3.31: Margins of Safety for Critical Fasteners in Reported Quartz Design under Load Case 2	71

Table 3.32: Margins of Safety for Critical Fasteners in Reported Quartz Design under Load Case 3	71
Table 4.1: Physical Characteristics of Panels Manufactured for Electrical Testing	73
Table 4.2: Electrical Properties for EM Material Trade Study	74
Table 5.1: Ply Thicknesses for Structurally Sized Dielectric Ventilation Panels	83

1. Introduction

1.1. Background and Motivation

Airborne radar applications require radome structures to protect the antenna elements from in-flight loads as well as environmental effects. To optimize antenna performance, radomes are typically made from low-loss, electrically transparent materials such as fiberglass and quartz and are made as thin as possible. However, structural sizing constraints drive the structure's thickness rather than the electrical performance, and structural and electrical requirements often conflict. Drivers of the material selection for radome applications not only include the structural and electrical performance requirements, but also cost, weight, and aerodynamics. As mentioned fiberglass and quartz fiber composites are common materials used for radome fabrication, and while the two materials have comparable mechanical properties, the electrical properties, such as dielectric constant and loss tangent, are much lower for quartz; however, this material costs five times as much as fiberglass, or more, depending on the quality of the glass fiber [Ref. 1]. The high cost of quartz is often prohibitive, except in instances where electrical performance is weighted more than other design requirements.

In this work, the electrical performance of a variety of composite radome panels is assessed, including a variety of designs made from S2-glass and quartz. This work was motivated by the on-going research by the Center for Remote Sensing of Ice Sheets (CReSIS) located at the University of Kansas. CReSIS has developed a series of airborne radar systems used to measure a variety of ice and snow characteristics [Refs. 2, 3]. As part of these radar installations, custom radome structures were required [Refs. 4 – 7]. CReSIS's 2 – 18 GHz Ultra-Wideband (UWB) Snow Radar [Refs. 8, 9] is particularly sensitive to the design of its protective radome due to its microwave operating frequencies. For this reason the electrical analysis in this work will focus on this frequency range.

In 2019, CReSIS flew two missions on NASA's Gulfstream V (GV) as part of the Operation IceBridge (OIB) polar survey program. The radome panels designed for this mission will serve as an example on which the comparative analysis herein was based. In this manner, structural requirements can

be considered in the radome design. The GV installation consisted of both a small dielectric vent cover on which the Snow Radar horn was installed, and a much larger and thicker radome panel on which a lower frequency Multichannel Coherent Radar Depth Sounder (MCoRDS) antenna was installed. While the Snow Radar was only installed over the smaller, thinner dielectric vent cover, both panels are included in this work to examine a range of thicknesses.

There has been on-going interest at CReSIS to use quartz composite materials for UWB microwave radome designs; however, the electrical benefits have never been thoroughly characterized, mechanical properties reported by manufacturers are generally not conservative compared to those used in the designs of fiberglass radomes, and the cost has been too prohibitive to explore the alternate material solutions experimentally. In 2019, the Multifunctional Structures group of an aerospace OEM provided a small amount of material that could be used for experimental characterization; however, this material was past its shelf-life. While the expired nature of the material would not affect the electrical characterization of the material, it would cause a reduction in the mechanical properties. Regardless, the donation of the quartz material provided an opportunity to experimentally characterize the electrical performance of the material and establish a probable lower bound for the mechanical properties of the material via strength testing.

1.2. Radome Design Considerations

Analysis of airborne radome effects on antenna performance has been carried out in the past for both transmitting and receiving antennas [Ref. 10, 11]. The introduction of a radome structure increases the transmission and reflection losses, and distorts the pattern and polarization of the radar system [Ref. 12]. Radomes typically cause transmission loss depending on the construction of the radome (i.e. thickness and material), the antenna look angle, the field distribution over the antenna aperture, the location of the antennas inside the radome, and the radome-to-antenna size ratio [Ref. 10, 11].

The transmissivity and corresponding reflectivity of a radome structure is a measure of both the impedance mismatch between the radome and surrounding environment as well as the lossy nature of the material used in the radome design. For low-loss materials, the loss in the signal is primarily due to reflection of the signal due to impedance mismatches at disparate media boundaries. (i.e. air and fiberglass)

as well as internal and external diffraction, refraction effects and polarization shifts [Ref. 10, 11]. Figure 1.1 is an illustration of the transmitted and reflected waves created at a media boundary.

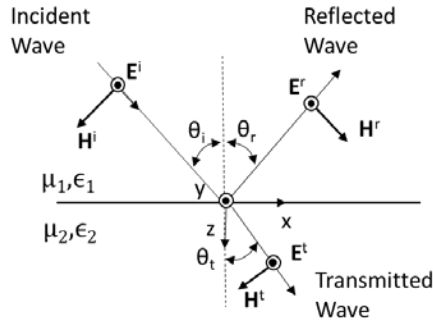


Figure 1.1: Illustration of the Reflected and Transmitted Waves [Ref. 13]

The reflectivity (and transmissivity) for a boundary between two different media is based on the intrinsic impedance shown in Equation (1-1) [Ref. 13].

$$\eta = \sqrt{\frac{j\omega\mu}{\sigma + j\omega\epsilon}} \quad (1-1)$$

Where the intrinsic impedance, η , is a function of the permeability, the angular frequency, and the conduction loss and polarization losses. The permeability (μ), conduction loss (σ) and polarization loss (ϵ) are defined characteristics of the material used in the design of the radome, while the angular frequency (ω) is a characteristic of the radar system. For a dielectric material that is non-conductive and non-magnetic, Equation (1-1) reduces to Equation (1-2) [Ref. 13]:

$$\eta = \sqrt{\frac{\mu_0}{\epsilon_0}} \sqrt{\frac{1}{\epsilon_r}} = \frac{377\Omega}{\epsilon_r} \quad (1-2)$$

Where η is the intrinsic impedance of the radome, while μ_0 and ϵ_0 are the permeability and polarization loss of free space (i.e. air), respectively; and ϵ_r is the permittivity of the material used in the radome design. Across the boundary of two dielectrics the tangential E-field component must be equivalent, while the normal components are related by the ratio of the dielectric constants of the materials as follows [Ref. 13]:

$$E_{1n} = \frac{\epsilon_2}{\epsilon_1} E_{2n} \quad (1-3)$$

Where E_{1n} is the E-field present before the signal interacts with the boundary and E_{2n} is the strength of the E-field propagating out the opposite side of the radome structure. The ϵ values in this equation represent the polarization losses before and after the signal passes through the radome structure (i.e. 1 is before and 2 is after as depicted in Figure 1.1). For the E-field to satisfy both the wave equation and the boundary conditions, the relationship between the incident field and the reflected and transmitted fields are as follows [Ref. 13]:

$$E^r = E^i \frac{\eta_2 - \eta_1}{\eta_2 + \eta_1} \quad (1-4)$$

$$E^t = E^i \frac{2\eta_2}{\eta_2 + \eta_1} \quad (1-5)$$

For Equations (1-4) and (1-5) E^i , E^r , and E^t are the E-field components of the incident, reflected and transmitted waves respectively, while η_1 and η_2 are the intrinsic impedances of the different layers. In the case of Figure 1.1, η_1 is the intrinsic impedance of free space and η_2 is the intrinsic impedance of the boundary layer. From Equations (1-4) and (1-5), the definitions of the reflection and transmission coefficients can be derived [Ref. 13].

$$\Gamma \equiv \frac{E^r}{E^i} = \frac{\eta_2 - \eta_1}{\eta_2 + \eta_1} \quad (1-6)$$

$$T \equiv \frac{E^t}{E^i} = \frac{2\eta_2}{\eta_2 + \eta_1} \quad (1-7)$$

Where Γ (1-6) is the reflection coefficient and T (1-7) is the transmission coefficient. In the case of multiple media boundaries, the reflection and transmission coefficients can be determined by finding the effective impedance. The effective impedance is found by simplifying multilayer designs into a single effective layer and illustrates that the reflectivity is dependent on the radomes impedance and thickness [Ref. 13]. The effective impedance is calculated by Equation (1-8) [Ref.13], which is a function of the intrinsic impedances, thickness of the layers, and the materials propagation constant, γ . (In this equation, the subscripts 2 and 3 illustrate that the effective impedance is being calculated by combining the impedance before and after a layer in the laminate.)

$$\eta_{eff} = \eta_2 \frac{\eta_3 + \eta_2 \tanh(\gamma_2 t)}{\eta_2 + \eta_3 \tanh(\gamma_2 t)} \quad (1-8)$$

In Equation (1-8) the propagation constant, γ , is a function of the polarization and conduction losses, permittivity, and angular frequency of the system, and is determined by Equation (1-9) [Ref. 13].

$$\gamma = \sqrt{j\omega\mu(\sigma + j\omega\epsilon)} \quad (1-9)$$

Once the effective impedance for the entire laminate is determined, the reflection coefficient can be found using Equation (1-10) (a modified version of Equation (1-6)) [Ref. 13], provided the definitions of reflectivity and transmissivity which is the square of the absolute value of the coefficients [Ref. 13].

$$\Gamma = \frac{\eta_{eff} - \eta_1}{\eta_{eff} + \eta_1} \quad (1-10)$$

A Boundary Value Problem (BVP) approach can also be used to determine the reflection at each interface as well as the reflectivity and transmissivity of the panel. The BVP was used to create Figure 1.2, illustrating the difference in percent reflected power of representative thick and thin laminates as well as monolithic and sandwich designs. Each laminate illustrated in Figure 1.2 is made of S2-glass, and the ‘thick’ monolithic and sandwich designs were made with 24 layers with an assumed ply thickness of 0.0101”; while the ‘thin’ monolithic design was analyzed with 12 layers and the ‘thin’ sandwich design was analyzed with four plies of S2 – glass. The sandwich designs included in Figure 1.2 are symmetric sandwich laminate with two and 12 surfaces layers on either side of the core for the four and 24 ply sandwich laminates, respectively.

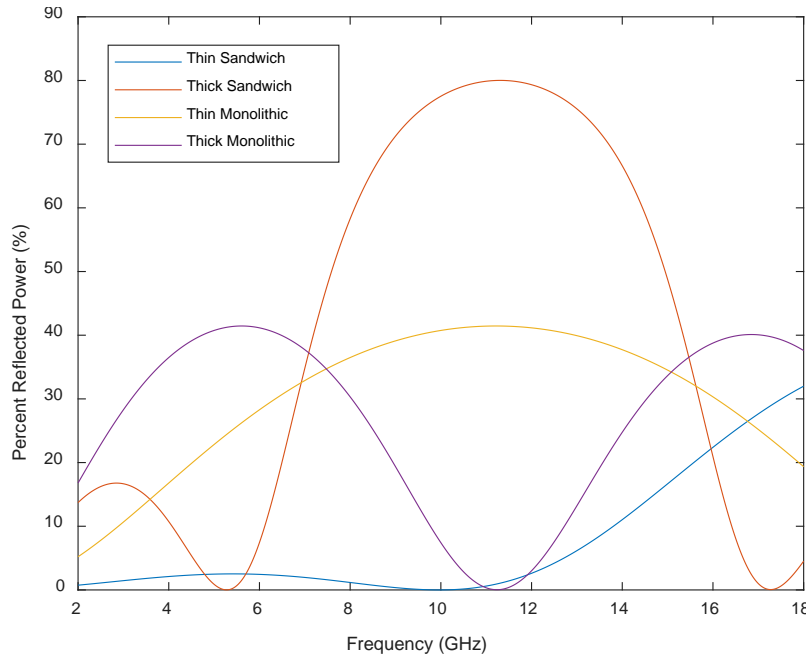


Figure 1.2: Boundary Value Problem Example Calculations

As can be seen from Figure 1.2 it is difficult to design radome structures for UWB applications. This can be seen by the high reflections created for the monolithic designs and the thick sandwich design. These designs only reflected a low percentage of the power over narrow frequency bands, and thus would be more desirable for a frequency selective design, where they would act as a physical filter for unwanted signals [Ref. 11]. Figure 1.2 also illustrates that even though the thin sandwich design produced the most favorable response across the frequency, it still reflects upwards of 30% of the power at high frequencies.

Radome structures can also add errors that degrade the performance of the system which are more prominent in UWB designs given the difficulty in matching across wide frequency bands. The primary types of performance degradation include increased sidelobe levels and radome depolarization [Ref. 12, 14]. Antenna sidelobes generally increase when an antenna is placed within a radome. The increased sidelobe level is caused by distortion and wall transmission effects as a signal propagates through a radome wall [Ref. 14]. Similar distortions will cause the main beam to broaden so the received signal includes more interference which will have to be filtered out of the signal [Ref. 14].

Radome depolarization is a folding of energy from the primary antenna polarization to the other sense. For example, the polarization can switch from left-hand circular to right-hand circular polarization after propagating through the radome. This phenomenon occurs as a result of the radome wall curvature and the difference in complex transmission coefficient between orthogonal polarized vectors [Ref. 14].

Previous research has shown the difficulties associated with designing radome structures for UWB applications due to the required structural performance [Refs. 15 – 17]. Most standard radome designs present high level transmission efficiencies for narrow frequency bands (0.667 GHz) [Ref. 14]. Some active frequency selective surfaces (AFSS) have been designed to try to achieve UWB frequencies by including elements which can be switched off and on depending on the desired operating frequency band [Ref. 15]. However, these active systems present rather complicated designs and are more expensive than passive systems. The designs presented in this document look to find a solution for an UWB (2 – 18 GHz) radome which does not require the complexity of an active system and thus is more cost effective.

1.3. Following Chapter Summary

Chapter 2 provides discussion of the procedures and results of mechanical testing performed to evaluate the mechanical properties of pre-impregnated (pre-preg) quartz/epoxy composite material. Again, the reduced mechanical properties found through the testing of an expired material will provide a more conservative design for the structural sizing of the panels. Chapter 3 provides structural analysis for sizing the modified radome structures based on the design for NASA's GV aircraft. For a complete structural analysis six different designs were analyzed. Four analyses included material substitutions of the existing S2-glass/epoxy dielectric vent panel design for a 2 – 18 GHz horn antenna, while the last two analyses were for the redesign of the dielectric radome panel for the MCoRDS antennas. For the quartz solutions, the panels were sized using both the manufacturer's reported properties as well as the tested properties from Chapter 2 to establish an upper and lower bound for the panel thicknesses. All of the analyses in Chapter 3 were performed using MSC.Patran/NASTRAN 2018 finite element software. Chapter 4 introduces the Boundary Value Problem (BVP) method for analyzing the transmissivity of the various panels. Representative panels are first analyzed using this method, and subsequently fabricated for validation

testing via anechoic chamber testing. After the BVP approach has been validated, it is then used in Chapter 5 to analyze the panel laminates found in Chapter 3. Conclusions and recommendations are presented in Chapter 6.

2. Mechanical Testing

The quartz material used for these mechanical tests was donated to the University of Kansas Aerospace Engineering Department from the Multifunctional Structures group of an aerospace OEM. The following mechanical tests were performed with an understanding that the epoxy resin system of the donated material was expired by two years. This testing performed on a material with an expired resin system is assumed to determine more conservative mechanical properties, as the material properties provided by the manufacturer are ideal properties and the ideal material properties are typically not used when sizing radome structures. Namely the manufacturer data is for an autoclave cure, including the cured ply thickness of 0.0105", and it does not provide data on laminated families, open-hole or filled-hole allowables, or any further stress concentrations from countersinks, pitch or edge distance. By considering both the tested properties and the reported properties the laminate design can be bound. The manufacturer's properties will result in the thinnest laminate possible illustrating the best mechanical and electrical performance of the material, while the properties determined from these tests will result in the most conservative solution, and a panel sized with more appropriate mechanical properties.

Material testing also allowed for determining the strength allowables for a laminate family. The family properties are the properties usually used for structural analysis and material manufacturers typically only report 0° and shear properties because these are more favorable than the family properties. Mechanical tests were performed to determine the properties of a [25/50/25] family as part of this analysis because a [25/50/25] family presents a quasi-isotropic laminate, which is the most common family used by CRISIS. Tensile and shear tests were performed in accordance with ASTM D3039 – 17 [Ref. 18] and ASTM 3518 – 18 [Ref. 19], respectively. This chapter also provides details of any deviations from these testing standards.

The following properties for the quartz material were provided by the manufacturer. The properties listed in Table 2.1 are the material properties listed on the manufacturer's sales brochure [Ref. 20], and

properties listed in Table 2.2 are the ranges determined from the material manufacturer’s own ‘In-House’ testing [Ref. 21]. These properties are the ‘ideal’ properties for this quartz material.

Table 2.1: Quartz/Epoxy Composite Material Properties [Ref. 20]

Property *	Method	Results	
Tensile Strength, 0°	ASTM D3039	834 MPa	121 ksi
Tensile Modulus, 0°	ASTM D3039	27 GPa	3.9 Msi
Compressive Strength, 0°	ASTM D6641	558 MPa	81 ksi
Compressive Modulus, 0°	ASTM D6641	29 GPa	4.2 Msi

- * Data normalized to 60% fiber volume
- * All of the properties listed are RTD properties

Table 2.2: Test Level Data for Quartz/Epoxy Composite, as provided by the Manufacturer [Ref. 21]

Property *	Method	Results
Tensile Strength, 0°	ASTM D3039	112 - 148 ksi
Tensile Modulus, 0°	ASTM D3039	4.0 - 4.4 Msi
Compressive Strength, 0°	ASTM D6641	86 - 110 ksi
Compressive Modulus, 0°	ASTM D6641	4.4 - 4.9 Msi
Short Beam Shear Strength	ASTM D3518	10.6 - 11.0 ksi
Per Ply Thickness	-	0.0105”

- * Data normalized to 60% fiber volume
- * All of the properties listed are RTD properties
- * 10 - 0° Ply layup
- * Cure:3-5°F/MIN to 350°F/ 2.0-2.5 hrs/85-100 psi (Autoclave Cure)

As mentioned the coupons used to determine the properties listed in Table 2.2, were cured using an autoclave [Refs. 20, 21], while the coupons used to produce the results presented in Sections 2.1 and 2.2 were cured using an oven cure cycle recommended by the material manufacturer [Ref. 20]. Regardless, materials cured using an oven provide reduced material properties from material cured in an autoclave due to changes in fiber volume and cured ply thickness. It should be noted that the properties found in this Chapter are expected to be lower than oven cured properties of in-date material. None-the-less, the testing of this material provided a probable lower bound for the quartz panel solution.

2.1 Tensile Testing of Composite Materials

The following sections will discuss the results of tensile testing of the quartz material. Tensile test were performed using an MTS Landmark test stand provided by the KU Civil, Environmental, and

Architectural Engineering Department (CEAE). The coupons were loaded until failure while the test stands control computer collected the necessary load data. Although the test stand also recorded cross-head displacement, linear strain gauges were installed on the coupons in both the longitudinal and lateral directions. The longitudinal strain and load data was used to calculate the materials tensile modulus, while the strain data from both the longitudinal and lateral strain gauges were used to calculate the Poisson's ratio. The strain data was also used to monitor the flexure in each coupon; this is why each coupon was equipped with strain gauges on both surfaces. Figure 2.1 shows the test setup for the tensile tests performed to determine the mechanical properties of the quartz material.

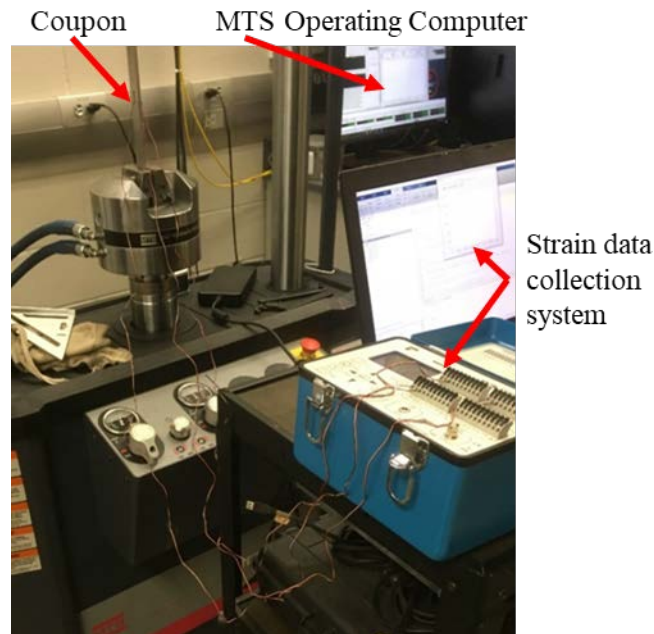


Figure 2.1: Tension Testing Setup

Before the quartz material could be tested calibration tests were performed with a 5052-H32 aluminum coupon. For calibration, the coupon was setup to measure the Young's modulus for the aluminum; the setup is described in Reference 18. The calibration tests showed flexure in two directions including an average bending of 1.3% about the y-axis (width axis) and 0.85% about the z-axis (thickness axis), while also showing an average 3% reduction in the Young's modulus of the 5052-H32 aluminum. According to ASTM D3039 – 17 bending may not exceed 5%. The flexure was assumed to result from slight misalignment of the grip heads as an inclinometer was used on each coupon to ensure they were

properly aligned. The 3% reduction in the stiffness was assumed to be a result of the expired calibration of the test stands force transducer. Results of the calibration tests are included in Appendix A.

After calibration testing was performed the following properties were evaluated for the quartz material:

1. Ultimate strength (0°)
2. Young's Modulus (0°)
3. Poisson's Ratio (0°)
4. Family Ultimate strength (25/50/25)
5. Family Young's Modulus (25/50/25)
6. Family Poisson's Ratio (25/50/25)
7. Shear Modulus (45°)
8. Ultimate Shear Strength (45°)
9. Yield Shear Strength (45°)

Three types of coupons were manufactured in accordance with the aforementioned testing standards and include: five – 0° coupons, five – 45° coupons, and five – 25/50/25 family coupons. Each property was studied independently for each set of coupons to provide a full overview of the materials capabilities. Tests 1 – 3 and 4 – 6 were used to determine the longitudinal and transverse properties for the lamina and family laminates, respectively, while tests 7 – 9 were used to determine the shear properties of the lamina. The shear properties are included as part of the tensile testing results because these tests follow the same procedure as the 0° and family tests [Ref. 18, 19]. The only differences between the following tensile and shear tests are the calculations of the final results.

Reference 18 recommends the tensile testing coupons be 10" long, 1" wide, and 0.10" thick. Based on the coupon sizing outlined in References 18 and 22 the coupon length and width should be maintained but the thickness is dependent on the specific test being performed. Following the laminate design in Reference 22 each coupon was manufactured 12 layers thick. This ideally resulted in a laminate thickness of 0.126"; slightly thicker than the recommended minimum thickness of 0.10", based on a cured ply thickness of 0.0105" for the quartz material [Refs.20 and 21].

The thickness of each coupon was thicker than the assumed 0.126" due to the expired resin system and its inability to flow properly, so a new cured ply thickness was calculated for each set of coupons. The

average cured ply thicknesses for the 0°, 45°, and 25/50/25 family coupons were 0.0118”, 0.0117”, and 0.0114”, respectively. These new thicknesses were considered acceptable because the driving factor in the design of the coupons was the 12 layer design from Reference 22, and Reference 18 allows for varying of the coupon thickness to fit the desired test conditions. The new cured ply thicknesses were used to calculate the final material properties reported in Sections 2.2 and 2.3, and the average cured ply thickness for the family coupons was used in the structural analysis in Chapter 3. The average dimensions for each set of coupons is included in Appendices B – D, and the actual dimensions of the coupons were utilized to determine the mechanical properties of the materials.

2.1.1 S2-glass/epoxy Tension Testing Results to Verify Calibration Testing

To provide an additional assessment of the calibration of the test stand, in-date MTM45-1/6781 S2 fiberglass coupons were tested. This provided insight into the failure response of a composite material as well.

The S2-glass/epoxy coupons were manufactured and tested following the same procedure as outlined for testing of the quartz material, with a 0° fiber orientation. S2-glass/epoxy with an in-date resin system was tested to find the ultimate strength and Young’s modulus and the results were compared to the ‘Warp (0°) Tension Properties’ reported in the NIAR report for MTM45/6781 S2 glass [Ref. 22]. As the calibration tests with an aluminum coupon only provided a margin of error for the material’s Young’s modulus, this S2-glass/epoxy testing also provided a margin of error for the material strength as well as insight into the sensitivity to the manufacturing techniques.

Because this was not a full test to determine the mechanical properties of the S2-glass/epoxy material, only three coupons were tested to compare the properties for in-date S2-glass/epoxy. The coupons were made 12 layers thick and were 10” long and 1” wide per sizing in Reference 22. The cured ply thickness was assumed to be 0.0101” for a total laminate thickness of 0.1212”; the actual measured dimensions of the coupons were used to calculate the final material strength allowables, not the normalized dimensions.

2.1.2 Results of S2-Glass/Epoxy Testing

The average peak load for testing in-date S2-glass was 10,976 lbs., and the standard deviation is 239 lbs. Figure 2.1 shows a front view for two of the in-date S2-glass/epoxy coupons after failure.



Figure 2.2: Front View of Failure Mode for S2-glass/epoxy Coupons -2 (Top) and -3 (Bottom)

Both of these coupons failed in brittle failure laterally across the coupon as expected for composite tensile testing. The main difference between the two coupons in Figure 2.2 is the location of the failure. One coupon failed across the strain gages and the other failed near the tab. The failure location in these coupons appeared to be driven by the variable width of the coupons as the coupons in Figure 2.2 appear to have failed at the narrowest location. The variable coupon dimensions for the fiberglass and quartz coupons were a result of the coupons being manufactured by hand, and thus lacked the precision of automated manufacturing causing the variable width along the length of the coupons. Figure 2.3 shows the failure mode of the final in-date S2-glass/epoxy coupon.

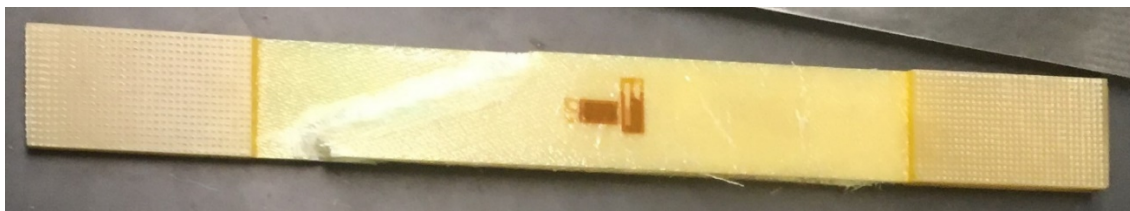


Figure 2.3: Front View of In-Date S2-glass/epoxy Coupon -1

Because the coupon in Figure 2.3 was made of 0° fibers and in-date material, the assumption was that it should fail laterally across the coupons following the failure modes shown in Figure 2.2. The failure mode shown in Figure 2.3 suggests twisting which is likely a function of the flexure in two directions found

during the aluminum calibration tests. The final results for the in-date S2-glass/epoxy tensile tests can be found in Table 2.3, along with the properties reported in Reference 20.

Table 2.3: Final Results of 0° In-Date S2-glass/epoxy Testing

	Ultimate Strength	Young's Modulus	Failure Mode*
Coupon I.D.	σ_{tu} (ksi)	E_1 (Msi)	
FGTC0-1	87.8	3.91	SGB
FGTC0-2	84.71	3.66	LGM
FGTC0-3	84.35	3.96	LGM
Average	85.62	3.84	
NIAR Values [Ref. 22]**	81.46	4.2	-

*1st characters – L represents lateral failure S means longitudinal splitting failure

*2nd characters – G means failure occurred within the coupons gage section

*3rd characters – M or B represents failure occurring near the middle, or bottom of the coupon, respectively.

**Material testing with coupons manufactured with an oven cure cycle

The results included in Table 2.3 show an average ultimate strength of 85.62 ksi, where the warp ultimate strength reported by NIAR is 81.46 ksi [Ref. 22]. This shows a 5.1% increase in the material property over the NIAR report. The NIAR report for MTM45-1 6781 S-2 glass reports a standard deviation of 2.52 ksi. This means the resulting 85.62 ksi is more than one standard deviation away from the average strength, which would indicate that the load cell on the test stand is likely over estimating the applied load.

The average Young's modulus in Table 2.3 was calculated as 3.84 Msi, where the warp Young's modulus reported by NIAR was 4.2 Msi [Ref. 22]. This corresponds to an 8.6% decrease in the Young's modulus of the material compared to the NIAR report. These results resemble the reduced Young's modulus values generated during the aluminum calibration tests which again suggests the test setup is under reporting the Young's modulus. Since the Young's modulus was under reported, no correction factors were applied to the tested quartz Young's modulus as under reporting will result in a more conservative Young's modulus.

Interestingly, these results also suggest an over predicted stress. While the over predicted stress would result in an un-conservative ultimate strength, no-correction factors will be applied to the tested quartz strength as the strength will already be significantly reduced due to the expired nature of the resin

system. In other words, the strength properties reported in the following sections are still expected to be conservative.

2.1.3 Results of 0° Quartz Tensile Testing

The following section presents the results of the 0° mechanical properties for the donated quartz material. Figure 2.4 shows the average stress – strain curve, and the stress-strain curves for each individual 0° coupon.

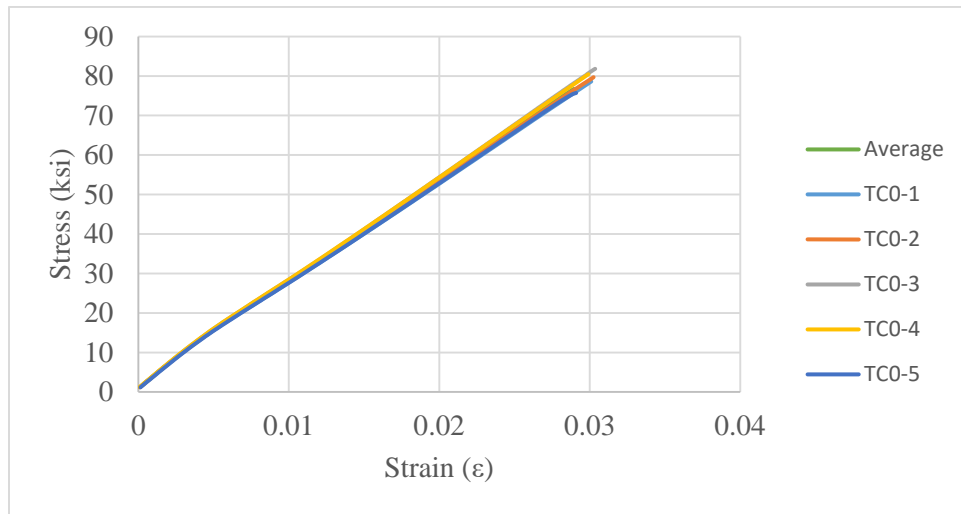


Figure 2.4: Stress – Strain Curves for 0° Coupons

Each 0° coupon was tested at a test rate of 2 mm/min as recommended in the ASTM standard [Ref. 18]. Individual test results including the peak loads, and peak elongation for each coupon are included in Appendix B. Figure 2.5 shows the side view of the failure modes for every 0° coupon. Every 0° coupon experienced two failure modes including explosive failure and delamination.



Figure 2.5: Side View of 0° Coupons (Coupons Numbered 1 – 5, Left to Right)

Both failure modes represent deviations from the expected failure mode of a 0° coupon. A 0° coupon is expected to fail through brittle failure laterally across the width of the coupon (as was shown through the S2-glass/epoxy test results). The primary failure was an explosive failure resulting in the ultimate fracture of the coupons. This failure mode showed failure near one edge of the coupons which would be indicative to the two-axis bending defined by the calibration testing (see Appendix A). The significant ply delamination is likely caused by the expired resin system. Due to expiration, the resin did not flow well resulting in very dry interfaces between the plies (confirmed by inspecting the failed coupons), which allowed for the delamination seen in Figure 2.5. The failure modes of the coupons are highlighted in Figure 2.6. Figure 2.6a and 2.6b represent failure of the surface plies and Figures 2.6c and 2.6d represent the ultimate failure of the coupon.

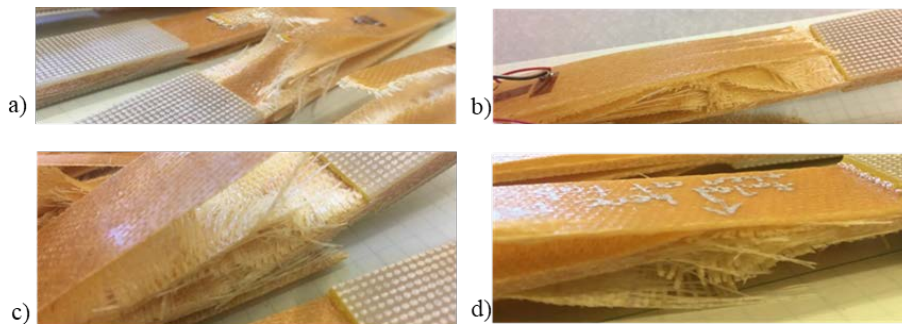


Figure 2.6: Surface Ply Failure (a, b) and Ultimate Failure (c, d) caused by Induced Bending in the Test Stand

Different modes of failure occurred for the surface plies. The surface plies shown in Figure 2.6a show ply splitting where Figure 2.6b shows the surface ply failing laterally across the coupon at the tab. While the failure of the surface plies was unique to each coupon it is important to observe these were secondary failures. The critical failure of the coupon occurred before the surface plies failed near the tabs. For the two main failure modes, the ply delamination seen in Figures 2.5 and 2.6 was assumed to be a result of the expired resin system. It is assumed that in-date material would not experience as significant of delamination because the inter-laminar bond strength of the resin would have held the plies together and the coupons would have experienced longitudinal fiber failure.

The final results for the 0° tensile testing can be found in Table 2.4. The ultimate strength, Young's Modulus, Poisson's ratio, and percent bending in the longitudinal direction were calculated following procedures outlined in ASTM D3039 – 17. As mentioned, no correction factors were applied to the mechanical testing results, as the properties found through testing were considered conservative. Plots for 0° testing can be found in Appendix B.

Table 2.4: Final Results of 0° Testing

	Ultimate Strength	Young's Modulus	Poisson's Ratio	Failure Mode*	Percent Bending
Coupon I.D.	σ_{tu} (psi)	E_1 (Msi)			%
TC0-1	81.95	3.024	0.0735	MWT (1 st) SGM (2 nd)	1.05
TC0-2	84.92	3.051	0.0730	X/MAB	N/A
TC0-3	83.65	3.145	0.0836	MWT (1 st) SAB (2 nd)	0.83
TC0-4	85.71	3.095	0.0781	MGT	0.38
TC0-5	85.13	3.055	0.0738	MGT	0.54
Average	84.27	3.074	0.0764		0.7

*1st characters – M represents multiple modes of failure and S means longitudinal splitting failure

*2nd characters – A means the coupon failed at the tab or grip, W means the coupon failed less than the width of the coupon from the tab or grip, and G means failure occurred within the coupons gage section

*3rd characters – T, M, or B in the third spot means the coupon failed near the top, middle, or bottom of the coupon, respectively.

The results of this 0° coupon testing show an average ultimate strength of 84.27 ksi, where the 0° ultimate strength reported by the material manufacturer was 121 ksi [Ref. 20], or 112 – 148 ksi [Ref. 21]. This represents a decrease of 30.33% from the reported 121 ksi. The ultimate strength of 84.27 ksi was also seen as a promising return on the ultimate strength since the storage condition of the material was unknown prior to KU AE taking possession and the material was already expired by two years. Following these material assumptions the ultimate strength of 84.27 ksi will serve as the lower bound strength of the material.

The average Young's Modulus was calculated as 3.074 Msi, where the Young's modulus reported by the material manufacturer was 3.9 Msi [Ref. 20] or 4.0 – 4.4 Msi [Ref. 21]. This corresponds to a 21.17% decrease from the reported 3.9 Msi. As mentioned in the discussion of the strength results, the Young's modulus was expected to be lower due to the material expiration and the uncertainty of material handling prior to KU AE taking possession of the material. Given these considerations the Young's modulus of 3.074 Msi will be used as a lower bound for the quartz material.

The final value listed in the right column of Table 2.4 is the percent bending in the longitudinal direction. These values are similar to those found for the aluminum coupon as the longitudinal bending was about 0.7%; due to the strain gage installation for these test the lateral flexure could not be evaluated. The percent bending for coupon TC0-2 was not able to be calculated because one of the longitudinal strain gages failed early in the test. All of the values calculated for TC0-2 were based on the values from one longitudinal strain gage instead of averaging two strain gages.

2.1.4 Results of 45° Tensile Testing

The following section presents the results for the shear properties found through testing the 45° coupons. As previously mentioned the shear properties are included with the tensile results because the testing was performed following the same procedure used for testing of the 0° coupons. Figure 2.7 shows the average shear stress – strain curve and the shear stress – strain curves for each individual test coupon.

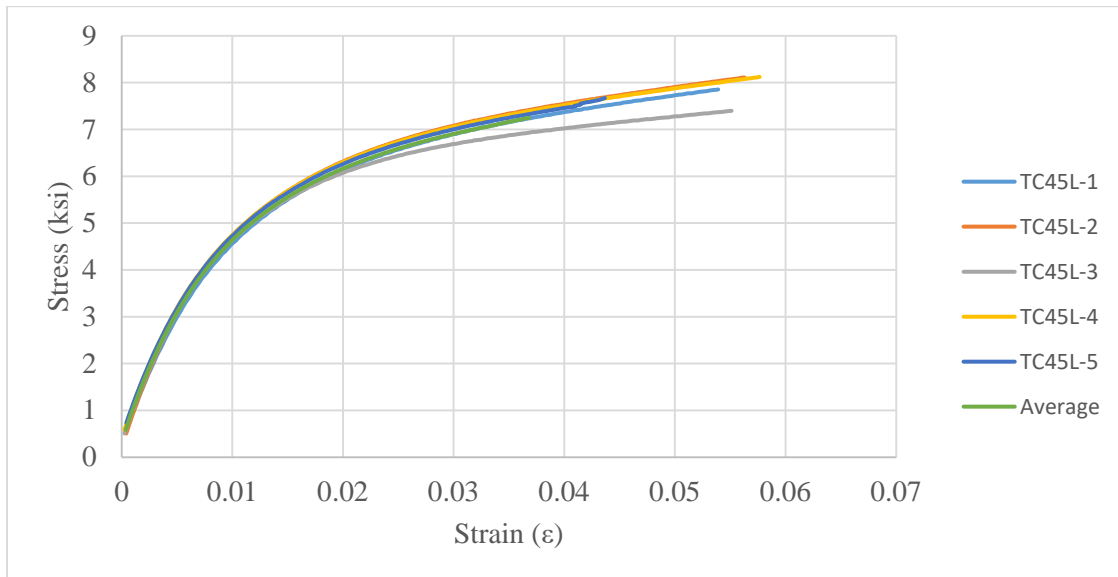


Figure 2.7: Shear Stress – Strain Curves for 45° coupons

The 45° coupons were tested at three different test rates. Coupons -1 and -2 were tested at 2 mm/min as recommended in the ASTM testing standard and failed with an average test length of 12 minutes [Ref. 18]. However, the ASTM test standard also outlines the testing rate should be set to cause failure in under 10 minutes. For coupon -3 the test rate was increase to 2.5 mm/min to cause failure in under 10 minutes, and coupons -4 and -5 were tested at 3 mm/min to determine if an increased testing rate modified the failure

modes or reduced the amount of necking. Using different test rates was considered acceptable because it did not have a significant effect on the final critical load or total crosshead displacement. Individual test results including the peak loads and peak elongation for each coupon are included in Appendix C. Figure 2.8 shows the front view of the failure modes for every 45° coupon.



Figure 2.8: Final Failure of 45° Coupons (Coupons Number 1 – 5, Left to Right)

For these tests, the main failure in coupons -1 and -2 was lateral failure across the width of the coupons while the surface plies failed at a 45° angle. Coupons -3, -4, and -5 failed at 45° angles as expected for 45° fibers. The varied failure mode between the coupons was assumed to be a function of the test rate. However, this was not the only failure which occurred. Some coupons experienced delamination near the mid-ply, as shown in Figure 2.9. These extra failure modes appeared to be created by the two-axis bending caused by the test stand coupled with the reduced performance of the expired resin system. The delamination was assumed to be caused by bending because it was more prominent near one edge of the coupon and delamination caused purely by an expired resin system would have been more uniform across the coupons, similar to the results of the 0° tensile tests.



Figure 2.9: Failure in 45° Coupons

The final results for the 45° tensile testing can be found in Table 2.5. The shear strength and shear modulus were calculated as described in Reference 19, while the percent bending was calculated as defined in Reference 18.

Table 2.5: Final Results for Shear Testing

Coupon I.D.	$F_{s0.2\%}$	$F_{s0.5\%}$	Shear Modulus (G_{12})	Failure Mode*	Percent Bending
	psi	psi	Msi		%
TC45L-1	4590	6540	0.462	X/LGT	N/A
TC45L-2	4645	6730	0.486	X/LGT	1.97
TC45L-3	4610	6410	0.464	X/AGT	1.46
TC45L-4	4800	6710	0.466	X/AGT	0.52
TC45L-5	4910	6650	0.461	X/AGT	0.91
Average	4710	6610	0.468		1.215

*1st characters – X means explosive failure occurred while L represents failure laterally across the coupon and A represents failure occurred at an angle

*2nd character – G means failure occurred within the coupons gage section

*3rd character – T in the third spot means the coupon failed near the top while in the test stand

The results of the 45° coupon testing show an average ‘ultimate’ shear strength of 6.61 ksi, where the shear strength reported by the material manufacturer was 10.6 – 11 ksi [Ref. 21]. This testing shows there is a 39.9% decrease in the shear strength of the quartz material. Similarly to the 0° results, this is reasonable considering the expiration of the material and any potential bending or twist from the test stand.

Also the average shear modulus was found to be 0.468 Msi. The material manufacturer did not report a shear modulus for comparison, so a shear modulus was predicted for the in-date quartz material.

To predict a shear modulus for in-date quartz material a scale factor was determined by comparing the 0°

test results and the 0° reported properties of the quartz material [Refs. 20 and 21]. The resulting modulus calculated from this process was 0.560 Msi. A process to determine the expected shear modulus of in-date material is further defined in Section 3.3.

The final value listed in Table 2.5 is the percent bending in the longitudinal direction. Once again, the bending values were comparable to those found during the aluminum coupon tests. The percent bending for coupon TC45L-1 was not able to be calculated because one of the longitudinal strain gages failed early in the test. All of the values calculated for TC45L-1 were based on the values from one longitudinal strain gage instead of two gages, like the rest of the coupons. The average percent bending of all the 45° coupons was 1.215%.

2.1.5 Results of family testing

The following section presents the results found through testing the 25/50/25 coupons. Figure 2.10 shows the average stress – strain curve and the stress – strain curves for each individual test coupon.

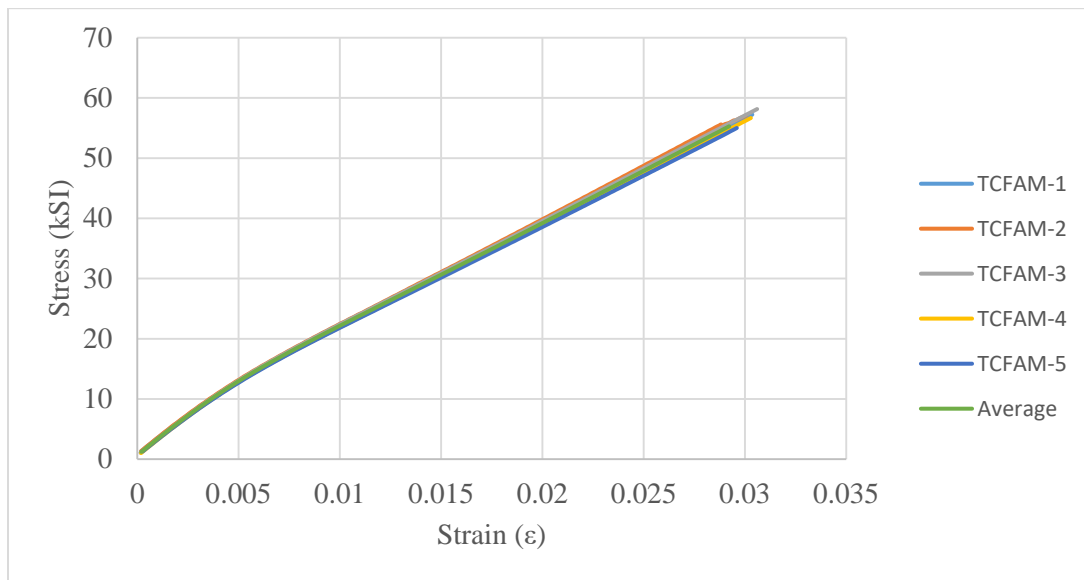


Figure 2.10: Stress - Strain Curves for the 25/50/25 Family Coupons

The 25/50/25 family coupons were tested at a test rate of 2 mm/min as recommended in the ASTM standard [Ref. 18]. Individual test results including the peak loads and peak elongation, for each coupon are included in Appendix D.

Figure 2.11 shows the front and side views of the 25/50/25 family coupons. In Figure 2.11a, the coupons are numbered 1 – 5, from left to right. All 25/50/25 family coupons experienced one failure mode. The main failure was delamination between the plies. On every coupon, delamination started at one edge of the coupon and propagated across the coupon until the plies were completely delaminated. This agreed with the expected failure mode, because the 45° plies failed in shear before the 0° plies could fail laterally.

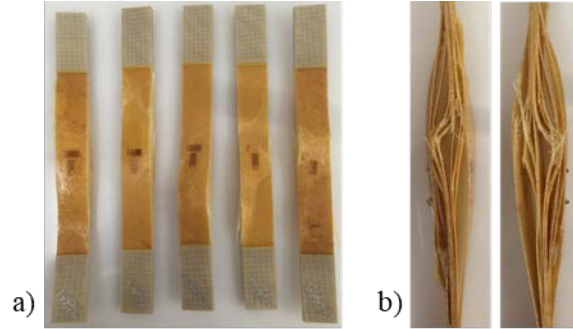


Figure 2.11: Top (a) and Side (b) Views of Failure Modes for 25/50/25 Testing

The final results for the 25/50/25 tensile testing can be found in Table 2.6. The ultimate strength, Young’s Modulus, Poisson’s ratio, and percent bending in the longitudinal direction were calculated following the equations outlined in Reference 16.

Table 2.6: Final Results of Family Testing

Coupon I.D.	Ultimate Strength	Young’s Modulus	Poisson’s ratio	Failure Modes	Percent Bending
	ksi	Msi			%
TC-FAM-1	62.90	2.543	0.2797	DGM	2.19
TC-FAM-2	61.30	2.553	0.2787	DGM	0.46
TC-FAM-3	63.71	2.574	0.2765	DGM	N/A
TC-FAM-4	62.28	2.547	0.2764	DGM	0.76
TC-FAM-5	59.68	2.507	0.2827	DGM	2.15
Average	61.97	2.545	0.2788		1.39

*1st character – D: D is representative of delamination

*2nd character – G: G means failure occurred within the coupons gage section

*3rd character – M: M is means the failure started in the middle of the coupons gage section

The results of the 25/50/25 testing include an average ultimate strength of 61.97 ksi, and an average Young’s modulus of 2.545 Msi. The material manufacturer did not report any family properties for comparison of the tested and manufacturer’s data, however it was important to perform these tests because

the family ultimate strength property is used for structural sizing and provides the lower limit for the laminate. The Young's Modulus, Poisson's ratio, and percent bending were calculated to produce a full set of results. Similar to the 0° and 45° tests, the average percent bending in each coupon was 1.39%.

2.2. Compression Testing of Quartz Material

Further testing was performed to determine the compressive mechanical properties of the quartz material. Since the MTS test stand used to perform the tensile tests is not compatible for compression testing, a new machine was used to perform compression testing. The test stand used to perform the following compression test is also a MTS hydraulic test stand and property of the KU CEAE department. The force transducer on this test stand was also expired however, due to time restrictions calibration tests were not able to be performed for this test stand.

The following sections will discuss the final results of compression testing of the quartz material. The procedure used to perform the testing is outlined in SACMA SRM 1R-94 [Ref. 23], a modified version of ASTM D695. The primary difference between the SACMA and ASTM test standards was the test fixture. The test fixture used for these tests can be seen in Figure 2.12.

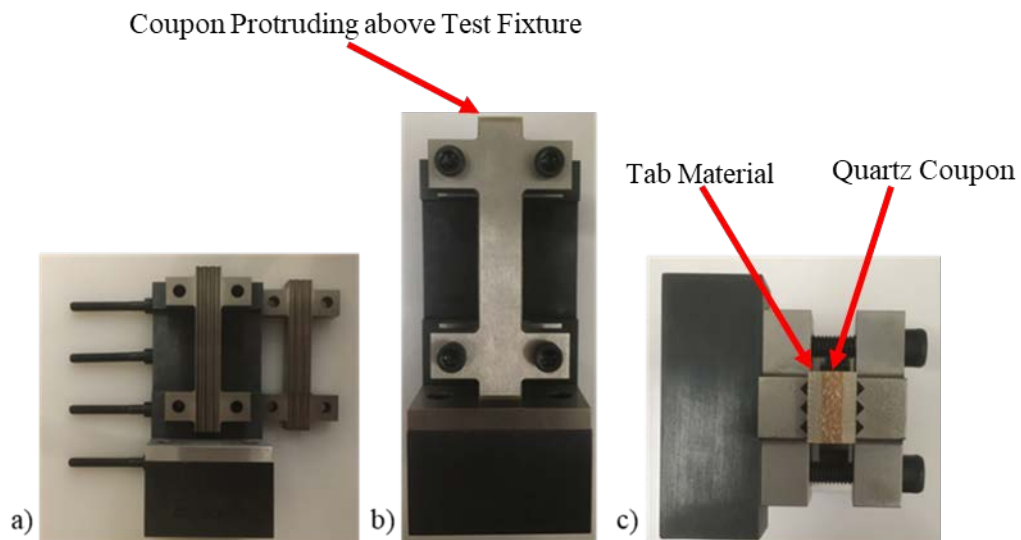


Figure 2.12: Compressive Test Fixture Components (a), Setup Front view (b) and Top View (c)

Figure 2.12a shows the components of the compressive test fixture while Figures 2.12b and 2.12c show the test fixture with a coupon set up for testing. The front view of the test fixture setup shows the

coupon extends above and below the gripping surfaces of the fixture ensuring the coupon is loaded in compression; not the fixture itself. The top view in Figure 2.12c is illustrating the use of tabbing between the gripping teeth of the fixture and the quartz material.

Compressive testing was performed to determine the following properties:

1. Ultimate Strength (0°)
2. Modulus of Elasticity (0°)
3. Poisson's Ratio (0°)
4. Family Ultimate Strength (25/50/25)
5. Family Modulus of Elasticity (25/50/25)
6. Family Poisson's Ratio (25/50/25)

Reference 23 outlines one test for finding the compressive strength of the material and one test for finding the compressive Young's modulus and Poisson's ratio. The coupons manufactured include: five – 0° coupons and five – 25/50/25 coupons for strength testing, and five more of each type of coupon for Young's modulus and Poisson's ratio testing. Separate coupons had to be manufactured depending on the property being tested because the compressive strength was tested with tabs between the test fixture grips and the material, while the Young's modulus and Poisson's ratio coupons had strain gages installed instead of the tabs.

The desired coupon dimensions for compression testing are as follows for testing of a woven cloth fabric: 3.18" long, 0.5" wide, and 0.12" thick [Ref. 23]. Assuming the material thickness was 0.0105", as reported by the material manufacturer, all compressive coupons were manufactured with 12 layers of quartz creating a final assumed cured thickness of 0.126". The ply thickness of 0.0105" did not allow for the 0.12" thickness, but using a 12 layer layup allowed for a balanced and symmetric laminate for the 25/50/25 family coupons while meeting the minimum coupon thickness. The stacking sequence for the 25/50/25 coupons was [45,0,45,0,45,0]_s.

Each coupon was thicker than the assumed 0.126" and the overall average thickness between the coupons was used to calculate a new cured ply thickness. The 0° coupons had an average laminate thickness of 0.1415" and an average cured ply thickness of 0.0118", while the 25/50/25 family coupons had an

average thickness of 0.136” for an average cured ply thickness of 0.0113”. The newly determined actual coupon dimensions were used to calculate the material properties; not the assumed dimensions.

2.2.1 Results of Compressive Strength Testing

Each coupon was tested at a test rate of 1 mm/min for compressive strength testing [Ref. 23]. The individual coupon failure loads are reported in Appendix E. The average failure load was 5,070 lbs., with a standard deviation of 111.7 lbs.

Figure 2.13 shows the side view and failure of the 0° and family coupons for the compressive strength tests. Each coupon was loaded until the first load drop on the load versus cross-head displacement plot created by the MTS computer. Coupons are labeled -1 to -5 from the top of the pictures to the bottom. Coupon CCSFam – 2 was loaded until the tabs were touching instead of stopping at the first sign of failure. The extra loading on this coupon was used to see if the first load drop represented 1st ply failure or complete failure of the coupon. Results found from complete testing of this coupon did not produce any significant results beyond the initial failure. Any failure after the initial failure occurred beyond the test section of the coupon meaning the results were affected by failure of the bond line between the material and the tabs.

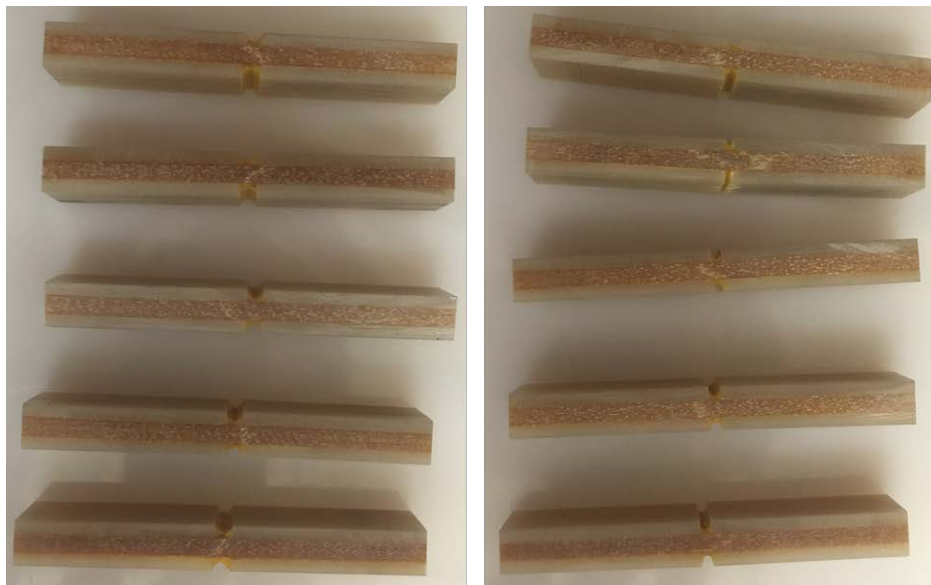


Figure 2.13: Side View of Compressive Strength Coupons (0° - left, 25/50/50 – right)

The final results for the compressive strength testing can be found in Table 2.7. The results of the 0° compressive strength tests show an average ultimate compressive strength of 71.01 ksi, where the 0°

compressive strength reported by the material manufacturer was 81 ksi [Ref. 20], or 86 - 110 ksi [Ref. 21]. This represents a 12.33% decrease in the ultimate compressive strength of the quartz material from the reported 81 ksi. This shows there was greater retention of the compressive properties than the tensile properties but this was expected given that the material is bearing against itself when in compression. A 12.33% decrease of the ultimate compressive strength was considered reasonable since the material was expired by two years and it followed the same trend as the tensile testing results.

Table 2.7: Final Results for Compressive Strength Testing

	0° Coupon Results		25/50/25 Family Coupon Results
Coupon I.D.	σ_{cu} (ksi)	Coupon I.D.	σ_{cu} (ksi)
CCS00-1	70.15	CCSFam-1	61.84
CCS00-2	68.33	CCSFam-2	59.84
CCS00-3	72.90	CCSFam-3	62.75
CCS00-4	72.10	CCSFam-4	63.64
CCS00-5	71.56	CCSFam-5	61.29
Average for 0° Coupons	71.01	Average for Family Coupons	61.87

The results of the 25/50/25 family compressive strength tests show an average ultimate strength of 61.87 ksi. The family compressive strength was not reported by the material manufacturer, however similar to the tensile test it was important to perform tests for the family properties because the family strength will be used for structural sizing for any application of this material. Also the compressive testing showed 15.7% change between the tensile and compressive 0° strength and the 25/50/25 family testing showed almost identical results between the tensile and compressive tests. This was expected because a 25/50/25 family has been seen to produce similar responses and failure modes under tensile and compressive loading as can be seen from the properties of MTM45-1/6781 S2 glass from Reference 22.

2.2.2 Results of Compressive Modulus Testing

Each compressive modulus coupon was loaded at a rate of 1 mm/min until the output from the longitudinal strain gage was 5000 micro - strain. This was required by SACMA SRM 1R-74 to allow for

calculating the modulus values from the stress –strain relationship recorded at 1000 and 3000 micro-strain [Ref. 23]. The test level data can be found in Appendix E.

Figure 2.14 shows the strain gage setup used on the coupons tested to determine the compressive Young’s modulus and Poisson’s ratio. The compression coupons were made so small that unlike with the tensile testing coupons, it would not have been possible to install two linear strain gages. To ensure both a longitudinal and lateral strain gage were installed, rosette strain gages were used for compression testing



Figure 2.14: Strain Gage Setup for Compressive Young’s Modulus Testing

The final results for the compressive Young’s modulus testing can be found in Table 2.8. Two averages are presented for the 0° coupon tests. Coupon CCE00-2 produced relatively low values for the compressive Young’s modulus and Poisson’s ratio compared to the other four coupons tested. The error in testing coupon CCE00-2 was assumed to be due to strain gage calibration error at the start of the test. The results for this test were removed from the average calculations to find the average values with and without the outlier data. The values in Table 2.8 which read ‘N/A’ were unable to be calculated because the strain gages either failed or the bonding adhesive failed and the strain gage came off the coupon.

Table 2.8: Final Results for Compressive Modulus and Poisson’s Ratio Testing

0° Testing	Compressive Young’s Modulus	Poisson’s Ratio	25/50/25 Family Testing	Compressive Young’s Modulus	Poisson’s Ratio
Coupon I.D.	σ_{cu} (ksi)		Coupon I.D.	σ_{cu} (ksi)	
CCE00-1	3.44	0.12	CCEFam-1	N/A	N/A
CCE00-2	2.31	0.08	CCEFam-2	2.87	0.28
CCE00-3	3.28	N/A	CCEFam-3	2.76	0.25
CCE00-4	3.53	0.16	CCEFam-4	2.81	0.27
CCE00-5	3.80	0.15	CCEFam-5	3.05	0.28
Average for 0° Coupons	3.27	0.13	Average for Family	2.87	0.27
Average without -2	3.51	0.14			

The results of the testing shows an average Young’s modulus for the 0° testing of 3.51 Msi, where the material manufacturer reported 4.2 Msi [Ref. 20] or 4.4 – 4.9 Msi [Ref. 21]. This testing shows there is a 16.4% decrease in the compressive Young’s modulus of the quartz material. The Poisson’s ratio was not reported by the manufacturer, but it was considered reasonable base on the results for the Young’s modulus. Both the compressive modulus and Poisson’s ratio followed the same trend as the tensile testing results. The Poisson’s ratio was almost identical to what was calculated through 0° and family tensile testing, while the compressive Young’s modulus was retained more than the tensile Young’s modulus which was similar to the results of the compressive strength tests.

2.3. Summary of Mechanical Testing

As mentioned the mechanical testing discussed in the previous sections produced possible a lower bound for the material allowables which was expected due to the testing of an expired material. However, the failure modes seen in the tensile testing were unexpected. The S2-glass coupons showed that the expected failure mode for tensile testing of a composite material with an epoxy resin system was lateral failure across the coupon; however, the quartz coupons also experienced significant delamination. Due to expiration it was assumed the resin did not flow properly and dry fibers were still present in the tested quartz coupons. The final results for the 0°, 25/50/25 family, and shear properties are summarized in Tables 2.9, 2.10, and 2.11, respectively.

Table 2.9: Final 0° Results

Properties	Results
E_1 (Msi)	3.07
E_{1c} (Msi)	3.51
ν_{12} (tensile)	0.0764
ν_{12} (compressive)	0.14
F_{tu} (ksi)	84.3
F_{cu} (ksi)	71.01

Table 2.10: Final 25/50/25 Family Results

Properties	Results
E_1 (Msi)	2.55
E_{1c} (Msi)	2.87
ν_{12} (tensile)	0.2788
ν_{12} (compressive)	0.27
F_{tu} (ksi)	61.97
F_{cu} (ksi)	61.87

Table 2.11: Final Shear Results

Shear Properties	
Properties	Results
G_{12} (Msi)	0.468
F_{sy} (ksi)	4.71
F_{su} (ksi)	6.61

Throughout tensile testing multiple sources of error were identified including two axis flexure, an over prediction of the strength and an under prediction of the stiffness. The errors were assumed to be caused, in part, by a combination of the expired calibration of the test stand as well as the mis-alignment of the cross-head. While the expired calibration of the test stand used for tensile testing showed an over prediction of the material strength and an under prediction of the stiffness, no correction factors were added to the mechanical test results of the expired quartz material. Even with the over prediction of the strength, no correction factors were applied because the strength properties were still considered to be conservative due to the expired nature of the material; while the Young's Modulus did not have a correction factor added because it was under predicted and therefore was considered more conservative. Given the significant reduction in the quartz properties as compared to the manufacturer's data, the tested values served as an adequate lower bound for the subsequent structural sizing presented in the following chapter.

Also, it is understood that the mechanical properties defined by this material testing should not be used as a basis for design and analysis of future flight-worthy hardware, and it is possible that claims of conservatism of mechanical design properties will not be supported with future statistically valid testing of

in-date materials. However, recall that the primary focus of this thesis is not mechanical characterization of the quartz/epoxy material, but rather a reasonable first approximation for whether the improved electrical performance could ever justify the increased cost of quartz.

3. Structural Application for Quartz Material

The structural analysis in this chapter provides sizing requirements for radomes constructed of both S2-glass and quartz. By first sizing each type of radome to a set of real loads, the electrical comparison is more realistic since families and thicknesses will be defined. The analysis presented in this chapter is based on the dielectric ventilation panel and antenna mounting bracket designed for integrating two 2 – 18 GHz horn antennas into NASA's Gulfstream V (GV) aircraft [Ref. 24]. Analysis is also presented for a modified GV outer moldline radome that accommodates four MCoRDS antennas [Ref. 25]. While the 2 – 18 GHz horn antennas were only installed over the smaller replacement ventilation panels, the larger MCoRDS radome panels were also assessed structurally to expand the electrical analysis to include significantly thicker laminates. Because the Original Equipment Manufacturer (OEM) loads and stresses were not made available, both of these designs were sized using a comparative analysis approach similar to the analysis in References 24 and 25.

In this chapter, Section 3.1 provides an overview for the design for the existing dielectric ventilation panel, horn antenna bracket, and MCoRDS radome. Section 3.2 discusses the loading conditions used for sizing the structures, while Section 3.3 discusses the material properties used for sizing the structures. Sections 3.4 and 3.5 provide discussion over the results of the analysis for the dielectric ventilation panel and the MCoRDS antenna radome, respectively.

3.1 Overview of the Current GV Designs

This section is a review of the current GV aircraft panels designed to accommodate the 2 – 18 GHz horn and MCoRDS antennas. For the 2 – 18 GHz horn antennas, the full design includes installing one antenna in each fuselage cavity (port and starboard), creating a two-element system [Ref. 24]. The original design for the fuselage panel of the GV aircraft was a carbon fiber panel with a metallic vent for pressure equalization. For installation of the 2 – 18 GHz horn antennas each metallic vent was replaced with an RF transparent S2-glass/epoxy ventilation panel. Figure 3.1 shows the approximate location of the fuselage

cavities behind the landing gear. Figure 3.2 is an isometric view of the final design of the 2 – 18 GHz horn antenna assembly on the Outer Moldline (OML) carbon fiber GV fuselage panel [Ref. 24].

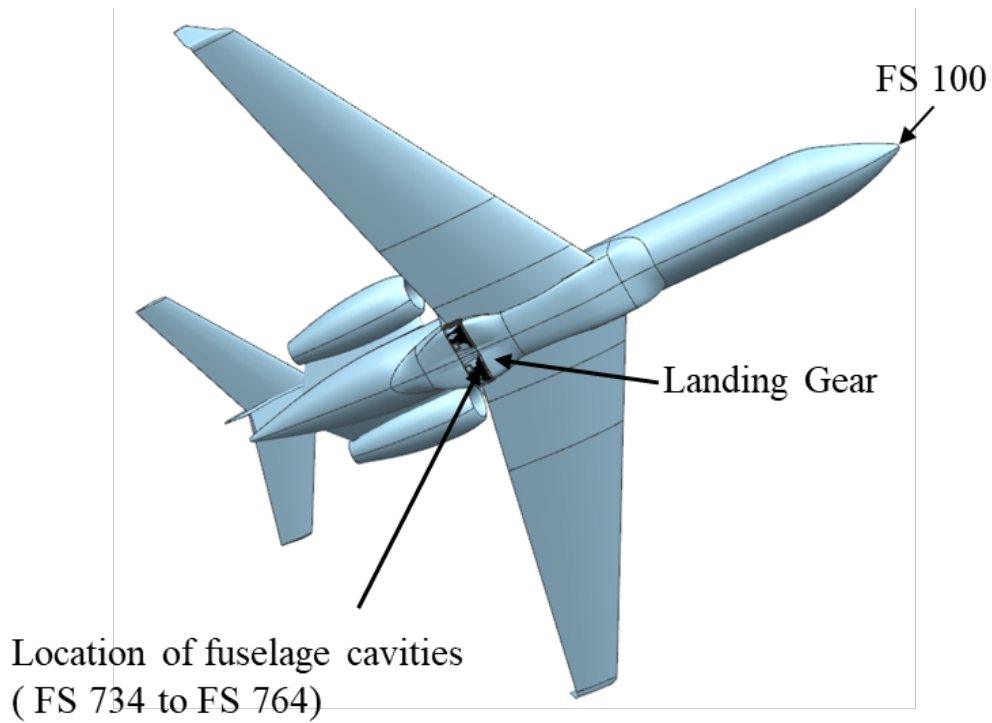


Figure 3.1: Location of Fuselage Panels on NASA GV Aircraft (not to scale) [Ref. 24]

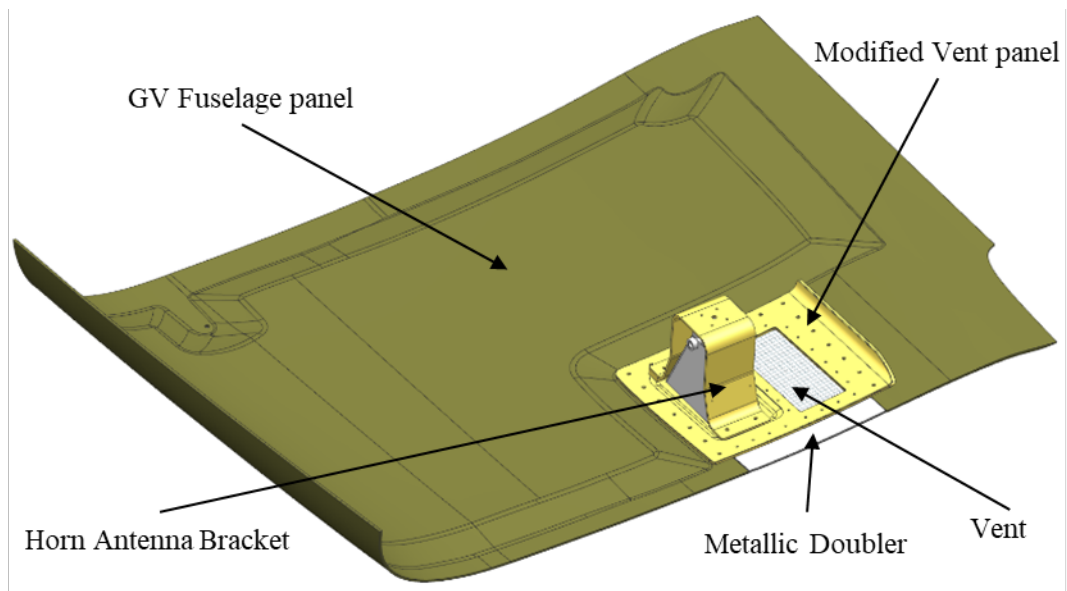


Figure 3.2: Isometric View of Antenna Assembly on GV Fuselage Panel [Ref. 24]

The final design for the dielectric ventilation panel was primarily made of ACG S2-glass 6781/DPL 862 epoxy cloth; a wet layup composite material. The dielectric ventilation panel was made with 18 layers of S2-glass/epoxy everywhere except in the recessed region [Ref. 24]. The recessed region of the panel is the region directly underneath the 2 – 18 GHz horn antenna and was designed with 12 layers of glass. The 18 and 12 layer sections had the following stacking sequences [Ref. 24]:

18 layers: $[0,45,0,45,0,45,0,45,0]_s$

12 layers: $[0,45,0,45,0,45]_s$

A metal mesh was used for the vent. The metal mesh was secured in place by sandwiching it between the glass panel and metallic doublers. A 0.040" thick aluminum doubler was used to hold the metallic mesh in place and an additional 0.063" doubler was added on the outer edge of the 0.040" doubler to meet the existing inner moldline of the panel. Reference 24 includes the analysis for this design. The full dielectric ventilation panel can be seen in Figure 3.3.

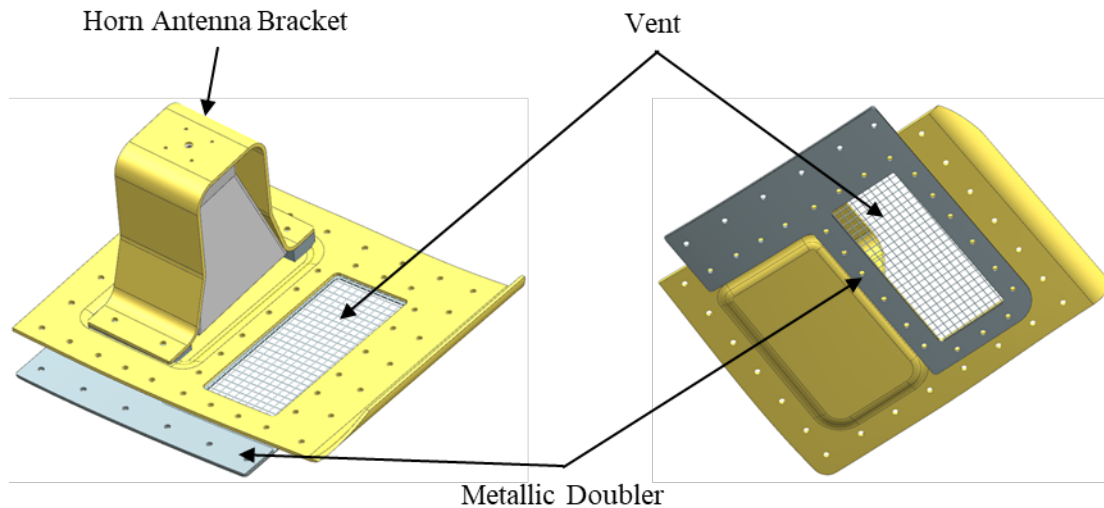


Figure 3.3: Full RF Transparent Vent Panel and Horn Antenna Bracket [Ref. 24]

In addition to the design for the dielectric ventilation panel a bracket was manufactured for mounting the horn antenna as seen in Figure 3.3. The horn antenna for this design was an A-info horn antenna [Ref. 24]. The final design for the bracket is made of 12 layers of S2 glass/epoxy with a

[0,45,0,45,0,45], stacking sequence. Also included in the assembly are shims between the mounting bracket and the recessed portion of the dielectric ventilation panel to maintain the antenna nadir [Ref. 24].

As mentioned above, the MCoRDS antennas were integrated on the aircraft via a new OML radome panel [Ref. 25]. For the MCoRDS radome, the full design includes installing two MCoRDS antennas in each fuselage cavity (port and starboard), creating a four element system [Ref. 25]. The MCoRDS radome was also designed to accommodate the dielectric vent panel meaning the outer moldline of the GV was modified to incorporate both systems [Ref. 25]. The MCoRDS radome is seated directly against the original OML carbon fuselage panel and uses the same fastener locations to attach to the aircraft. The MCoRDS radome was designed with S2-glass/epoxy. Figure 3.4 shows an exploded view of the full assembly including the dielectric vent panel and the MCoRDS radome.

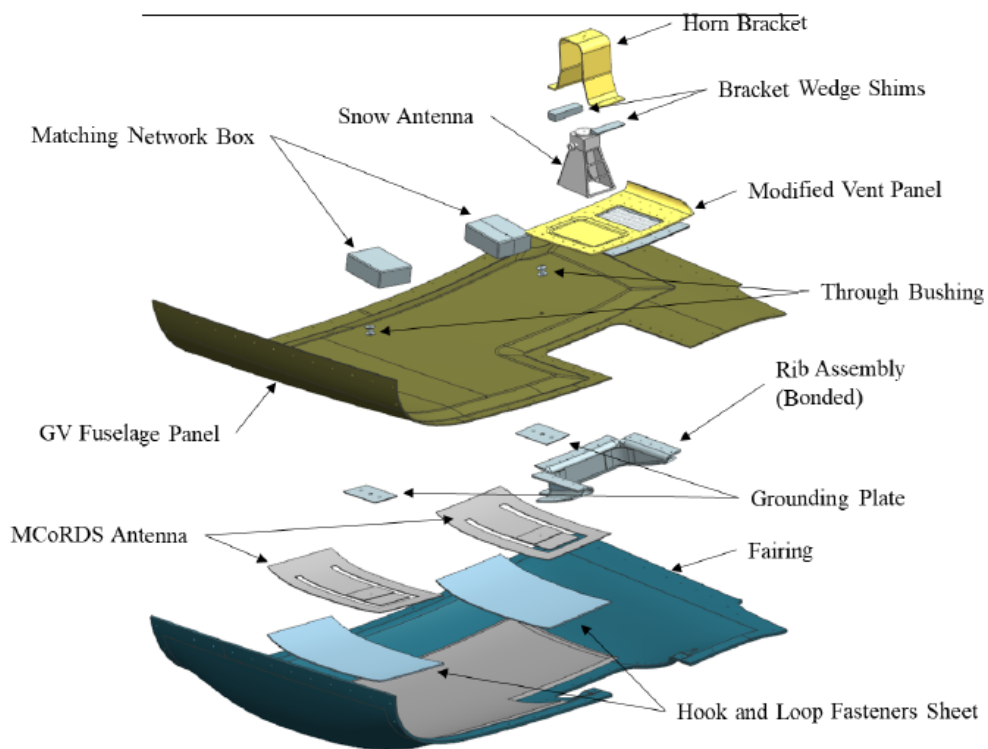


Figure 3.4: Exploded View of the GV Fuselage Fairing Assembly [Ref. 25]

The final design for the MCoRDS radome is made of MTM45-1-35%-S2SC75-8H-305-1270 pre impregnated (pre-preg) S2-glass/epoxy composite. The radome panel is made with 24 layers of glass including a region with 0.256" thick Rohacell 71-WF core. [Ref. 25]. The panel tapers down from the

sandwich design to a monolithic laminate in regions where fasteners are located. The following are the regional stacking sequences for the radome [Ref. 25]:

Monolithic: [0,45,0,45,0,45,45,0,45,0,45,0]_s

Sandwich: [0,45,0,45,0,45,45,0,45,0,45,0,Rohacell 71-WF]_{os}

In addition to the design for the radome, a rib structure was manufactured for support between the dielectric ventilation panel and the new OML radome structure. The rib structure was designed as a structural attachment point between the carbon panel and the new radome [Ref. 25]. The final design for the bracket is made of 14 layers of pre-preg S2-glass/epoxy composite [Ref. 25].

3.2 Loading Conditions for Structural Sizing

During the design of the dielectric ventilation panel and the MCoRDS radome five aerodynamic loads and three inertial loads were considered [Ref. 24 and 25]. The load cases considered for each analysis are presented in References 24 and 25 [Ref. 22 – 26]. CFD analysis was used to determine the most critical aerodynamic load cases. Each of the aerodynamic load cases resulted in compressive internal forces and the aerodynamic load cases which created the highest internal compressive forces were then coupled with each inertial load to determine the final structural load cases. From References 24 and 25 only one load case was determined to be critical (i.e. one load case resulted in the lowest Margin of Safety (MS)) for all failure conditions) for the dielectric ventilation panel, while two load cases were determined to be critical for the MCoRDS radome. Table 3.1 shows the inertial load factor which is coupled with the aerodynamic loads shown in Table 3.2 to size the dielectric ventilation panel and MCoRDS radome.

Table 3.1: Inertial Load Factor

Direction	Inertial Load Factor (Ultimate)
Downwards	9g

Table 3.2: Aerodynamic Load Cases

Aerodynamic load					
Load Cases	Mach	Altitude (kft)	q (psf)	Alpha (°)	Beta (°)
1	0.97	34	344	2	5
2	0.61	0	552	2	5
3	0.883	35	344	2	5

The 9g downward load case in Table 3.1 was selected because it caused the highest compressive stresses in the panels sized in References 24 and 25. Load Case 1 is the critical load case for the dielectric ventilation panel, while Load Cases 2 and 3 were critical for the MCoRDS radome. The new designs discussed in this document also maintained the load and safety factors used in the glass panel design. These factors are discussed in detail in References 24 and 25, and are provided by Reference 26:

3.3 Material Properties

As mentioned previously, the quartz material properties provided by the manufacturer are typically the ideal material properties, while the tested properties of the expired material are likely lower than the in-date material properties; however, these two sets of properties provided an upper and lower bound for the mechanical properties. Quartz replacement panels were sized using both sets of properties to examine the possible range of mechanical designs and corresponding electrical performance.

The following tables include the material properties used in this analysis. S2-glass properties used for sizing the original dielectric ventilation panel and MCoRDS radome panel were taken from References 24 and 25 and are summarized in Tables 3.3 and 3.4, respectively.

Table 3.3: 6781 S-2 Glass/DPL 862 Resin Properties for Wet Layup [Ref. 24, 27]

	RTD	180F wet	
E_1^T	3,900	3,500	ksi
E_1^C	4,000	3,800	ksi
E_2^T	3,800	3,400	ksi
E_2^C	4,000	3,800	ksi
G_{12}	600	400	ksi
ν_{12}	0.130	0.130	
t_{nom}	0.009	0.009	in
ρ	0.065	0.065	lb/in ³
F_1^T	23.5	18.5	ksi
F_1^C	25.0	17.0	ksi
F_2^T	21.5	19.0	ksi
F_2^C	25.0	17.0	ksi
F_{12}	13.5	9.5	ksi

The Room Temperature Dry (RTD) properties from Table 3.3 were used in the sizing of the original glass vent panel, while the RTD and Elevated Temperature Wet (ETW) properties from Table 3.4 were used in sizing the original MCoRDS radome.

Table 3.4: ACG S2-Glass 6781/MTM45-1 Epoxy Pre-Preg Properties [Ref. 22]

	-65, Dry	RTD	180F wet	
E_1^T	4,300	4,200	3,900	ksi
E_1^C	4,400	4,200	4,100	ksi
E_2^T	4,100	4,100	3,800	ksi
E_2^C	4,200	4,000	3,900	ksi
G_{12}	700	600	300	ksi
ν_{12}	0.140	0.140	0.120	-
t_{nom}	0.010	0.010	0.010	in
α_1	6.5×10^{-6}	6.5×10^{-6}	6.5×10^{-6}	in/in/°F
α_2	6.5×10^{-6}	6.5×10^{-6}	6.5×10^{-6}	in/in/°F
ρ	0.065	0.065	0.065	lb/in ³
ϵ_{11}^T	5.2×10^{-3}	5.2×10^{-3}	5.0×10^{-3}	-
ϵ_{12}^C (near hole)	-3.5×10^{-3}	-3.5×10^{-3}	-3.5×10^{-3}	-
ϵ_{22}^T	6.0×10^{-3}	6.0×10^{-3}	5.5×10^{-3}	-
ϵ_{12}^C (away fr. hole)	-1.6×10^{-2}	-1.6×10^{-2}	-1.6×10^{-2}	-
γ_{12}	1.7×10^{-2}	1.7×10^{-2}	1.6×10^{-2}	-
F_1^T	38.9	32.1	24.4	ksi
F_1^C	37.0	37.0	26.3	ksi
F_2^T	38.0	30.8	20.1	ksi
F_2^C	31.6	31.6	20.1	ksi
F_{12}	12.3	9.2	5.6	ksi

Data in Tables 3.3 and 3.4 above has been arbitrarily thresholded to more reasonable strain limits in the vicinity of fasteners holes (laboratory data shows ultimate undamaged coupon strain allowables of 24000-26000 microstrain in tension and 16000 microstrain in compression), particularly for the compression strain cutoff listed. Laminated plate stress allowables are more commonly used, with assumptions for family-based bearing-bypass allowables. Ultimate tensile strength of S2-glass/epoxy cloth can be expected to be 70-85 ksi on and off-axis, depending on the bias of the weave. Ultimate compressive strength of S2-glass/epoxy cloth can be expected to be ~60 ksi. For analyses herein, we have limited the former to 24.4 ksi on-axis and 20.1 ksi off-axis, and the latter to 20.1ksi. This will readily allow for open-hole tension compression allowables to account for such factors as countersinks (*0.75 reduction from nominal), fastener size (*0.9), finite widths (*0.95), edge distances (*0.85), fastener spacing (*0.9) and gaps (*0.9). S2-glass/epoxy material allowables are believed to be

conservative for even conventional safety factors, and are well below even E-glass cloth properties available in MIL-HDK-17.

Also the material properties for the metallic doublers and shims were taken from References 24 and 25 and are included in Tables 3.5 and 3.6. The 2024-T3 aluminum was used to size the metallic doublers, while the 6061-T6 aluminum was used to size the shims.

Table 3.5: 2024-T3 Aluminum Sheet Properties, RT, QQ-A-250/5 [Ref. 28]

	RTD	
E	15,220	psi
G	6,090	psi
ρ	0.0027	lb/in ³
ν	0.25	
F _{tu}	319	psi
F _{cu}	246	psi
F _{su}	188	psi

Table 3.6: 6061-T6 Aluminum Sheet Properties, RT, QQ-A-200/8 [Ref. 28]

	RTD	
E	15,220	psi
G	6,090	psi
ρ	0.0027	lb/in ³
ν	0.25	
F _{tu}	319	psi
F _{cu}	246	psi
F _{su}	188	psi

Since the material testing presented in Chapter 2 only included un-notched coupons, quartz open-hole allowables were estimated by multiplying the tested strength of the 25/50/25 family coupons by the ratio of the S2-glass/epoxy open-hole allowable to the un-notched allowable. This ratio was performed using family open-hole data for the S2-glass/epoxy material available from NIAR and presented in Table 3.7 [Ref. 22].

Table 3.7: MTM45-1/ 6781 S-2 Glass Properties [Ref. 22]

	RTD (0°) Un-notched	RTD (25/50/25) Un-notched	RTD (25/50/25) Open-Hole	180F wet	
E ₁ ^T			4,200	3,900	ksi
E ₁ ^C			4,200	4,100	ksi
E ₂ ^T			4,100	3,800	ksi
E ₂ ^C			4,000	3,900	ksi
G ₁₂			600	300	ksi
ν ₁₂			0.140	0.120	
t _{nom}			0.010	0.010	in
ρ			0.065	0.065	lb/in ³
F ₁ ^T	81.46	63.7	32.1	24.4	ksi
F ₁ ^C	83.43	70.76	37.0	26.3	ksi
F ₂ ^T	80.5		30.8	20.1	ksi
F ₂ ^C	69.07		31.6	20.1	ksi
F ₁₂			9.2	5.6	ksi

The resulting material allowables are highlighted in yellow in Table 3.8. A scale factor was found for each property individually based on the relationship between the 25/50/25 un-notched and open-hole properties for S2-glass/epoxy, highlighted in red in Table 3.7 [Ref. 22]. Equation (3-1) shows an example calculation for the longitudinal tensile strength. The fiberglass properties were used for the scale factors due to the similarities between the glass/epoxy and quartz/epoxy composite materials.

$$F_1^T = 61.973 \text{ ksi} * \frac{32.06 \text{ ksi}}{63.7 \text{ ksi}} = 31.2 \text{ ksi} \quad (3-1)$$

Furthermore, Elevated Temperature Wet (ETW) quartz properties were estimated using a second scale factor based on the ratio of the RTD and ETW properties of S2-glass/epoxy included in Table 3.7 [Ref.22]. The final scale factors to convert from RTD to ETW properties are: 0.924*E₁^T, 0.969* E₁^C, 0.926*E₂^T, 0.980* E₂^C, 0.618*G₁₂, 0.841* ν₁₂, 0.760*F₁^T, 0.711*F₁^C, 0.653*F₂^T, 0.636*F₂^C, and 0.609*F₁₂.

Table 3.8 summarizes the conservative quartz properties, defined in Chapter 2, used for the sizing of the dielectric ventilation panel and MCoRDS radome panel. The values highlighted in yellow correspond to the open-hole material allowables calculated using the previously discussed procedure.

Table 3.8: Quartz Material Properties from Material Testing

	RTD (Tested)	RTD (Scaled)	ETW (Scaled)	
E_1^T	3,074	3,074	2,841	ksi
E_1^C	3,513	3,513	3,405	ksi
E_2^T	-	3,074	2,847	ksi
E_2^C	-	3,513	3,443	ksi
G_{12}	468	468	289	ksi
ν_{12}	0.143	0.143	0.120	
t_{nom}	0.0114	0.0114	0.0114	in
ρ	0.0416	0.0416	0.0416	lb/in ³
F_1^T	61.97	31.2	23.7	ksi
F_1^C	61.87	32.4	23.0	ksi
F_2^T	-	30.0	19.6	ksi
F_2^C	-	27.6	16.8	ksi
F_{12}	6.7	6.7	4.1	ksi

Table 3.9 summarizes the quartz material properties derived using the manufacturer's data. Similar to the tested properties, the quartz manufacturer only provided un-notched coupon strengths, so the properties were again scaled. As shown by Equation (3-2), this time the properties were scaled using the ratio of the un-notched Warp (0°) and open-hole 25/50/25 properties of S2-glass [Ref. 22]. The values highlighted in red in Table 3.9 correspond to the open-hole material allowables calculated using this approach, while the ETW properties were scaled by the previously discussed scale factors.

$$F_1^T = 121 \text{ ksi} * \frac{32.06 \text{ ksi}}{81.46 \text{ ksi}} = 47.6 \text{ ksi} \quad (3-2)$$

Finally, the shear modulus (G_{12}) and Poisson's ratio were not reported by the quartz manufacturer so the properties were estimated based on the material testing results. The shear modulus was found by calculating a ratio between E_1^T of the tested and reported properties to use as a scale factor. The Poisson's ratio was directly carried over from the material testing.

Table 3.9: Quartz Material Properties as Reported [Refs. 20 and 21]

	RTD (reported)	RTD (Scaled)	ETW (Scaled)	
E_1^T	3,900	3,900	3,604	ksi
E_1^C	4,200	4,200	4,071	ksi
E_2^T	-	3,900	3,613	ksi
E_2^C	-	4,200	4,116	ksi
G_{12}^*	-	560	346	ksi
ν_{12}^*	-	0.143	0.120	
t_{nom}	0.0105	0.0105	0.0105	in
ρ	0.0416	0.0416	0.0416	lb/in ³
F_1^T	121	47.6	36.2	ksi
F_1^C	81	35.9	25.5	ksi
F_2^T	-	46.4	30.3	ksi
F_2^C	-	37.0	23.5	ksi
F_{12}	9.9	9.9	6.0	ksi

Analysis in the following sections includes sandwich designs sized with Rohacell 71-WF core material. Table 3.9 summarizes the material properties of the core material.

Table 3.10: Rohacell 71 WF Properties [Ref. 29]

	RTD	
E	15,220	psi
G	6,090	psi
ρ	0.0027	lb/in ³
ν	0.25	
F_{tu}	319	psi
F_{cu}	246	psi
F_{su}	188	psi

3.4 Analysis for the RF Transparent Vent Panel

Since OEM loads and stresses were not available the original GV OML carbon fuselage panel was first assessed for baseline stress and displacement in Reference 24. Changes in vents and radomes were then compared with this baseline to ensure similar stresses, displacements and fastener loads, such that a comparative analysis basis of safety is established via minimal influence of original design and load paths. A similar approach is used in the assessment of the alternate designs. A maximum stress condition was used to size the modified vent panel while creating comparable stresses and a comparable maximum displacement.

For this analysis four different panels were sized for comparison to the dielectric ventilation panel from Reference 24. These panels included: a pre-preg S2-glass/epoxy panel, two quartz panels (one sized using the ideal properties and the other was sized using the conservative tested properties), and one S2-glass/epoxy sandwich panel made with 0.25” thick Rohacell 71-WF core. For the design including core, the core was only included in the recessed region of the panel to prevent having a design which requires a fastener to be driven through the core material.

A design was resized with pre-preg glass (ACG MTM45-1 6781 S2-glass [Ref. 22]), to provide a more direct comparison for pre-preg quartz. A 12 layer layup was achieved for the pre-preg glass design with a $[0,45,0,45,0,45]_s$ stacking sequence and a cured ply thickness of 0.0101”, as opposed to the 0.009” cured ply thickness for the wet layup design [Ref.24]. Another analysis substituted the S2-glass/epoxy properties for the conservative quartz RTD properties in Table 3.7 and maintained the same 12 ply layup with a cured ply thickness of 0.0114”. Analysis was also performed using the quartz properties reported by the manufacturer, as summarized in Table 3.8. The dielectric ventilation panel designed with the reported quartz properties was made with 12 layers everywhere except in the recessed region where there were only eight layers with a $[0,45,0,45]_s$ stacking sequence. The cured ply thickness used with the reported quartz properties was 0.0105” as defined by the material manufacturer [Refs. 20, 21]. Analyzing designs based on each set of quartz properties provides boundary conditions for future structural analysis. The tested properties provide a lower bound for material performance, and the reported properties provide an upper bound.

MSC.Patran/NASTRAN 2018 software was used to create the finite element models for the structural analysis. Only the most critical components of the design will be discussed in the following subsections. A summary of the stresses and margins of safety for the full design are included in Appendix F – I. The following results include reviews of the OML carbon fuselage panel stresses, stress distribution, maximum deflection (specifically the OML carbon fuselage panel), and critical loads. Critical elements found during the analysis and any changes in overall response are presented in the following subsections.

3.4.1 Overview of Comparison between Glass and Quartz models

This section provides a review of the changes in maximum deflection between the different dielectric ventilation panel designs, as well as the maximum and minimum principal stresses in the OML carbon fuselage panel. The latter is provided to assess changes in the stress distribution of the various designs. Each design discussed in the following section was designed based on maintaining the stress distribution of the OML carbon fuselage panel and sized using Load Case 1.

Figure 3.5 shows the maximum displacement of the original GV metal vent design [Ref. 24] and the design utilizing the tested quartz properties from Table 3.8. This figure illustrates the similar displacement distributions and that the maximum deflection occurred in the same location.

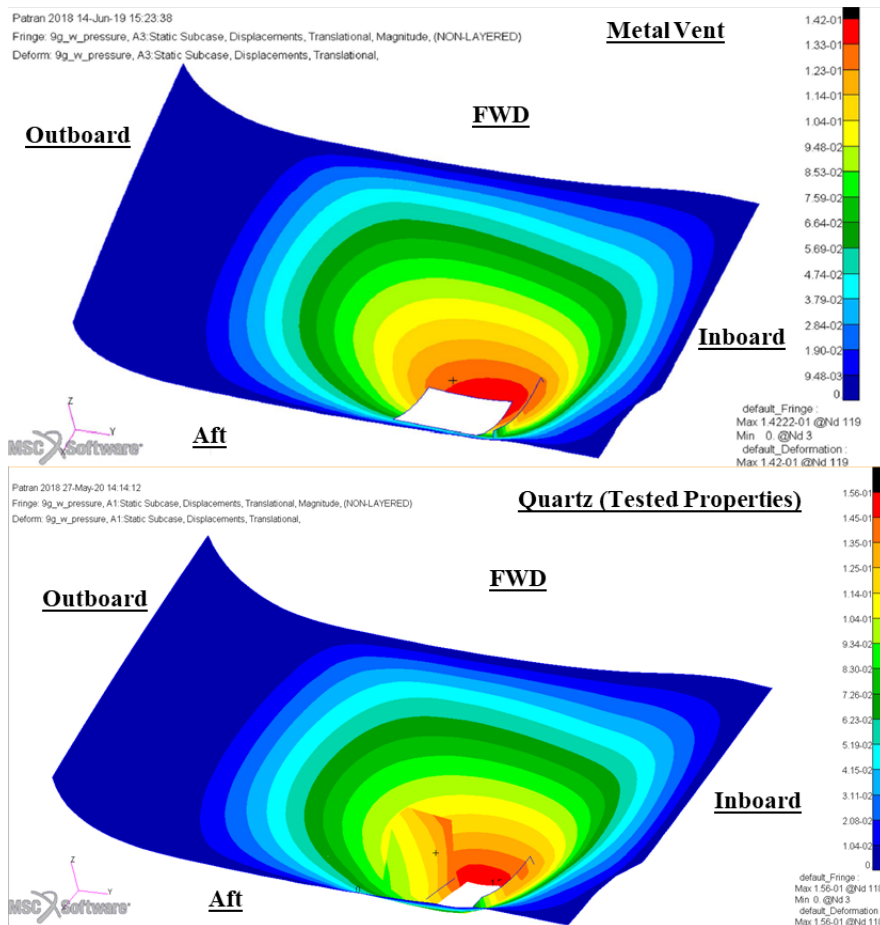


Figure 3.5: Comparison of Maximum Deflection [Ref. 24]

The maximum deflection of each design is located at the forward (FWD) and inboard most corner of the vent (the white region in Figure 3.5). A summary of the maximum deflection for every design is included in Table 3.11.

Table 3.11: Maximum Deflection

Dielectric Vent Panel Designs	Deflection (inches)	
	Full Assembly	Carbon Panel
Original GV [Ref. 24]	0.1422	0.139
Wet Layup S2-glass/epoxy [Ref. 24]	0.1479	0.145
Pre-Preg S2-glass/epoxy	0.1543	0.151
Tested Quartz	0.1555	0.152
Reported Quartz	0.1563	0.152
Sandwich Glass	0.1542	0.151

In Table 3.11, the deflection of the carbon panel only considers the OML carbon fuselage panel, and the deflection of the full assembly includes the OML carbon fuselage panel with the vent panel. In each case the modified dielectric ventilation panels created higher deflections than the original metal vent panel, including the wet layup S2-glass/epoxy panel from Reference 24. For final consideration, the maximum deflection of the panels designed for the analysis in this document were compared to the wet layup S2-glass/epoxy ventilation panel from Reference 24. This design was used as a baseline because it is an accepted design which has flown two missions [Refs. 24 and 25].

The panel which produced the highest maximum deflection is the quartz panel sized with the manufacturer’s properties, or the ideal properties. This design showed an increase of 0.0084” in the maximum deflection from the wet layup S2-glass/epoxy design. An increase of 0.0084” in the deflection represents a 5.6% increase in the maximum deflection for the system; however, this was considered an acceptable margin for the maximum deflection to increase because such a small increase in the deflection was considered smaller than the accuracy of the model given the assumptions about the boundary conditions and material properties. To provide assurance the system will not fail the stresses in the system were evaluated.

Moving forward the principal stresses in the OML carbon fuselage panel of each design were evaluated. As previously mentioned, the main design consideration was the stress distribution in the OML carbon fuselage panel. The following plots show the stress distribution in the carbon fuselage panel. Figure 3.6 is a representation of the changes in the maximum principal stress distribution between the metallic vent design and the dielectric vent design sized with the tested quartz properties, and Figure 3.7 represents the changes in the minimum principal stress.

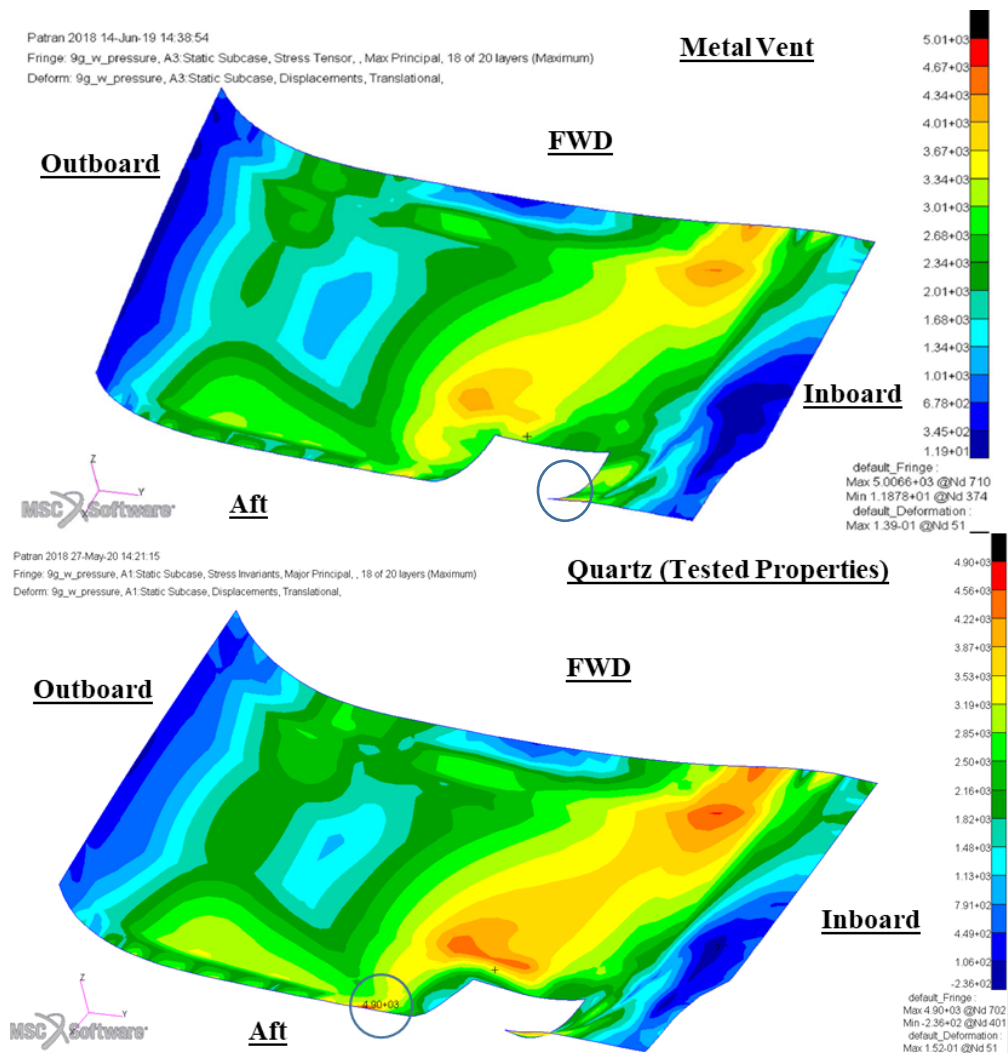


Figure 3.6: Comparison of Maximum Principal Stress Distribution [Ref. 24]

Figure 3.6 shows that the maximum principal stress in the design for the dielectric ventilation panel sized with the tested quartz properties had a similar stress distribution to the metallic vent design. The stress distribution in the quartz panel was also similar to the other dielectric vent panels including the wet layout

fiberglass panel design discussed in Reference 24. The most significant difference between the maximum principal stress distributions for each design was the location of the peak stress. In the quartz panel included in Figure 3.6, the peak stress is outboard of the location of the vent panel. For several of the other designs, including the wet layup fiberglass design this stress is located inboard of the vent panel [Ref. 24]. The change in the location of the peak stress was considered acceptable due to the decrease in the maximum principal stresses from the original metallic GV vent to each of the new designs.

The pre-preg S2-glass/epoxy, sandwich S2-glass/epoxy, and tested quartz designs showed the maximum principal stress increased over the wet layup S2-glass/epoxy design in Reference 24. The maximum principal stress in the S2-glass/epoxy sandwich design increased by 100 psi. The increase in the maximum principal stress in these systems was still considered acceptable because it remained lower than the maximum principal stress in the OML carbon fuselage panel with the original metallic vent design. The maximum principal stress in the panel made from the reported quartz properties was considered acceptable because the maximum principal stress decreased from both the original metallic GV design and the wet layup fiberglass design [Ref. 24].

Similar to the results for the maximum principal stress, Figure 3.7 shows that the minimum principal stress for the dielectric ventilation panel sized with the tested quartz properties had a similar stress distribution to the metallic vent design. The distribution of the minimum principal stress in the quartz panel was similar to each of the other dielectric ventilation panels including the wet layup S2-glass/epoxy panel design discussed in Reference 24, and the location of the minimum principal stress was maintained for each design. The main difference for the minimum principal stress was the magnitude.

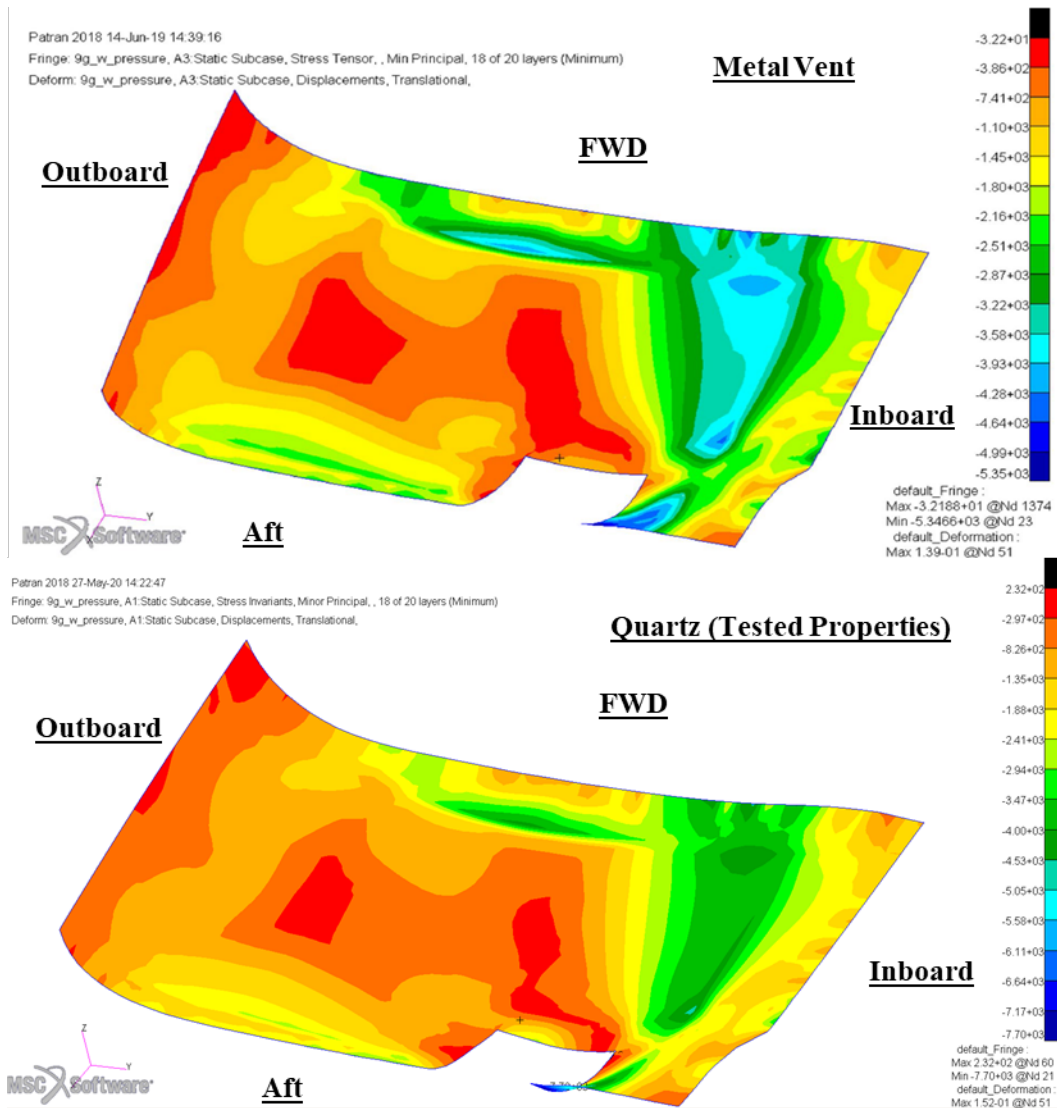


Figure 3.7: Minimum Principal Stress Distribution [Ref. 24]

Table 3.12 summarizes the maximum and minimum principal stresses of each design. This table shows that the maximum principal stresses for each modified ventilation panel were higher than those for the original dielectric S2-glass/epoxy vent design, however all the new designs maintained maximum stresses lower than the original GV design [Ref. 24]. Table 3.12 also shows that every design produced increased minimum principal stresses. The increase in the minimum principal stress was the result of increased bending around the vent panel due to the lower stiffness of the material used for sizing.

Table 3.12: Principal Stresses

Dielectric Vent Panel Designs	Principal Stresses for Carbon Panel (psi)	
	Maximum	Minimum
Original GV [Ref. 24]	5,007	-5,347
Wet Layup S2-glass/epoxy [Ref. 24]	4,889	-6,835
Pre-Preg S2-glass/epoxy	4,920	-7,750
Quartz (Tested Properties)	4,900	-7,700
Quartz (Reported Properties)	4,820	-7,700
Sandwich Glass	4,990	-6,970

While the minimum principal stresses increased from the original GV design and the wet layup S2-glass/epoxy design [Ref. 24], the minimum principal stresses in the new designs still created positive margins of safety in the OML carbon fuselage panel. The design which produced the largest increase in the minimum principal stress was the pre-preg S2-glass/epoxy design, showing an increase of -915 psi from the wet layup S2-glass/epoxy design from Reference 24. While, an increase of -915 psi for the minimum principal stress is a significant change this was considered acceptable because the margin of safety for this compressive stress was 2.44, where the margin of safety of the wet layup fiberglass design was 2.9. The reduced margin of safety for the new designs were considered acceptable due to the conservative material allowables used for the analysis. Also, the resulting maximum and minimum principal stresses in this section were primarily emphasized to illustrate that the stress distributions were maintained from the original OML carbon fuselage panel. Further analysis of the OML carbon fuselage panel is discussed in the next section to determine the effect of these increased minimum compressive stresses and to determine the critical loads and load types.

3.4.2 Analysis of the OML Carbon Fuselage Panel

This section discusses the critical stresses and corresponding margins of safety for the OML carbon fuselage panel. Table 3.13 includes the stresses, layer of critical stress, ply description, load type, and corresponding margins of safety for the critical elements in each design. The margins of safety for every load type were evaluated to determine the most critical load type and direction for each design. Full analysis results are included in Appendices F - I.

Table 3.13: Critical Stresses and Margins of Safety

Design	Layer	Orientation	Direction	Load Type	Stress (ksi)	MS
Metallic Vent [Ref. 24]	8	Core	-	Shear	-0.0356	2.52
Wet Layup S2-glass/epoxy [Ref. 24]	8	Core	-	Shear	-0.0369	2.40
Pre-Preg S2-glass/epoxy Vent	13	45	Transverse	Compression	-8.23	2.24
Tested Quartz Vent Panel	13	45	Transverse	Compression	-8.24	2.24
Reported Quartz Vent Panel	13	45	Transverse	Compression	-8.17	2.26
Sandwich S2-glass/epoxy Panel	8	Core (carbon)	-	Shear	-0.0375	2.34

Similar to the results discussed for the minimum and maximum principal stresses the S2-glass/epoxy sandwich panel provided the response most like the designs analyzed in Reference 24. For these three designs the critical loads were in shear and occurred in the core layer of the OML carbon fuselage panel. Specifically this region of the carbon fuselage panel is made with 14 layers of carbon and is in a location where the Rohacell 71-WF core is tapering down to the monolithic region of the carbon fuselage panel near the inboard edge of the carbon fuselage panel closest to the centerline of the fuselage.

The monolithic pre-preg S2-glass/epoxy design and both monolithic quartz designs showed the critical stress in a glass or quartz ply of the design instead of the core layer. The critical load type in these three designs is transverse compression, in a 45° ply, near the surface of the laminate (Ply 13 out of a 14 ply laminate). The location of the critical stress is the same in these three designs, occurring near the forward edge of the dielectric ventilation panel in the region of the carbon fuselage panel where the Rohacell 71-WF core is tapering down to the monolithic region of the panel. The change in the location of the critical stress was assumed to be driven by the varying stiffness in the materials and the laminate thicknesses.

As can be seen from Table 3.13 the critical elements and load types were not the same for every design. Since comparison of dis-similar load types does not provide an accurate portrayal of the difference between designs, Table 3.14 was included for a more direct comparison. Table 3.14 includes the critical margins of safety for the designs which deviated from the critical load type of the metallic and wet-layup fiberglass vents in Table 3.13 [Ref. 24].

Table 3.14: Stresses and Margins of Safety of Similar Elements

Design	Layer	Orientation	Direction	Load Type	Stress (ksi)	MS
Pre-Preg S2-glass/epoxy Vent	8	core	-	Shear	-0.0370	2.39
Tested Quartz Vent Panel	8	core	-	Shear	-0.0370	2.39
Reported Quartz Vent Panel	8	core	-	Shear	-0.0376	2.38

The margins of safety for the four designs being evaluated in this document were lower than the designs included in Reference 24, as seen in Tables 3.13 and 3.14; however, these designs were considered acceptable because their margins of safety remained rather high.

3.4.3 Modifications to RF Transparent Vent Panel

This section discusses the critical stresses and corresponding margins of safety for the designs of the dielectric ventilation panels. This section is only concerned with the results of the main vent panel made of the S2-glass, quartz, and core materials. Analysis of the metal doublers will be discussed in a later section. Table 3.15 includes the stresses, layer of critical stress, ply description, load type, and corresponding margins of safety for the critical elements in the radome panels for each design. The margins of safety for every load type were evaluated to determine the most critical load type and direction for each design. Full analysis results are included in Appendices F – I.

Table 3.15: Critical Stresses and Margins of Safety

Design	Layer	Orientation	Direction	Load Type	Stress (ksi)	MS
Wet Layup S2-glass/epoxy [Ref. 24]	1	0	Longitudinal	Tension	3.99	2.93
Pre-Preg S2-glass/epoxy Vent Panel	1	0	Longitudinal	Tension	4.27	4.01
Tested Quartz Vent Panel	11	45	-	Shear	0.879	4.08
Reported Quartz Vent Panel	11	45	-	Shear	0.999	5.61
Sandwich S2-glass/epoxy Panel	1	0	Longitudinal	Tension	9.01	0.74

For this analysis, only the wet layup S2-glass/epoxy design from Reference 24 was considered for comparison to the modified designs; comparison to the metallic vent design is not applicable. Table 3.15 shows that the three designs made of S2-glass/epoxy produced the same critical load type, while the two quartz panels were different. For the three glass designs the critical loads were in longitudinal tension and occurred in 0° plies. For the wet layup S2-glass/epoxy panel and the sandwich panel, the critical element

was in the region with 18 layers of glass directly adjacent to the recessed portion of the vent panel and the critical element for the pre-preg S2-glass/epoxy design was in the 12 ply recessed region of the vent panel. The pre-preg S2-glass/epoxy design responded similarly to the wet-layup S2-glass/epoxy design, as the critical stress in each of these designs is 4.27 ksi and 3.99 ksi, respectively. However, the margin of safety in the pre-preg S2-glass/epoxy design was higher than that of the wet-layup S2-glass/epoxy design, thus the pre-preg design was considered acceptable.

The sandwich panel produced a margin of safety significantly lower than any of the other designs. Even though the load type, and ply are the same as the monolithic fiberglass panels, the sandwich panel showed significantly higher stresses around the recessed portion of the vent. This was likely caused due to the lack of a tapered region in the core and the resulting high stress was caused by local bending due to the discrete thickness change. This critical stress is artificially high due to the discrete change in thickness and is therefore overly conservative. Since the discrete thickness change caused an artificially high stress and the design still maintained a positive margin of safety, it was still considered an acceptable design.

The monolithic quartz designs showed a critical shear stress instead of a critical tensile stress. The critical stresses in both quartz designs were in 45° plies, and located in the portion of the vent lip which has been tapered near the inboard aft corner of the vent panel. This illustrates that changing the material used in the design slightly shifted the load path. The change in the location of the critical stress was driven by the overall reduction in the stiffness of the vent cover; however these designs were considered acceptable because the critical margins of safety showed an improvement over the margin of safety for the wet layup design in Table 3.15.

Even though both quartz designs were considered acceptable based on their improved margins of safety in Table 3.15, the critical longitudinal tension elements of the quartz vent panels are included in Table 3.16. Similar to the analysis in Section 3.4.2, these extra stresses and margins of safety were included for a more direct comparison between all the designs.

Table 3.16: Stresses and Margins of Safety for Comparison

Design	Layer	Orientation	Direction	Load Type	Stress (ksi)	MS
Tested Quartz	1	0	Longitudinal	Tension	3.45	5.02
Reported Quartz	1	0	Longitudinal	Tension	3.99	7.11

The longitudinal tension stresses in Table 3.16 occurred in the same region as the tension stresses included in Table 3.15. The margins of safety for the three monolithic designs being evaluated in this document showed the modified designs were acceptable due to the increased margins of safety in Tables 3.15 and 3.16.

3.4.4 Review of the Modified Horn Antenna Bracket

This section discusses the critical stresses and corresponding margins of safety for the designs of the dielectric bracket for the 2 – 18 GHz horn antenna. Similar to the modifications made to the dielectric ventilation panels, the design of the dielectric brackets were also changed. The dielectric bracket was designed with the same laminate family and thickness as the recessed portion of the vent panel in each design. For the wet layup S2-glass/epoxy panel [Ref. 24], the dielectric bracket was made with a [0,45,0,45,0,45]_s stacking sequence resulting in an assumed laminate thickness of 0.108”. This stacking sequence was maintained for the designs sized with pre-preg S2-glass/epoxy, tested quartz properties, and the sandwich panel which was made with wet layup S2-glass/epoxy resulting in assumed laminate thicknesses of 0.1212”, 0.1368”, and 0.108”, respectively. The quartz panel sized with the manufacturer’s properties had a dielectric bracket with a [0,45,0,45]_s stacking sequence with an assumed laminate thickness of 0.084”. Table 3.17 includes the stresses, layer of critical stress, ply description, load type, and corresponding margins of safety for the critical elements of the horn antenna bracket in each design. The margins of safety for every load type were evaluated to determine the most critical load type and direction for each design. Full analysis results are included in Appendix F – I.

Table 3.17: Critical Stresses and Margins of Safety for Dielectric Horn Antenna Bracket

Design	Layer	Layer Orientation	Direction of Stress	Load Type	Stress (ksi)	MS
Wet Layup S2-glass/epoxy [Ref. 24]	2	45	Transverse	Tension	1.15	11.46
Pre-Preg S2-glass/epoxy Vent Panel	2	45	Transverse	Tension	1.06	18.37
Tested Quartz Vent Panel	2	45	Transverse	Tension	0.851	22.5
Reported Quartz Vent Panel	2	45	Transverse	Tension	1.55	18.93
Sandwich S2-glass/epoxy Panel	2	45	Transverse	Tension	3.53	3.06

Table 3.17 shows that all four new designs maintained the critical load type and direction of the wet layup fiberglass design from Reference 24. For each design, the critical loads included in Table 3.17 were located in the feet of the dielectric bracket, where it is secured to the dielectric ventilation panel. The three monolithic designs evaluated were considered acceptable designs for the dielectric bracket due to their increased margins of safety; however, the sandwich design showed a significant increase in stress in the dielectric bracket resulting in a drastic reduction of the critical margin of safety for the critical element, and the sandwich design was still accepted because the margins of safety for the monolithic wet layup fiberglass design was incredibly high (>10), meaning a reduction in the margin of safety is allowable without resulting in failure. Also, conservative material properties were used for these designs so a margin of safety of 3.06 provides a lower bound for the critical margin of safety in this design.

3.4.5 Review of the Vent Panel Metallic Doublers of the Dielectric Vent Panels

This section discusses the critical stresses and corresponding margins of safety in the metallic doublers used for each design. The design of the metallic doublers was not altered between designs. Table 3.18 includes the stresses, layer of critical stress, ply description, load type, and corresponding margins of safety for the critical elements of the metallic doublers in each design. The margins of safety for every load type were evaluated to determine the most critical load type and direction for each design. Full analysis results are included in Appendix F – I.

Table 3.18: Critical Stresses and Margins of Safety for the Metallic doublers

Design	Load Type	Stress (ksi)	MS
Wet Layup S2-glass/epoxy [Ref. 24]	Compression	-9.123	3.06
Pre-Preg S2-glass/epoxy Vent Panel	Tension	9.816	3.07
Tested Quartz Vent Panel	Tension	10.163	2.93
Reported Quartz Vent Panel	Tension	9.816	3.07
Sandwich S2-glass/epoxy Panel	Compression	-9.11	3.06

Table 3.18 shows that the sandwich S2-glass/epoxy panel produced a similar critical stress and load type to the wet layup S2-glass/epoxy design from Reference 24. This was considered a function of the similarities between the monolithic region of the sandwich panel and the design from Reference 24. Also in both designs the critical compressive stresses occurred at the aft inboard corner of the doubler. This design was considered acceptable due to the similarities between the stress and margins of safety of the critical element of this design and the wet layup fiberglass design from Reference 24.

The load type for the critical stresses in the three modified monolithic designs was tensile loading instead of compressive loading like the designs utilizing the wet layup material. These critical stresses occurred in the outboard corner of the region of the metallic doubler which was cutout to create the opening for the mesh vent. Even though these designs showed a different critical load type, the pre-preg S2-glass/epoxy and reported quartz designs were still considered acceptable due to increased margins of safety in the critical elements. However, the design sized with the tested quartz properties showed a reduced critical margin of safety.

The reduced margin of safety for the tested quartz was acceptable because the 90° corners modeled in Patran created unrealistic stress concentrations due to the simplicity of the Patran model used for this analysis. In reality the 90° corners in the model would be manufactured with rounded corners reducing the stress concentrations. So the results in Tables 3.18 are a conservative estimation of the margins of safety for these designs because of the stress concentrations due to the 90° corners.

Since the three modified monolithic designs experienced a different critical load type from the design in Reference 24, Table 3.19 was included to show the compressive stresses and corresponding

margins of safety for these designs. Similar to previous sections, these extra stresses and margins of safety were included for a more direct comparison between all the designs.

Table 3.19: Critical Stresses and Margins of Safety for Comparison of the Metallic doublers

For Comparison	Load Type	Stress (ksi)	MS
Pre-Preg S2-glass/epoxy Vent Panel	Compression	-9.027	3.09
Tested Quartz Vent Panel	Compression	-9.021	3.10
Reported Quartz Vent Panel	Compression	-8.99	3.11

The compressive stresses in Table 3.19 occurred in the same region of the panel as the compressive stresses included in Table 3.18. The margins of safety for the three monolithic designs being evaluated in this document showed the modified designs were acceptable due to the increased margins of safety from the wet layup S2-glass/epoxy design in Tables 3.18 to the results in Table 3.19.

3.4.6 Review of Metallic Shims for Dielectric Horn Bracket

This section covers the critical stresses and corresponding margins of safety in the metallic shims between the dielectric bracket and dielectric ventilation panels used for orienting the 2 – 18 GHz horn antenna nadir. The design of the metallic doublers was not altered from the design in Reference 24. Table 3.20 includes the stresses, layer of critical stress, ply description, load type, and corresponding margins of safety for the critical elements of the metallic shims in each design. The margins of safety for every load type were evaluated to determine the most critical load type and direction for each design. Full analysis results are included in Appendix F – I.

Table 3.20: Critical Stresses and Margins of Safety for the Metallic Shims

Design	Load Type	Stress (ksi)	MS
Wet Layup S2-glass/epoxy [Ref. 22]	Shear	0.918	17.88
Pre-Preg S2-glass/epoxy Vent Panel	Shear	0.963	16.99
Tested Quartz Vent Panel	Shear	0.937	17.50
Reported Quartz Vent Panel	Shear	0.891	18.45
Sandwich S2-glass/epoxy Panel	Shear	0.908	18.09

As seen in Table 3.20 the critical load type did not change between any of the designs. The position of the critical load was also maintained in the outboard most region of the metallic shims aft of the 2 – 18

GHz horn antenna. Table 3.20 shows that the margin of safety for both the pre-preg glass and the tested quartz designs reduced from the wet layup S2-glass/epoxy design from Reference 24; however, this was considered acceptable due to the large margins of safety.

3.4.7 Results for the Perimeter Bolts of the Modified Designs

This section discusses the critical fasteners in the OML carbon fuselage panels and their corresponding margins of safety. These fasteners are highlighted because the initial evaluation of the OML carbon fuselage panel with a metallic vent produced a negative margin of safety. Table 3.21 includes the load type and corresponding margins of safety for the critical fasteners in the OML carbon fuselage panel. The fastener loads for each design are included in Appendices F – I, along with sample calculations for the critical margins of safety.

Table 3.21: Critical Margins of Safety for OML Carbon Fuselage Panel

Design	Loading Type	Load (lbs.)	MS
Original GV [Ref. 24]	Bearing	662.5	-0.20
Wet layup Fiberglass [Ref. 24]	Bearing	613.0	-0.14
Pre-preg Fiberglass	Bearing	619.2	-0.15
Tested Quartz	Bearing	613.5	-0.14
Reported Quartz	Bearing	620.9	-0.15
Fiberglass Sandwich	Bearing	633.0	-0.16

The original design of the OML carbon fuselage panel with a metallic vent was analyzed because the OEM loads and stresses were not made available [Ref. 24]. The resulting negative margin of safety for the original GV design was in bearing and located in the OML carbon fuselage panel inboard of the vent panel. This fastener showed the highest stresses for all of the dielectric vent panel designs because there is only a single fastener in this region of the panel. The negative margin of safety was assumed to result from the conservative assumptions of the material properties used in the analysis, as the margin of safety would have been positive for the original design of the GV aircraft. Analysis by comparison was performed since the critical margin of safety at this fastener location was -0.2; and this margin of safety was used as the baseline for the new designs evaluated.

The critical margin of safety for the wet layup S2-glass/epoxy design was -0.14, at the same fastener location [Ref. 24]. This was considered an acceptable design because it showed improvement from the analysis of the original GV metallic vent design. This margin also provides padding for the design of the dielectric ventilation panel to be modified.

Based on the four new designs discussed in this document, three designs showed reduced margins of safety. These designs were considered acceptable because the critical bearing margin of safety still improved from the original GV metallic vent design; with the lowest margin of safety resulting from the sandwich glass design, while the design sized with the conservative quartz properties maintained the critical bearing margin of safety of the wet layup S2-glass/epoxy design.

3.5 Review of the MCoRDS Antenna Radome and Coupling Structure

The following analysis was performed to size the MCoRDS radome using the tested and reported quartz properties. The original design for the MCoRDS radome panel was made of pre-preg S2-glass/epoxy thus it did not need to be reanalyzed as was done for the dielectric ventilation panel. Although the 2 – 18 GHz horn antenna does not radiate through the much thicker OML radome panel, it does provide a representative structure for the electrical analysis that is much thicker than the vent cover. Also this radome design provides an opportunity to see the response of the quartz for a sandwich composite. The designs for the dielectric ventilation panels and antenna brackets for the 2 – 18 GHz horn antenna were maintained from Section 3.4 while sizing the MCoRDS radomes. The following analyses were performed in a comparative manner following the analysis method used to size the dielectric ventilation panels.

One analysis substituted the pre-preg S2-glass/epoxy sandwich used in the original design of the radome panel for a sandwich design utilizing the tested quartz properties with a cured ply thickness of 0.0114". This design maintained the laminate design outlined for the S2-glass/epoxy sandwich including a 24 layer layup with Rohacell 71-WF core, where the core tapered down to a monolithic 24 layer design around the perimeter of the radome panel for fastening the panel to the aircraft. Another analysis substituted the glass properties with the reported quartz properties. When substituting for the reported material properties the laminate design was again maintained with 24 layers with the core tapering down to the 24

layer monolithic region. The panel sized with the reported quartz properties was analyzed with a cured ply thickness of 0.0105” [Ref. 21].

Each design was sized by Load Cases 2 and 3 from Table 3.2 coupled with the 9g downward inertial load factor from Table 3.1. Each loading condition provided the critical condition for different components of the design. Every component of the final design was analyzed to ensure the new designs could withstand the loading conditions. The alternative designs for the dielectric vent panels which were carried over from Section 3.4, were reanalyzed to ensure they still produced positive margins of safety with the inclusion of the MCoRDS radome; however, since the analysis of the new dielectric ventilation panels were already discussed in the previous section, this section will focus on the design of the MCoRDS radome [Refs. 24 and 25]. The critical margins of safety were the perimeter fasteners of the carbon fuselage panel and analysis is included to verify the safety of the critical fasteners. The following results include a review of the panel stresses, stress distribution, max deflection of the panel and critical margins of safety across the entire design for the critical load case.

3.5.1 Overview of Comparison between Glass and Quartz Radome Designs

This section provides a review of the changes in maximum deflection between the different MCoRDS radome designs, as well as the maximum and minimum principal stresses in the MCoRDS radome. Each design discussed in the following section was designed based on maintaining the stress distribution of the MCoRDS radome. Load Cases 2 and 3 were used for the following analysis. As mentioned, only the most critical results are discussed in the following section.

Figure 3.8 shows the maximum displacement of the fully assembled design from Reference 23 and the new design utilizing the tested quartz properties with the corresponding dielectric ventilation panel discussed in Section 3.4. Figure 3.8 is the deflection of the full assembly relative to Load Case 3; this load case was used for the illustration because it resulted in the largest displacements. This figure helps illustrate the similar displacement distributions between the designs.

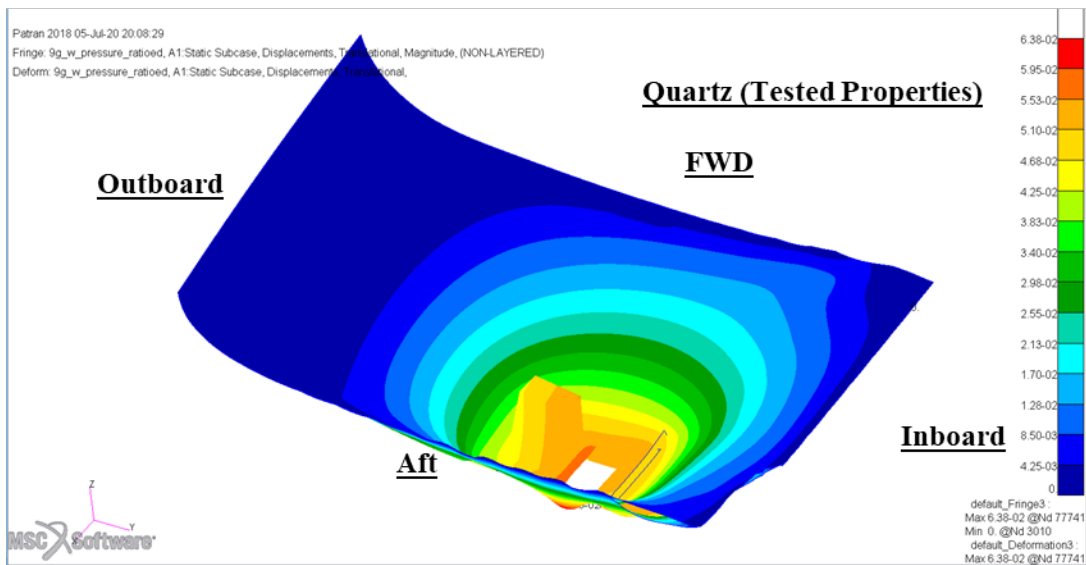
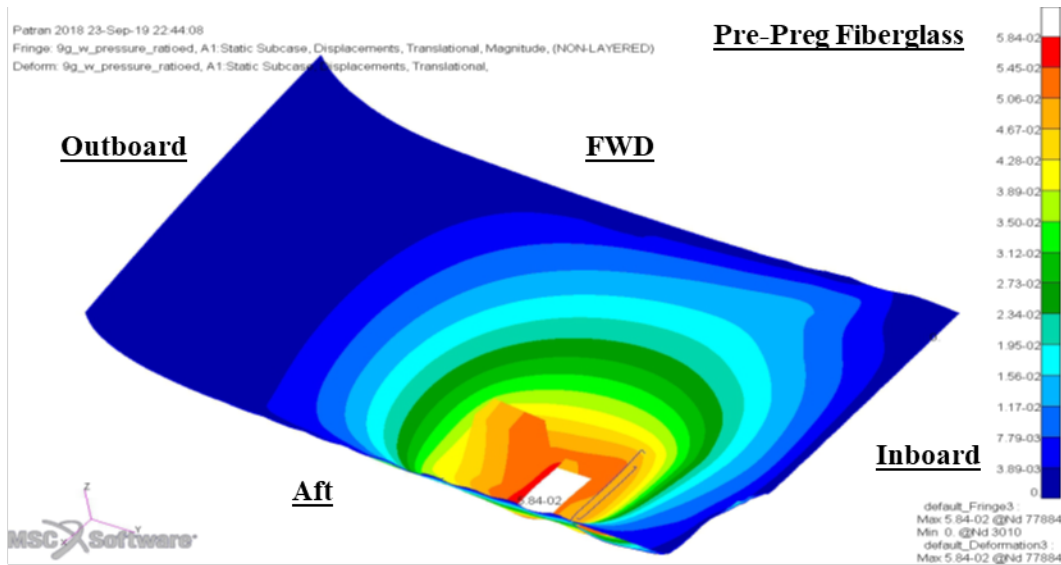


Figure 3.8: Comparison of Total Displacement for Full Assembly based on Load Case 3 [Ref. 25]

Figure 3.8 shows the maximum deflection has increased from 0.0584” in the pre-preg fiberglass design to 0.0638” in the design utilizing the tested quartz properties. Also the location of the maximum deflection was maintained for each design and is located in the dielectric ventilation panel mated to the carbon fuselage panel. Figure 3.9 shows the maximum deflection of the MCoRDS radome panel independent from the rest of the assembly for both the pre-preg S2-glass/epoxy design and the quartz design utilizing the tested properties.

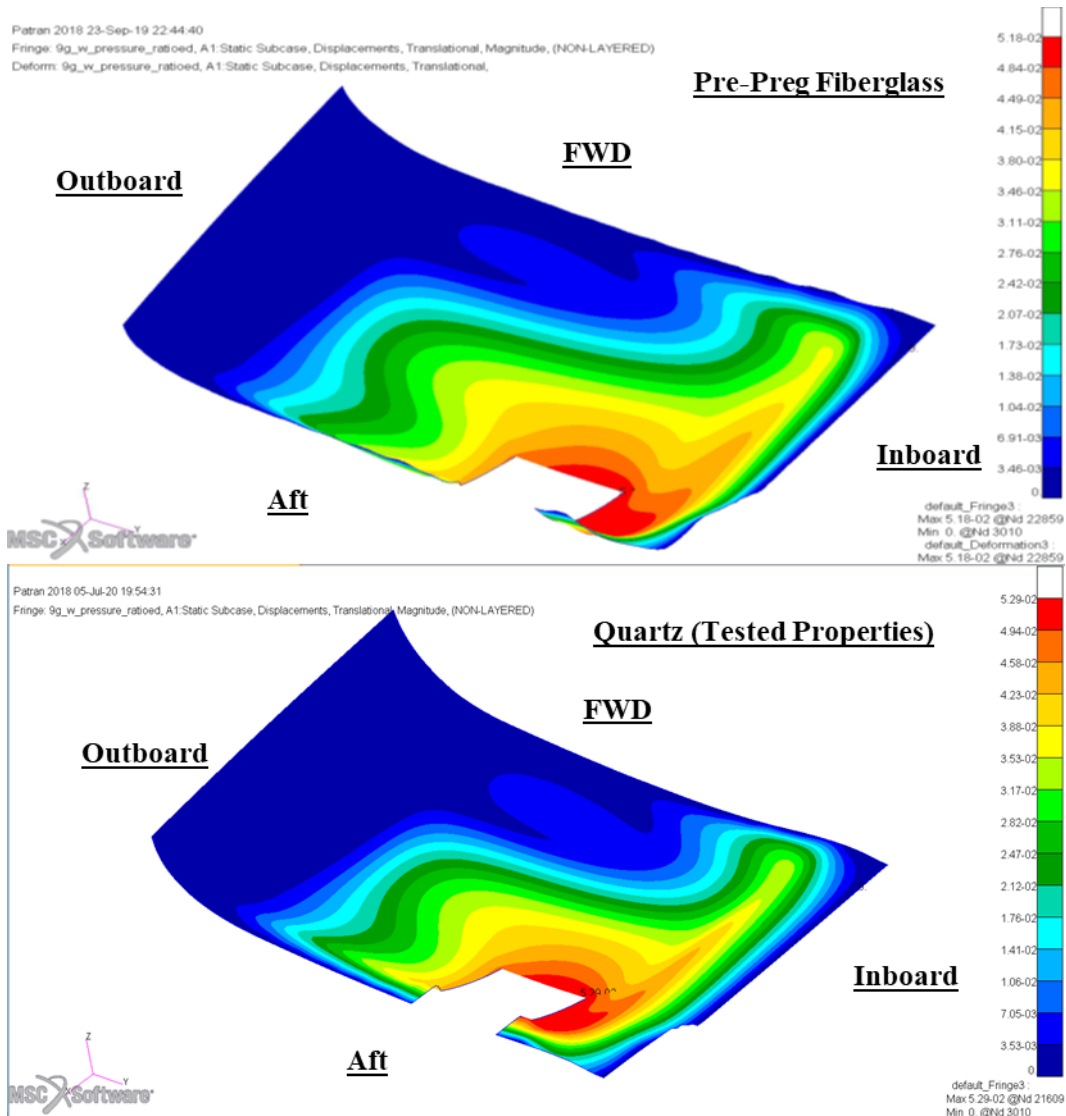


Figure 3.9: Comparison of Total Displacement of the Radome Panel based on Load Case 3 [Ref. 25]

Figure 3.9 shows that the deflection of the MCoRDS panel has shifted inboard causing increased deflections in a more concentrated area of the radome panel. Also the maximum deflection of each design in the MCoRDS radome panel is located near the forward inboard corner of the opening underneath the dielectric ventilation panel for the 2 – 18 GHz horn antenna; however, the maximum deflection for the full design is in the carbon fuselage panel. A summary of the maximum deflection for all three designs is included in Table 3.22.

Table 3.22: Maximum Displacement for MCoRDS Radome Designs sized using Load Case 3

MCoRDS Fairings	Full Assembly	MCoRDS Radome
Pre-Preg S2-glass/epoxy [Ref. 25]	0.0584	0.0518
Tested Quartz	0.0638	0.0529
Reported Quartz	0.0637	0.0498

In Table 3.22, the deflection of the MCoRDS radome only considers the MCoRDS radome, and the deflection of the full assembly includes the MCoRDS radome and the original OML carbon fuselage panel with the modified ventilation panels. The design utilizing the tested quartz properties produced the highest deflections. This design showed an increase of 0.0054” for the full assembly from the pre-preg fiberglass design, and an increase 0.0011” when only looking at the MCoRDS radome panel. This was considered an acceptable margin for the maximum deflection to increase because such a small increase in the deflection is within the accuracy of the model given the assumptions about the boundary conditions and material properties.

The design sized with the reported quartz properties produced a similar maximum displacement for the full assembly to that of the tested quartz properties. The similar deflection between the two quartz designs agrees with the similar deflections reported in Section 3.4. Similar to the design utilizing the tested quartz properties the increased deflection was considered acceptable because it was considered within the accuracy of the model.

Also the design utilizing the reported quartz properties produced a smaller maximum deflection than either of the other designs for the MCoRDS radome, and was therefore considered an acceptable design. The improvement from the pre-preg S2-glass/epoxy to the reported quartz was assumed to be a function of the increased thickness of the quartz material, as the cured ply thickness reported for the quartz is 0.0105” and for fiberglass it is 0.0101”. This was considered the source of the reduced deflection since the actual material Young’s modulus reported for the quartz was lower than the Young’s modulus reported for the S2-glass/epoxy. Also, the increased maximum deflection seen for the design utilizing the tested quartz properties was considered to be a function of the significantly reduced Young’s modulus, because the cured ply thickness was even higher than the reported cured ply thickness.

As the previous discussion was for the designs sized by Load Case 3, Table 3.23 was included to show the results for Load Case 2.

Table 3.23: Maximum Displacement for MCoRDS Radome Designs sized using Load Case 2

MCoRDS Fairings	Full Assembly	MCoRDS Radome
Pre-Preg S2-glass/epoxy [Ref. 25]	0.0418	0.0418
Tested Quartz	0.0425	0.0425
Reported Quartz	0.0403	0.0398

Table 3.23 shows the design sized with the tested quartz properties under Load Case 2 had a similar response to Load case 3; however, the radome sized with the reported quartz properties had a different response showing improved results for both the full assembly and the deflection of the MCoRDS radome on its own. Again this reduced deflection was considered a function of the increased cured ply thickness used while sizing the radome with the reported quartz properties. Again, the increased maximum deflection seen for the design utilizing the tested quartz properties was considered to be a function of the significantly reduced Young’s modulus, because the cured ply thickness was even higher than the reported cured ply thickness.

The maximum and minimum principal stresses were also compared similar to the analysis discussed in Section 3.4. Figure 3.10 shows the maximum principal stress of the design sized with the tested quartz properties compared to the maximum principal stress of the pre-preg S2-glass/epoxy design from Reference 25, and Figure 3.11 shows the minimum principal stresses.

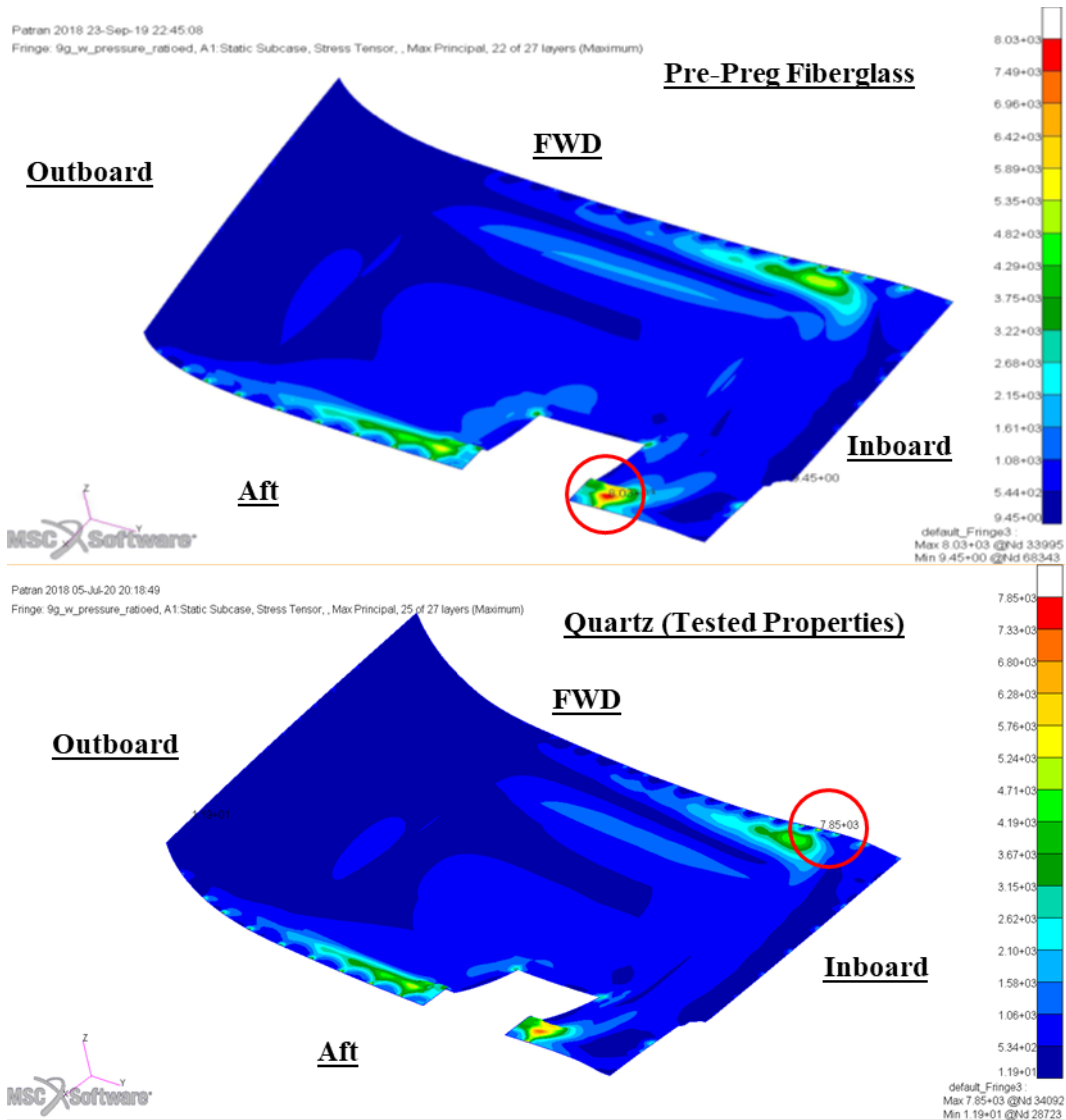


Figure 3.10: MCoRDS Dielectric Radome Maximum Principal Stress for Load Case 3 [Ref. 25]

The main difference between the maximum principal stresses of the MCoRDS radome design was the location of the maximum principal stress. All three designs showed high stresses in the inboard section of the radome panels, but for the pre-preg S2-glass/epoxy design the peak stress was located in the aft inboard section of the panel near where the rib structure is fastened to the panel, and the peak stress in both quartz designs is located in the forward inboard section of the radome panel. The peak stresses are circled for each design in Figure 3.10. The change in the location of the maximum principal stress was considered a function of the different stiffness values and the thicknesses of the quartz materials used to size the panels, because all three designs used the same laminate designs for the MCoRDS radome and rib structures.

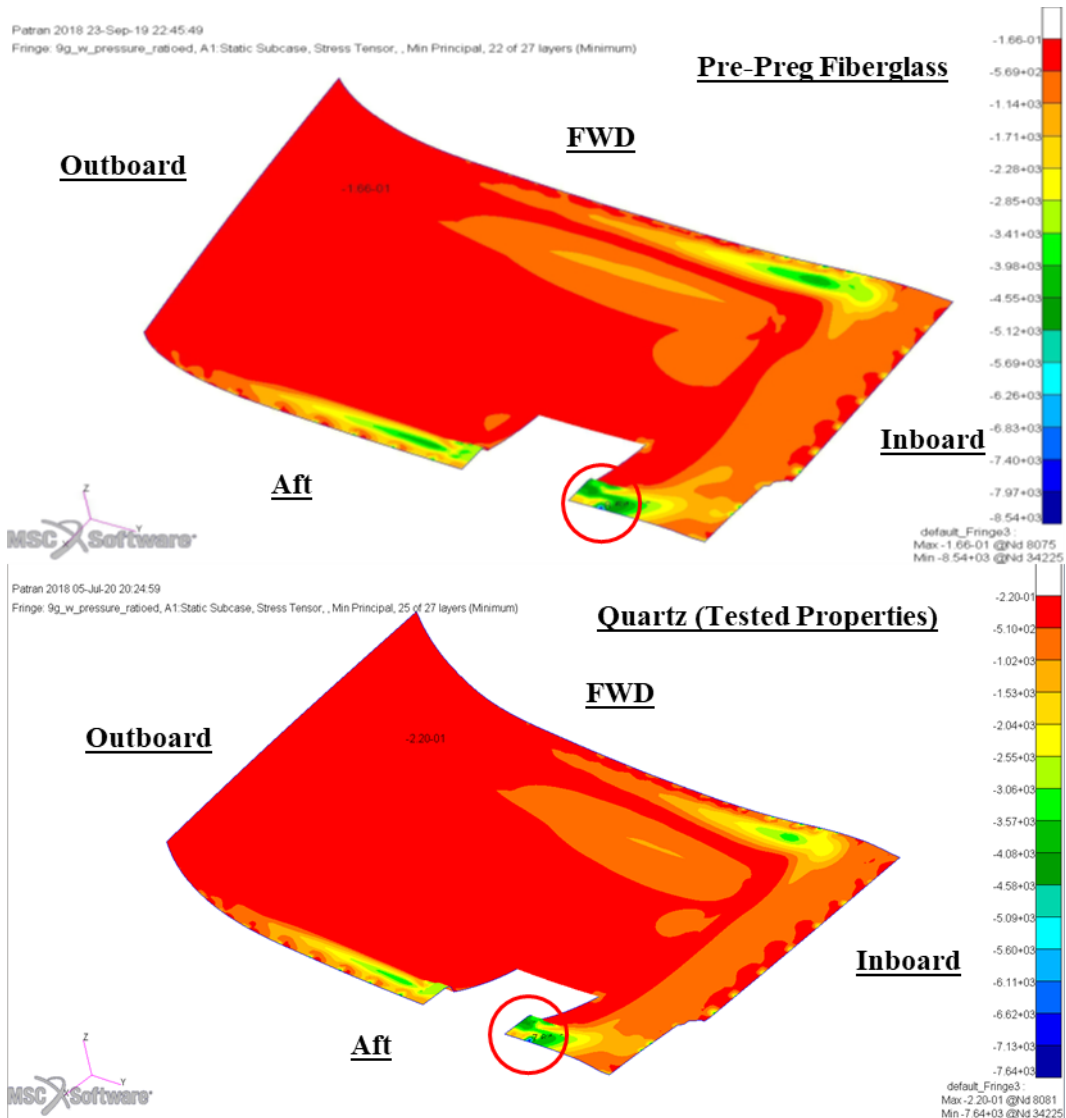


Figure 3.11: MCoRDS Dielectric Radome Minimum Principal Stresses for Load Case 3 [Ref. 25]

Figure 3.11 shows that the minimum principal stress in the MCoRDS radome design utilizing the tested quartz properties has a similar stress distribution to that of the pre-preg S2-glass/epoxy design. The same comment could be made for the design sized with the reported quartz properties. The main difference for the minimum principal stress was the magnitude; as the design sized with the tested quartz properties showed a decrease of 900 psi in the peak stress over the pre-preg S2-glass/epoxy design, while the design sized with the reported quartz properties showed an increase of 390 psi in the minimum principal stress from the pre-preg S2-glass/epoxy design. Table 3.24 summarizes the maximum and minimum principal stresses of each design for the MCoRDS radome based on Load Case 3.

Table 3.24: Principal Stresses in the MCoRDS Radome Panels sized with Load Case 3

Design	Maximum (psi)	Minimum (psi)
Pre-Preg S2-glass/epoxy [Ref. 25]	8,030	-8,540
Tested Quartz	7,850	-7,640
Reported Quartz	8,370	-8,930

As the radome panels sized with each set of material properties maintained similar designs the only differences were the cured ply thickness of the laminates and the stiffness of the materials. The reduced stiffness in the tested quartz design was assumed to be the cause for the reduced stresses in the radome structure. The lower stiffness caused the load to shift, causing adjacent structures to carry more load; however, the change in stress was not that high thus the change was deemed acceptable. Therefore, the design sized with the tested quartz properties was a viable design.

The design sized with the reported quartz properties showed the principal stresses increase from the S2-glass/epoxy design. The increased cured ply thickness was the cause for the increased principal stresses in the panel sized with the reported quartz properties, as the reported stiffness value was lower than that for glass. Similar to the design of the dielectric ventilation panel, the perimeter fasteners securing the radome to the GV aircraft were the critical elements of this design. A review of the critical fastener margins of safety is included in Section 3.5.4 to verify this design showed acceptable margins of safety.

The MCoRDS radome panels were also sized by Load Case 2 and the resulting maximum and minimum principal stresses are included in Table 3.25. The results in Table 3.25 show that the maximum and minimum stresses improved for both quartz designs from that of the pre-preg S2-glass/epoxy design.

Table 3.25: Principal Stresses in the MCoRDS Radome Panels sized with Load Case 2

Design	Maximum (psi)	Minimum (psi)
Pre-Preg S2-glass/epoxy [Ref. 25]	7,500	-6,450
Tested Quartz	7,280	-6,040
Reported Quartz	7,220	-6,410

This table shows that the maximum and minimum stresses for both of the quartz MCoRDS radome designs sized with Load Case 2 showed slight improvement over the pre-preg S2-glass/epoxy design.

Comparing the results in Tables 3.24 and 3.25 also helps verify that the structure was sized by Load Case 3 due to the increased stresses in the new designs in Table 3.24. The results discussed in the following sections will show the critical stresses and margins of safety for components added to the GV aircraft during the design of the MCoRDS radome.

3.5.2 Sizing for the MCoRDS Dielectric Radome Panel

This section discusses the critical stresses and corresponding margins of safety for the MCoRDS radome designs. Table 3.26 includes the stresses, layer of critical stress, ply description, load type, and corresponding margins of safety for the critical elements in each design. The margins of safety for every load type were evaluated to determine the most critical load type and direction for each design. Full analysis results are included in Appendices J and K.

Table 3.26: Critical Stresses and Margins of Safety for the MCoRDS Radome Designs

Design	Layer	Layer Orientation	Direction of Stress	Load Type	Load Case	Stress (ksi)	MS
Pre-Preg S2-glass/epoxy [Ref. 25]	23	45	Transverse	Tension	2	11.83	0.13
Tested Quartz	23	45	Transverse	Tension	2	9.17	0.42
Reported Quartz	1	0	Transverse	Compression	2	-9.64	0.91

The results in Table 3.26 show deviations from the results discussed for the maximum and minimum principal stresses. In this case the radome structure was sized by Load Case 2, and the design sized with the tested quartz properties was the most similar to the pre-preg S2-glass/epoxy design. For these two designs the critical loads were in transverse tension and occurred in the monolithic region of the radome panel at the forward edge of the structure and near the inboard edge of the radome.

The MCoRDS radome panel sized with the reported quartz properties showed the critical stress in the same region of the radome but the compression load created the critical load case in transverse compression. This critical load case was selected based on the allowable compressive strength of the material causing the compression load to create the lowest margin of safety however, the two quartz designs created similar stresses in the panels.

Since comparison of dis-similar loads does not provide an accurate portrayal of the difference between designs Table 3.27 was included for a more direct comparison. Table 3.27 includes the critical margins of safety for the designs which deviated from the critical load type of the pre-preg S2-glass/epoxy radome design in Table 3.26.

Table 3.27: Critical Stress and Margin of Safety for Comparison

Design	Layer	Layer Orientation	Direction of Stress	Load Type	Load Case	Stress (ksi)	MS
Reported Quartz	23	45	Transverse	Tension	2	9.52	1.10

The transverse tension stress in Table 3.27 occurred in the same region as the transverse tension stresses in Table 3.26. The margins of safety for the two modified MCoRDS radome designs showed improvement from the pre-preg S2-glass/epoxy design from Reference 25, so these designs were considered acceptable based on the increased margins of safety.

3.5.3 Sizing of Rib Structure

This section discusses the critical stresses and corresponding margins of safety for the rib structure coupling the MCoRDS radome to the dielectric ventilation panel discussed in Section 3.4. Table 3.28 includes the stresses, layer of critical stress, ply description, load type, and corresponding margins of safety for the critical elements in each design. Table 3.28 also shows that the rib structure was sized by Load Case 3. The margins of safety for every load type were evaluated to determine the most critical load type and direction for each design. Full analysis results are included in Appendices J and K.

Table 3.28: Critical Stresses and Margins of Safety for the Rib Structure

Design	Layer	Layer Orientation	Direction of Stress	Load Type	Load Case	Stress (ksi)	MS
Pre-Preg S2-glass/epoxy [Ref. 25]	14	0	Transverse	Compression	3	-5.11	3.12
Tested Quartz	14	0	Transverse	Compression	3	-4.15	3.43
Reported Quartz	14	0	Transverse	Compression	3	-4.89	4.05

Table 3.28 shows that both of the new quartz designs maintained the critical load type and direction of the pre-preg S2-glass/epoxy design from Reference 25. For each design, the critical loads included in Table 3.28 were located at the inboard aft corner of the rib structure on the flange where it is secured to the

MCoRDS radome. Based on the sizing of the rib structure, both quartz designs were considered acceptable designs based on the increases seen for the critical margins of safety.

3.5.4 Perimeter Bolt Loads

The design of the MCoRDS radome panel and corresponding rib structure was done in a comparative manner. Included in Reference 25 is a review of the fastener loads and margins of safety for each component of the design. These margin of safety calculations were repeated for each of the new radome panels discussed in Sections 3.5.1 – 3.5.3, for both Load Cases 2 and 3.

For the design sized with the tested quartz properties and Load Case 2, three critical fasteners were found in the original OML carbon fuselage, while one critical fastener was found in the quartz radome. Similar to the S2-glass/epoxy radome panel sized in Reference 25, this design produced negative margins of safety for the critical bearing loads. The critical margin of safety for the S2-glass/epoxy design was found to be -0.383 in the OML carbon fuselage panel, and this was considered acceptable because -0.383 is a higher margin of safety than the original GV carbon fuselage panel flown at OEM configuration using the considered analysis assumptions; the original GV carbon fuselage panel produced a margin of safety of -0.420 [Ref. 25]. Table 3.29 shows the critical margins of safety for the design sized with the tested quartz properties and Load Case 2.

Table 3.29: Margins of Safety for Critical Fasteners in Tested Quartz Design under Load Case 2

Location	Total Load (Lbs.)	Bearing MS	Allowable load (Lbs.)	Allowable MS
OML Carbon Fuselage Panel	591.5	-0.35	662.1	-0.42
OML Carbon Fuselage Panel	487.4	-0.21	688.8	-0.44
OML Carbon Fuselage Panel	573.6	-0.33	631.1	-0.39
Radome Panel	573.6	0.58	-	-

Similar to the procedure in Reference 25, allowable margins of safety were determined at each fastener location based on the loads from the original GV carbon fuselage panel flown at OEM configuration. The margins of safety in the carbon fuselage panel were considered acceptable because they were higher than the allowable margins of safety. For the MCoRDS radome panel, a bushing was added to increase to the fastener hole to produce a positive margin of safety [Ref. 25]. For the S2-glass/epoxy design

in Reference 25, a 0.34” bushing was added to each of the fastener locations which produced a negative margin of safety; one critical margin of safety in the S2-glass/epoxy panel was -0.158 and adding the bushing increased this margin of safety to 0.53. For this design, a 0.34” diameter bushing was placed at the fastener hole in the MCoRDS radome panel and the margin of safety was found to be 0.58. Since the margins of safety in the OML carbon fuselage panel and the MCoRDS radome (with bushings) are greater than the allowable margins of safety, this design was acceptable under Load Case 2. Table 3.30 show the critical margin of safety for the design sized with the tested quartz properties and Load Case 3.

Table 3.30: Margins of Safety for Critical Fasteners in Tested Quartz Design under Load Case 3

Location	Total Load (Lbs.)	Bearing MS	Allowable load (Lbs.)	Allowable MS
OML Carbon Fuselage Panel	785.5	-0.33	662.1	-0.42

The same process was used to determine the allowable margin of safety for the tested quartz sized under Load Case 3. Since the bearing margin of safety was found to be greater than the allowable, the design was considered acceptable under Load Case 3.

Tables 3.31 and 3.32 show the critical margins of safety for the design sized with the reported quartz properties and Load Cases 2 and 3, respectively. For Load Case 2, three critical margins of safety were found in the original OML carbon fuselage panel. Due to the bearing margin of safety being greater than the allowable, this design was considered acceptable under Load Case 2.

Table 3.31: Margins of Safety for Critical Fasteners in Reported Quartz Design under Load Case 2

Location	Total Load (Lbs.)	Bearing MS	Allowable load (Lbs.)	Allowable MS
OML Carbon Fuselage Panel	471.1	-0.19	662.1	-0.42
OML Carbon Fuselage Panel	500.6	-0.23	688.8	-0.44
OML Carbon Fuselage Panel	588.8	-0.348	631.1	-0.39

Included in Table 3.32, the bearing margin of safety is greater than the allowable, therefore the design sized with the reported quartz properties was also considered acceptable under Load Case 3.

Table 3.32: Margins of Safety for Critical Fasteners in Reported Quartz Design under Load Case 3

Location	Total Load (Lbs.)	Bearing MS	Allowable load (Lbs.)	Allowable MS
OML Carbon Fuselage Panel	808.5	-0.35	662.1	-0.42

3.6 Summary of Structural Analysis

As mentioned the structural analysis discussed in the previous sections produced designs for both the dielectric ventilation panel and the MCoRDS radome utilizing both S2-glass/epoxy and quartz materials. Similarly analysis was performed to size both monolithic and sandwich designs utilizing wet-layup S2-glass/epoxy and 0.25” Rohacell 71-WF core. Sizing of the four modified dielectric ventilation panels was performed to establish the different thicknesses required while using each material, while the analysis of the MCoRDS radome was performed to determine the effect of the quartz when applied to a much thicker design. Each of the four modified vent panels and two modified MCoRDS panels discussed in the previous sections showed comparable displacements and stresses to the designs discussed in References 24 and 25. The slight increase in the displacements and stresses in each design were considered acceptable due to the increased margins of safety of the modified designs and the accuracy of the models used for this analysis.

While we could not rely on this sizing to establish an airworthy quartz radome, as was done for the S2-glass/epoxy, note that is not the intent of this thesis. Instead, this comparative sizing is done to establish realistic bounds on likely thickness and families for future structures that might be sized with such quartz materials, to investigate whether the electrical performance benefits are justified. Hence it was critical that such effort was invested for comparable sizing using the material assumptions outlined in Chapter 2. The structural analysis in the previous sections illustrates that each of the modified dielectric ventilation panels would be viable alternative designs using the developed quartz material properties; similarly viable are the two MCoRDS radome designs, based on the critical margins of safety of each design. In the following Chapters, the designs sized by the structural analysis in the previous chapter are compared based on their electrical performance.

4. EM Characterization Using Boundary Value Problem

While the design of the original dielectric ventilation panel allowed for satisfactory radar performance, there is interest in investigating possible electrical improvements based on the alternate designs studied in Chapter 3. In this section the Boundary Value Problem (BVP) approach will be used to estimate the transmission coefficient for each of the designs. To validate the BVP solution, several representative panels were fabricated and tested in an anechoic chamber. Due to the limited amount of quartz material available, there was not enough material to fabricate all the designs from Chapter 3, thus four representative designs were first examined and validated. Section 4.1 first describes the representative panel designs that were analyzed using the BVP technique and subsequently validated through anechoic chamber testing. Section 4.2 presents the BVP theory and analysis of the representative panels, and Section 4.3 presents the chamber results for the panels.

4.1 EM Analysis of Representative Panels

Electrical performance of the quartz and glass designs were compared by manufacturing and analyzing panels with similar thicknesses. For these tests three panels were manufactured based on the thickness of recessed portion of the original glass vent panel. Two of the panels were fabricated from S2-glass/epoxy, one quasi-isotropic and one with all 0/90 plies, while the third was fabricated from quartz. Table 4.1 provides a summary of the panels manufactured for electrical testing.

Table 4.1: Physical Characteristics of Panels Manufactured for Electrical Testing

Panels	Stacking Sequence	Thickness (inches)	Panel Sizes (inch x inch)
Family Glass	[0,45,0,45,0,45] _s	0.1215	8 x 8
Family Glass	[0] ₁₂	0.1220	8 x 8
Quartz	[0,45,0,45,0] _s	0.1100	7.5 x 5.5
Sandwich	[0,45,core,45,0]	0.2850	8 x 8

Table 4.1 includes the sandwich design which was analyzed in Chapter 3 and did not maintain the thickness of the other panels. However, the main purpose of this panel was to test and validate the difference in electrical performance between a monolithic panel and a sandwich panel, so the increased thickness did

not present a problem. Table 4.1 also includes a monolithic S2-glass/epoxy design made with all 0/90 plies. This design was created because the BVP is not dependent on fiber orientation and there was interest in evaluating if this could be verified through anechoic chamber testing or if chamber testing would show a dependence on fiber orientation. The electrical material properties used in the BVP method are included in Table 4.2 [Refs. 21, 22, and 29].

Table 4.2: Electrical Properties for EM Material Trade Study

Material	ϵ_r	Loss Tangent	CPT/Thickness (inches)
S2-glass 6781/DPL862 Epoxy [Ref. 22]	4.7	0.014	0.0101
Quartz [Ref. 21]	3.244	0.004	0.011
Rohacell 71-WF [Ref. 29]	1.09	0.00265	0.25

4.2 Theoretical Panel Transmissivity

The BVP method is used to analyze transmissions and reflections for flat multilayer laminates. For the BVP, the total transmitted and reflected power is a function of the polarization, the signal incidence angle with respect to the surface of the panel, the thickness of the panel, and the panel material properties (dielectric constant and loss tangent). The polarization can be perpendicular polarization or parallel polarization. Perpendicular polarization is observed when the E-field is perpendicular to the incidence plane and the H-field is in the incidence plane. Parallel polarization is observed when the E-field is in the incidence plane and the H-field is perpendicular to the incidence plane. The impedance for a given polarization can be found using Equations (4-1) and (4-2), from Reference 13.

$$Z_i = \frac{\cos(\theta)}{\sqrt{\epsilon_{r_i} - \sin^2(\theta)}} \quad (4-1)$$

$$Z_i = \frac{\sqrt{\epsilon_{r_i} - \sin^2(\theta)}}{\epsilon_{r_i} * \cos(\theta)} \quad (4-2)$$

For these equations, Z_i is the impedance for each layer, θ is the signals incidence angle with respect to the surface of the panel, and ϵ_{r_i} is the relative permittivity of each layer. The subscript, i , represents the i^{th} layer in a laminate if the material had changed between adjacent layers, as is the case for the glass panel

with the Rohacell core. Figure 4.1 provides an illustration for a multilayered laminate showing how the properties can differentiate when the material has changed between layers.

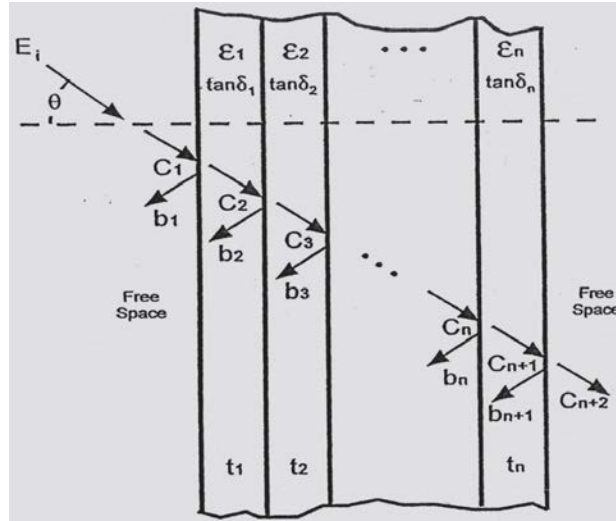


Figure 4.1: Multilayer Dielectric Wall for Boundary Value Analysis [Ref. 13]

For this analysis and the following anechoic chamber testing the incidence angle is 0° , which is representative of the antenna orientation for most CReSIS antenna installations. Use of a 0° incidence angle causes Equations (4-1) and (4-2) to simplify to Equations (4-3) and (4-4), respectively [Ref. 13]. Equations (4-3) and (4-4) are thus equivalent for the 0° incidence case.

$$Z_{i,\theta=0} = \frac{\sqrt{\epsilon_{r_i} - \sin^2(\theta)}}{\epsilon_{r_i} \cdot \cos(\theta)} = \frac{1}{\sqrt{\epsilon_{r_i}}} \quad (4-3)$$

$$Z_{i,\theta=0} = \frac{\sqrt{\epsilon_{r_i} - \sin^2(\theta)}}{\epsilon_{r_i} \cdot \cos(\theta)} = \frac{\sqrt{\epsilon_{r_i}}}{\epsilon_{r_i}} \quad (4-4)$$

Using the BVP method to provide an estimate of the electrical performance for each panel can show which design will provide the best transmissions and reflections. The reflection and transmission coefficients at the layer boundaries are calculated with Equations (4-5) and (4-6), respectively [Ref. 13].

$$R_i = \frac{Z_i - Z_{i-1}}{Z_i + Z_{i-1}} \quad (4-5)$$

$$T_i = 1 - R_i \quad (4-6)$$

These reflection and transmission coefficients feed into the solution for the BVP for a multilayer laminate as represented by Equation (4-7) [Ref. 13].

$$\begin{bmatrix} C_1 \\ B_1 \end{bmatrix} = \left[\prod_{i=1}^N \frac{1}{T_i} \begin{bmatrix} e^{j\gamma_i t_i} & R_i * e^{-j\gamma_i t_i} \\ R_i * e^{j\gamma_i t_i} & e^{-j\gamma_i t_i} \end{bmatrix} \right] \left(\frac{1}{T_{N+1}} \right) \begin{bmatrix} 1 & R_{N+1} \\ R_{N+1} & 1 \end{bmatrix} \begin{bmatrix} C_{N+2} \\ B_{N+2} \end{bmatrix} \quad (4-7)$$

In Equation (4-7), C_1 corresponds to the forward propagating or transmitted wave as seen in Figure 4.1, while B_1 is the reverse propagating or reflected wave. Also, $N+1$ is representative of the final layer because C_1 , and B_1 correspond to the free space before the signal reaches the panel, and $N+2$ represents the free space on the exiting side of the panel [Ref. 13]. Also in Equation (4-7) is the variable t_i , which is the thickness of the i^{th} layer of the laminate and γ_i is the propagation constant in the i^{th} layer normal to the boundary and given by Equation (4-8) [Ref. 13].

$$\gamma_i = k_0 * \sqrt{\epsilon_{ri}} * \cos(\Theta) \quad (4-8)$$

The variable k_0 is the wave number in free space equivalent to the ratio $2\pi/\lambda$, where λ the wavelength of the incident signal. Finally, ϵ_{ri} is the permittivity for the i^{th} layer accounting for the loss tangent ($\tan\delta$) and given by Equation (4-9) [Ref. 13].

$$\epsilon_{ri} = \epsilon_r * (1 - j\tan\delta) \quad (4-9)$$

Equation (4-9) shows that ϵ_{ri} consists of a real part (ϵ_r) and an imaginary part ($\epsilon_r * j\tan\delta$) defined by the loss tangent.

After performing the matrix multiplication, Equation (4-7) simplifies to Equation (4-10) [Ref. 13].

$$\begin{bmatrix} C_1 \\ B_1 \end{bmatrix} = \begin{bmatrix} A_{11} & A_{12} \\ A_{21} & A_{22} \end{bmatrix} \begin{bmatrix} C_{N+2} \\ B_{N+2} \end{bmatrix} \quad (4-10)$$

The reflected and transmitted power is then calculated by Equations (4-11) and (4-12), respectively, from Reference 13.

$$|R|^2 = \frac{A_{21}}{A_{11}} \quad (4-11)$$

$$|T|^2 = \frac{1}{A_{11}} \quad (4-12)$$

Figure 4.2 is the transmissivity (Eq. 4-12) on a decibel scale for each of the three panel designs. As mentioned, the BVP method is not dependent on the fiber orientation of the layers within the laminate, so Figure 4.2 only includes results for one monolithic S2-glass/epoxy panel, as the 25/50/25 family and the 0/90 panels result in similar solutions.

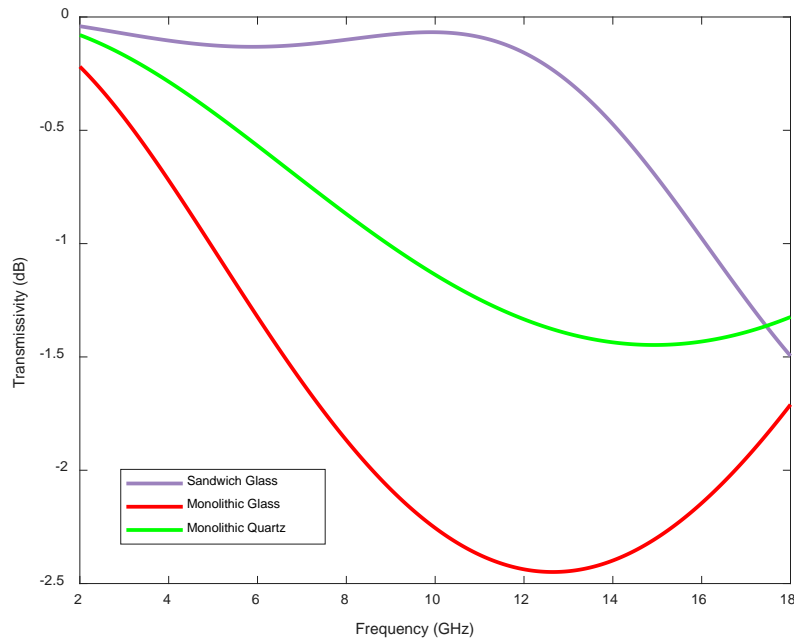


Figure 4.2: Transmitted Power Produced from the BVP method

These results show that the glass sandwich design, [0,45,core,45,0], performed exceptionally well from 2 – 12 GHz, while the performance degraded from 12 – 18 GHz. However, the sandwich design still maintains the best performance of the designs evaluated for every frequency below 16 GHz.

The monolithic quartz panel did not perform as well as the S2-glass/epoxy sandwich showing a maximum reduction in the transmitted signal between the two designs around 10 – 12 GHz. The largest separation between the sandwich design and the monolithic quartz design is approximately 1.25 dB; representing a power loss of 25%. Given the generally reduced performance, the BVP suggests a sandwich S2-glass/epoxy design is far superior over a similarly sized quartz panel for an UWB application.

A similar comparison was made for the monolithic S2-glass/epoxy design. The peak difference between the monolithic and sandwich S2-glass/epoxy designs occurs around 11 GHz where the sandwich

design shows a performance approximately 2.5 dB greater than the monolithic design. A 2.5 dB reduction in power is equivalent to 56% of the transmitted signal. Based on these results, if the electrical performance is the main driving factor for the design, the sandwich design is clearly the superior design across the majority of the band.

It should be noted that the transmissivity only accounts for one way loss. Thus for monostatic radar applications, similar to systems CReSIS has employed in the past, the losses would actually be double what is presented in Figure 4.2. The loss would occur once for the transmit signal and again for the return signal. This would mean the monolithic glass design would have a signal attenuation of -5 dB around 11 GHz, while the quartz and sandwich panels would have attenuations of -2.5 dB and -0.25 dB, respectively, at the same frequency.

The results in Figure 4.2 also show support for the fact that it is very difficult to design radomes for UWB applications. As mentioned in Chapter 1, radomes are generally designed for narrow frequency bands as the transmissivity of the panel eventually reduces. In this sense, the radomes are acting as a physical filter. Thus it is important to note that any conclusions regarding UWB performance for the radomes designs is limited to the microwave band of 2 – 18 GHz. In particular, if the designs were compared at lower frequencies the results may show the performance of two designs are similar enough the design may be selected based on structural performance or cost rather than electrical performance.

4.3 Anechoic Chamber Measurements

For anechoic chamber testing, two A-info horn antennas [Refs. 24 and 25] were setup 37 inches apart so that the antennas were operating in each other's far field. Each of the test panels were placed 1" away from the transmitting antenna. This setup can be seen in Figures 4.3 and 4.4. The panels were spaced 1" from the transmitting antenna due to the size of the panels; placing the panels further from the transmitting antenna caused the results to show more interference possibly due to the signal leaking around the panels or diffractions caused by the edge of the panels.

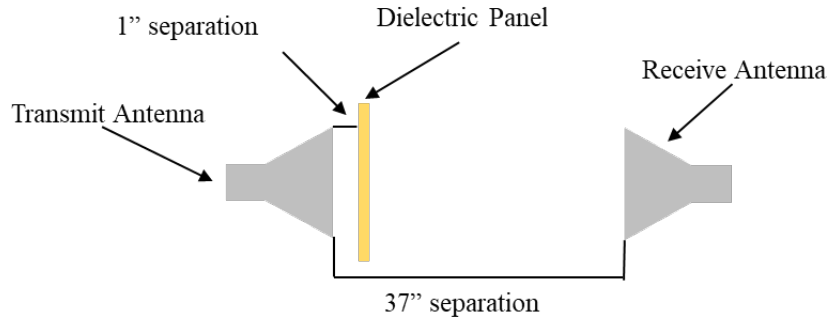


Figure 4.3: Infographic of the Anechoic Chamber Setup



Figure 4.4: Anechoic Chamber Setup

During testing five measurements were taken including the free space response (when there was no panel between the two antennas) and then a measurement with each of the four panels. While the S2-glass/epoxy and quartz materials have orthographic properties, the BVP analysis treats each material as isotropic. Since both materials are dielectric, this assumption is reasonable. The 0/90 S2-glass/epoxy design was tested along with the other three designs to determine if the fiber orientation has any effect on the transmissivity. The S-parameters measured represent the transmitted power (S_{12}) between the two antennas as well as the reflected power (S_{11}). Figure 4.5 shows the S_{12} time domain response for each of the panels, and Figure 4.6 is a zoomed in view of the peaks. In these plots the index values on the x-axis are representative of the time delay for the signal to travel from the transmit antenna to the receive antenna. As expected the free space curve shows the highest transmitted power (S_{12} (dB)) because there is nothing impeding the signal between the two antennas. The time delay observed in the panel measurements is due to the signal traveling at a slower velocity through the dielectric medium. Once again, the sandwich panel had the lowest loss out of the four panel solutions.

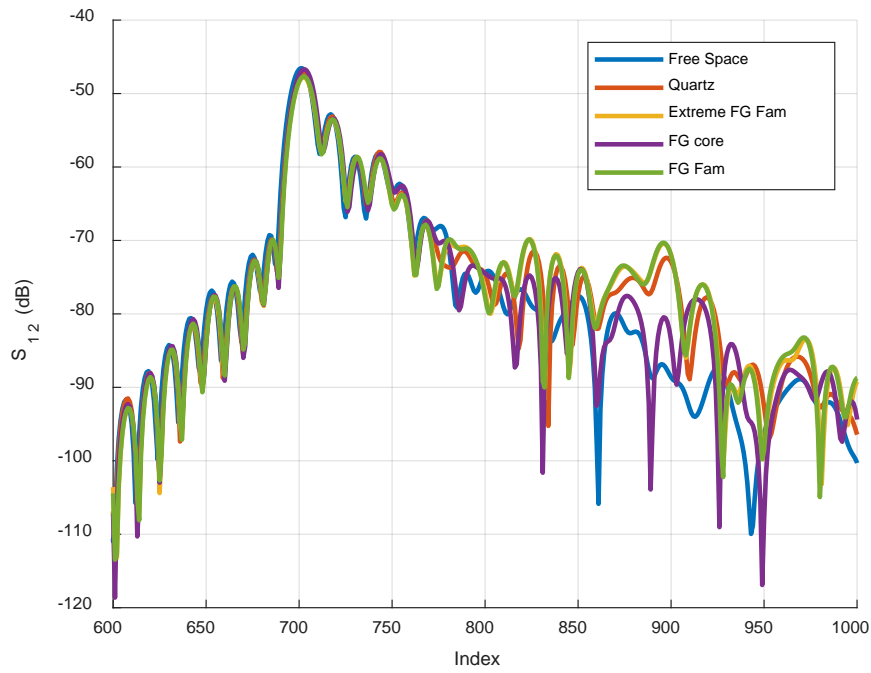


Figure 4.5: Time Domain Response

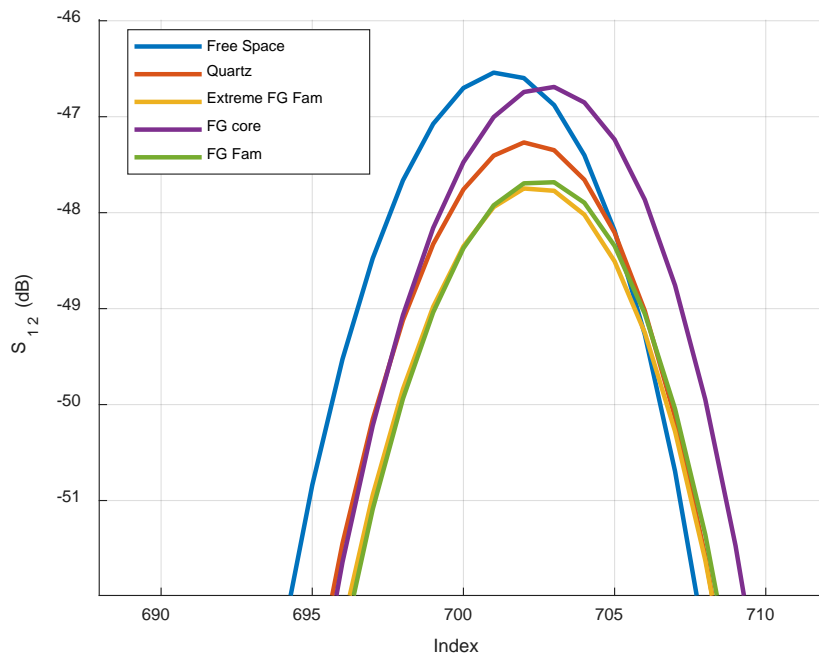


Figure 4.6: Peak S_{12} Response of the Test Results in the Time Domain

To extract the transmissivity of the panel, the difference was found between the free space data and the test data for each panel. The free space measurement was used as a baseline to remove reflections in the

system that could not be calibrated out (i.e. the antenna response as well as reflections bouncing off the receiving antennas) as well as the spherical spreading losses. To further isolate the actual signal a time gate and Hanning window were also used. The S_{12} resulting transmissivity of the panels are shown in Figure 4.7.

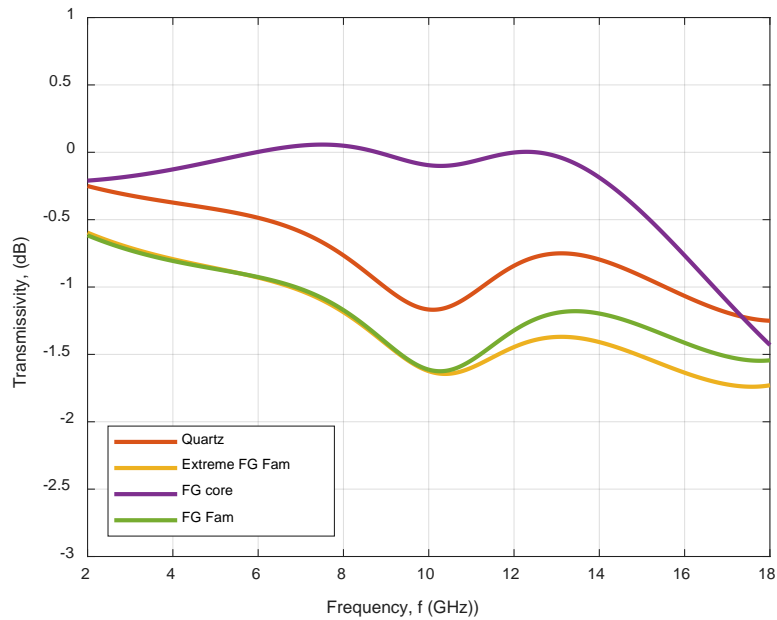


Figure 4.7: Measured Transmitted Power

The results presented for anechoic chamber testing shows that the BVP analysis provided a close approximation to the actual response of each panel. Based on Figure 4.7 the results for the sandwich panel (FG core) were higher than the BVP results, and from 6 – 8 GHz the response was over 0 dB which means the system transmitted over 100% of the available power; however the shape of the curve was the same as the BVP results for the sandwich panel with the inflection points occurring at almost identical frequencies. The transmissivity above 0 dB would indicate that more power was received by the receiving antenna than that for the free space measurement. In general this does not make sense. The increase (and similarly other deviations between the measurements in Figure 4.7 and the BVP solution) can be attributed, in part, to edge diffractions of the panel. This was confirmed by performing measurements with a sheet of metallic backed

foam with a small window cut in it. Though the metal – backing should have reflected most of the signal, due to diffraction at the edges of the cutout, there was an increase in S_{12} over the free space measurements.

The same conclusion can be made for the other three panels because the transmitted power levels were also higher than what the BVP produced. However, the BVP provided a good approximation as can be seen from the response of the sandwich design, which only showed a 0.25 dB deviation between the BVP and the results of anechoic chamber testing. The responses for the monolithic designs showed the same response at 2 and 18 GHz however, these panels showed deviations across the span, especially around 8 – 12 GHz. The BVP was still considered a good approximation for the monolithic designs because the largest deviation is only 0.7 dB. Also, the improvement of the monolithic quartz over the monolithic S2-glass/epoxy was found to be smaller during testing than the results of the BVP analysis. The BVP suggests the monolithic quartz design should show a 1 dB improvement over the monolithic S2-glass/epoxy; however, Figure 4.7 would suggest this improvement is closer to 0.5 dB for one way transmission. These results could also be a function of the signals diffraction at the edges of the panels providing a higher transmission than what was expected.

Figure 4.7 also shows that in general the solutions of the two monolithic S2-glass/epoxy panels are identical and have a maximum deviation of 0.25 dB at 18 GHz. Again, this could have been caused leakage or signal diffraction at the edges (especially since the panels were manufactured by hand), creating a better response for the [25/50/25] family, or it could have been caused by depolarization of the wave. However, in general the two panels were identical, thus it would seem that the BVP provides a good approximation of the transmissivity for potential radome designs.

Despite these differences, the good agreement between the BVP results and the measurements suggest that the BVP can provide a good estimate of the electrical response of structurally sized panels. Chapter 5 will discuss the results of using the BVP to determine the transmission of the panels sized in Chapter 3.

5. EM Analysis of Alternate Radome Panel Designs

Despite the simplicity of the BVP solutions, the results discussed in Chapter 4 suggests this approach provides a good estimate for the preliminary electrical analysis of radome structures. This chapter presents the results of the BVP analysis for the dielectric ventilation panels and MCoRDS radome panels sized in Chapter 3. Section 5.1 presents the results for the BVP analysis of the dielectric ventilation panels, and Section 5.2 presents the results for the BVP analysis of the MCoRDS radome panels

5.1 EM Analysis of the Dielectric Vent Panel Designs

As discussed in Chapter 3, there were five different designs for the dielectric vent panel, including the original wet layup glass design. For this analysis only the laminate design in the recessed region of the panel was analyzed because this is the region of the ventilation panel that the signal must propagate through. The designs included 12 layers of wet layup S2-glass/epoxy, 12 layers of pre-preg S2-glass/epoxy, 12 layers of quartz based on the conservative mechanical properties, eight layers of quartz sized with the manufacturer's ideal properties, and a sandwich laminate with a [0,45,core,45,0] layup. Table 5.1 provides the cured ply thickness of each material, while Figure 5.1 shows the electrical response for each of the dielectric vent panels sized in Chapter 3.

Table 5.1: Ply Thicknesses for Structurally Sized Dielectric Ventilation Panels

Material	CPT (inches)
Wet Layup S2-glass/epoxy [Ref. 24, 25]	0.009
Pre-Preg S2-glass/epoxy [Ref. 22]	0.0101
Tested Quartz	0.0114
Reported Quartz [Ref. 20 and 21]	0.0105

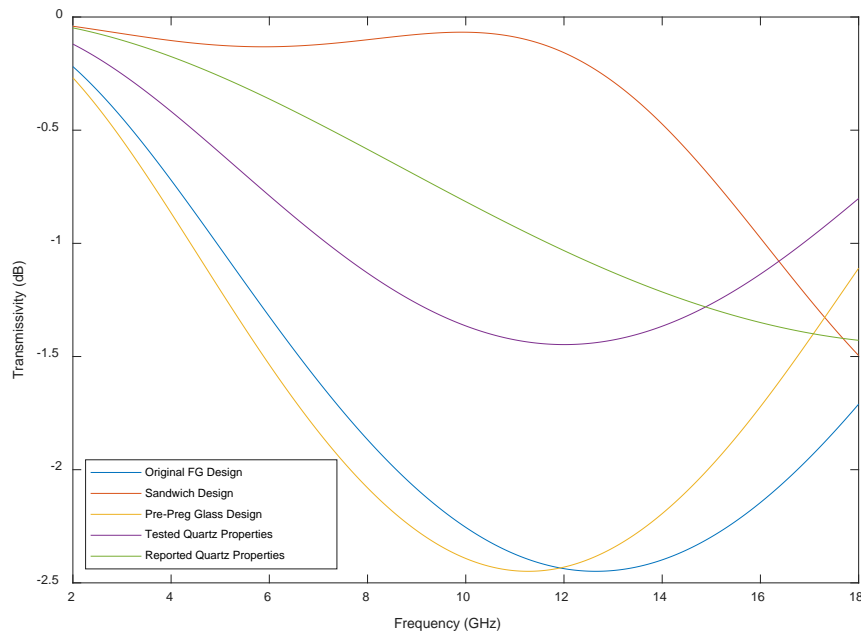


Figure 5.1: BVP Analysis for Dielectric Ventilation Panel Designs

Similar to both the BVP and measured results in Chapter 4, the sandwich panel with 0.25” Rohacell 71 WF core still provided the most favorable electrical response for the majority of the frequency band, providing exceptional returns for 2 – 12 GHz. In Figure 5.1, the two monolithic S2-glass panels, both the wet layup and pre-preg designs, provided roughly the same transmitted power levels; only deviating by approximately 0.2 dB while operating below 14 GHz. The only difference in the BVP analysis of the two S2-glass designs was the ply thickness. When the performance of the monolithic S2-glass designs started to improve above 12 GHz, the pre-preg transmissivity improved at a faster rate resulting in an improvement in the transmitted power of approximately 0.5 dB, at 18 GHz. Both designs provided the lowest transmitted power levels of all the designs and the results shown in Figure 5.1 would suggest monolithic S2-glass designs are only more favorable at either 2 or 18 GHz.

The two quartz designs created better response than the monolithic S2-glass designs. Given the reduced thickness of the quartz design based on the manufacturer’s properties, this panel had a slightly better performance, achieving a maximum increase in the transmitted power level over the tested properties design by 0.5 dB at a frequency within 10 – 11 GHz. This is an improvement of 12% in the transmitted

power between the two quartz designs. These two quartz designs also showed improvement over the monolithic S2-glass designs. The quartz panel sized with the manufacturer's properties showed an average improvement of approximately 0.9 dB across the frequency band, while the tested quartz properties showed an average improvement of approximately 0.83 dB. Since the two quartz designs were created to provide bounds for the capabilities of the material, it is likely that a panel made of quartz would have a transmissivity between these bounds showing favorability of a quartz monolithic design over a S2-glass monolithic design.

These results conclude that based on the electrical performance of the dielectric ventilation panels, the sandwich design is the most favorable given the near unity transmissivity for the majority of the frequency span. While this design demonstrated good transmissivity, Figure 5.1 also illustrates the difficulty of designing an UWB radome. The sandwich S2-glass design only provided a good response, above -0.5 dB, for 2 – 14 GHz, while above 14 GHz it could be advisable to use one of the monolithic quartz designs.

Given the performance of the S2-glass sandwich design, the transmissivity of a quartz sandwich was also investigated. Figure 5.2 includes a sandwich panel composed of Rohacell 71-WF core and quartz material. The BVP analysis for this quartz sandwich was based on the same laminate design as the S2-glass sandwich and the design was not evaluated through structural analysis. This panel was considered based on the conclusions made in Chapter 4 stating that the BVP can provide a good preliminary analysis of the electrical performance.

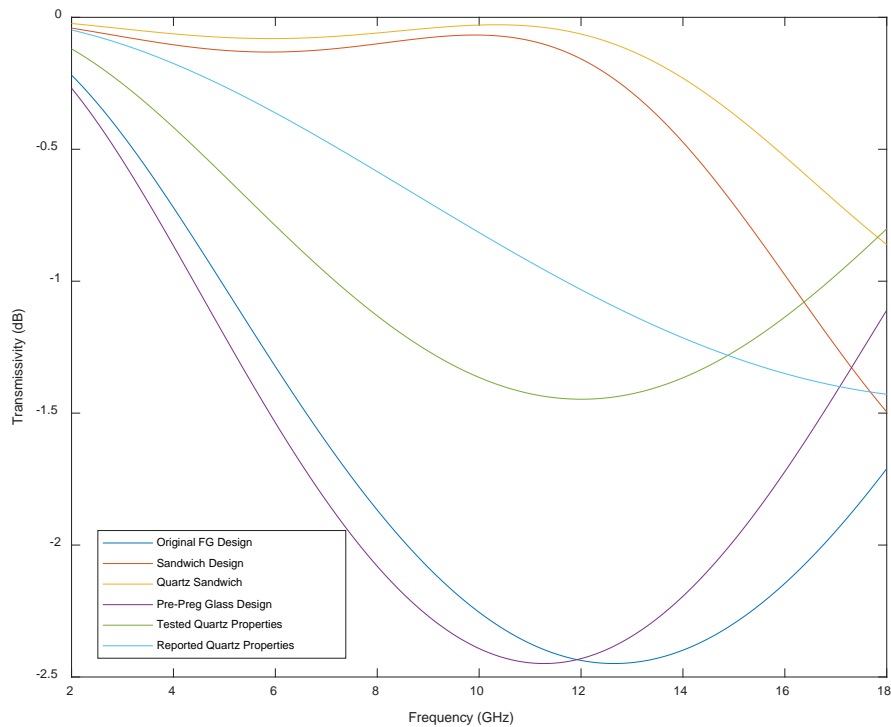


Figure 5.2: BVP Analysis including a Sandwich Quartz Design

The sandwich quartz design only shows slight improvement from the S2-glass sandwich design from 2 – 12 GHz, but the transmissivity improves by about 0.7 dB at 18 GHz. Given the modest improvement in the electrical performance of the quartz sandwich over the S2-glass sandwich designs for the majority of the frequency band, and the increased cost of the quartz material [Ref. 1], the sandwich S2-glass design is likely the most favorable in most instances.

5.2 EM Analysis for the MCoRDS Radome Panels

Figure 5.3 shows the transmissivity for the thicker MCoRDS panel for 2 – 18 GHz. Recall that the designs shown in Figure 5.3 were sandwich designs with 24 plies of material and Rohacell 71-WF core. It is clear from this plot that the thicker radomes had improved performance over much narrower bands; however, the maximum losses were comparable to that of the thinner vent cover.

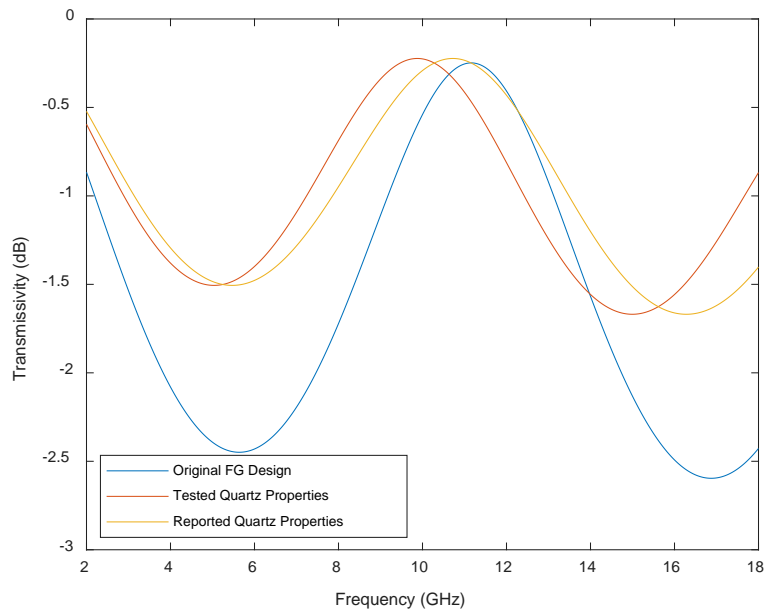


Figure 5.3: BVP Results for the MCoRDS Sandwich Radomes

Once again the UWB performance of the two quartz designs is better than the glass design with the exception of a small frequency range between 11 – 14 GHz where the transmissivity was within 0.5 dB. The main difference between the quartz designs, most likely driven by the thickness, is a shifted frequency response. However, these two designs produced essentially the same results across the frequency span only deviating by 0.5 dB at 18 GHz.

Once again, these BVP results for the MCoRDS radome designs suggest the quartz material will result in a potential improvement in the transmissivity of about 1 dB. The maximum losses of the MCoRDS quartz sandwich were comparable to the monolithic quartz solution for the dielectric ventilation panel. However, both MCoRDS sandwich designs had transmissivities more suited for narrow band operations. When comparing the thinner sandwich designs of Figure 5.1 to the thicker sandwich designs in Figure 5.3, it is clear that overall losses are higher and the thicker panel has only had a small frequency band between 8-12 GHz where the estimated losses were less than 1 dB.

6. Conclusions and Recommendations

6.1 Conclusions

The preceding work provided a robust comparison of the predicted electrical performance of several dielectric panel designs while also balancing structural requirements. While the designs involving the quartz material could only provide bounds on the expected performance, the following are conclusions derived from this work:

1. The results of the mechanical testing in Chapter 2 showed multiple modes of failure including significant delamination. The delamination was assumed to be caused by the expiration of the resin system; since the resin was expired it was dry and was unable to flow thus leaving dry fibers in the laminate. Given this, the mechanical properties found through material testing in Chapter 2 were much lower than the in-date material, and thus there is high confidence they are very conservative.
2. The electrical testing performed for this analysis demonstrates the validity of using the BVP method for preliminary analysis for radome designs. This was proven by the similarities between the BVP method and anechoic chamber test results. The anechoic chamber testing showed the sandwich panel provided an average 0.75 dB improvement over the quartz design across the frequency span, whereas the BVP showed a 1 dB improvement. Also the anechoic chamber testing verified that the electrical response in the presence of the dielectric radome structure is relatively insensitive to the fiber orientation within the laminate; as fiber orientation is not taken into account in the BVP analysis. This is why the 25/50/25 and the 0/90 fiberglass laminates produced virtually the same results in the anechoic chamber testing, with only a 0.25 dB deviation at 18GHz. Differences between the BVP solution and chamber measurements are likely a result of leakage around the panel and edge diffraction. The BVP formulation assumes an infinitely large planar surface, whereas the test panels were only slightly larger than the footprint of the horn aperture, which was assumed to be the cause of the leakage and edge diffraction. This was most pronounced in the testing of the sandwich S2-glass/epoxy panel which produced a transmissivity above unity. Edge

diffraction or leakage was also present in the responses of the other three panels, resulting in the 0.25 dB deviation between the two monolithic S2-glass/epoxy designs, and the 0.5 dB difference between the monolithic S2-glass/epoxy and quartz designs instead of the expected 1dB from the BVP analysis. It should also be noted that the BVP assumes the panel is in the far-field of the antenna, and thus the waves impinging on it are planar. The panels in the test setup were placed in the near field, and this is likely another source of discrepancy.

3. The results from Chapter 5 showed that there is a limit to how well a sandwich design will perform, as the thicker MCoRDS radomes only performed well over the 8 – 12 GHz range (Ku-band). The sizing of the MCoRDS radomes showed a thicker laminate was better suited for narrow band applications; for this instance in the Ku-band. In the case of the 2 – 18 GHz horn antenna, the thinner laminate designs of the dielectric ventilation panels were the best designs for UWB applications. Based on the sizing of the dielectric ventilation panel, the sandwich solution was the most applicable to an UWB application, as was seen with the transmissivity near unity for the frequency band 2 – 12 GHz. For a 2 – 18 GHz application, these results suggest it would be better to design a smaller footprint thinner sandwich structure that is bound by stiffeners than to design a thicker sandwich without stiffeners.
4. Ultimately, the electrical analysis illustrated that a sandwich S2-glass/epoxy design demonstrated better electrical performance than a monolithic quartz design, and certainly better than a monolithic S2-glass/epoxy design. Also, although the sandwich quartz design showed modest improvements over the S2-glass/epoxy sandwich design, given the significantly higher cost for the quartz, the S2-glass/epoxy sandwich design is recommended for 2 – 18 GHz radomes. More specifically a sandwich made from four layers of S2-glass/epoxy and core is recommended for the 2 – 18 GHz band, when the application loads allow this to be feasible.

6.2 Recommendations and Future Work

The following are recommendations for continuation of the research presented in this document:

1. The material testing discussed in Chapter 2, while conservative, provided a lower bound for the mechanical properties of the quartz material. However, it would be imperative to conduct a robust testing program of in-date material for any future applications of this material. Also, the testing in Chapter 2 was performed for un-notched coupons, with the following fiber orientations and families: 0° , 45° , and 25/50/25. Any future testing should also include 30/40/30 and 20/60/20 families to provide a more complete analysis as not all structures are designed with 25/50/25 families; and testing should be performed to determine the open-hole allowables so the un-notched properties do not have to be scaled.
2. For the anechoic chamber results presented in Chapter 4, the system generated a response above 0 dB, representing that the signal received was stronger than the signal transmitted. This was assumed to be a function of the edge diffraction due to the panel sizes. The panels used for anechoic chamber testing were built relatively small to preserve material; the monolithic glass panels were made 8" by 8"; the monolithic quartz panel was made 5.5" by 7.5"; and the core in the sandwich panel was 8" by 8". As a result of the panels being so small, the transmitted signal was able to leak around the edges of the panels and into the receive antenna. The signal also diffracted at the edges of the panels producing a higher receive signal than what was transmitted. The anechoic chamber testing should be repeated with larger panels to mitigate these effects.
3. For a structural design such as the dielectric ventilation panel, a sandwich structure may not be advisable due to the small footprint of the design. The dielectric ventilation panel design required fasteners around the perimeter of the panel, thus a sandwich design would require a taper to a monolithic laminate in the region of the fasteners. In this particular instance the core taper would have been with the footprint of the antenna aperture. It is recommended to conduct electrical testing to examine the effect of a taper if the tapered region of the core is in the illuminated region of the radome panel.

7. References

1. E.J. Arnold, "Personal Communication," 2020.
2. E.J. Arnold, C. Leuschen, F. Rodriguez-Morales, J. Li, R. Hale, S. Keshmiri, "CReSIS Airborne Radars and Platforms for Ice and Snow Sounding," *Annals of Glaciology*, No. 81, 2019, pp 1–10. <https://doi.org/10.1017/aog.2019.37>
3. F. Rodriguez-Morales, P. Gogineni, C. Leuschen, J. Paden, J. Li, C. Lewis, B. Panzer, D. Gomez-Garcia, A. Patel, K. Byers, R. Crowe, K. Player, R. Hale, E. Arnold, L. Smith, C. Gifford, D. Braaten, and C. Panton, "An Advanced Multi-Frequency Radar Instrumentation Suite for Polar Research," *IEEE Transactions on Geoscience and Remote Sensing*, Vol. 52, No. 5, May 2014.
4. A. Escalera Mendoza, "Effects of Radome Design on Antenna Performance in Transonic Flight Conditions," *AIAA SciTech*. 2020.
5. R. Hale, E. Arnold, M. Ewing, and W. Lui, "Method for Design and Analysis of Externally Mounted Antenna Fairings in Support of Cryospheric Surveying," *AIAA Structures, Structural Dynamics and Materials Conference*, Denver, CO, April 2011.
6. E. Arnold, "Development and Improvement of Airborne Remote Sensing Radar Platforms," Ph.D. Dissertation, University of Kansas, Department of Aerospace Engineering, June 2013.
7. W.A. Anemaat, W. Liu, B. Kaushik, M. Yang, M. Brown, R. Hale, "Design, Build and Fly: NASA Lockheed P3 Orion with External Antenna Fairings", AIAA-2013-0019, presented at the 51st AIAA Aerospace Sciences Meeting, January 7-10, 2013, Grapevine, Texas.
8. Rodriguez-Morales F, Leuschen C, Carabajal C, Wolf A and Garrison S, "Measurements of snow cover using an improved UWB 2–18 GHz airborne radar testbed," 2018 IEEE Radar Conference, Oklahoma City, OK. doi: 10.1109/RADAR.2018.8378703.
9. Rodriguez-Morales F, "An improved UWB microwave radar for very long-range measurements of snow cover," *IEEE Transactions on Instrumentation and Measurement*. 2019.
10. R. Shavit, "Radome Electromagnetic Theory and Design," John Wiley & Sons, April 2018.

11. R.B. Curtis, "Survey of Ground Radomes," Rome Air Development Center, Air Force Systems Command, United States Air Force, 1961.
12. A Piche, et al. "Prediction by Simulation of Electromagnetic Impact of Radome on Typical Aircraft Antenna," The 8th European Conference on Antennas and Propagation (EuCAP 2014), 2014.
13. K.R. Demarest, "Engineering Electromagnetics", 1st ed. Prentice Hall, Upper Saddle River, NJ. 1997.
14. D.J. Kozakoff, "Analysis of Radome-Enclosed Antennas," Artech House. Second Edition. 2010
15. Y. Zhao, J.Fu, et al, "A Novel Ultra-Wideband Switch-Type Active Frequency Selective Surface for Radome Applications," 13th European Conference on Antennas and Propagation (EuCAP 2019), 2019.
16. Y. Feng, Y. Hu, J. Jiang, D. Cheng, D. Li, "Design and Analysis of Wave Transmission Performance of Centimeter Band Ultra-Wideband Missile Radome," IEEE Advanced Information Technology, Electronic Automation Control Conference (IAEAC), 2019.
17. R.U. Nair, and R.M. Jha, "EM Performance Analysis of an A-sandwich Cone-Ogive Hybrid Variable Thickness Radome," Computational Electromagnetic Lab. IEEE. 2004.
18. ASTM. "Standard Test Method for Tensile Properties of Polymer Matrix Composite Material." ASTM Standard D3039/D3039M. American Society for Testing and Materials. 2017.
19. ASTM. "Standard Test Method for In-Plane Shear Response of Polymer Matrix Composite Materials by Tensile Test of a +/- 45° Laminate. ASTM Standard D3518/D3518M. American Society for Testing and Materials. 2018.
20. Anonymous. "BTCy-1A Product Data Sheet." Tencate Advance Composites.
21. Anonymous. Tencate Advance Composites. "Test Level Data."
22. National Institute for Aviation Research, Advanced Composites Group. "ACG MTM45-1 6781 S-2 glass 35% RC Qualification Material Property Data Report." CAM-RP-2009-001 REV C 1 May 2013

23. SACMA. "SACMA Recommended Test Method for Compressive Properties of Oriented Fiber-Resin Composites." SACMA Standard SRM 1R-94. Suppliers of Advanced Composite Materials Association. 1994
24. R. Hale. et. al. "Structural Analysis of the Snow Horn Antenna Assembly for the NASA GV." University of Kansas. October 2019.
25. R. Hale, et. al. "Structural Analysis of the MCoRDS and Snow Horn Antenna Assembly for the NASA GV." University of Kansas. October 2019.
26. Anon., "NSF/NCAR Gulfstream V Investigator's Handbook," National Center for Atmospheric Research, Boulder, CO, January 2016.
27. R. Hale. et al. "Structural Analysis of the MCoRDS Antenna Assembly," The University of Kansas, August 2009.
28. MMPDS-10, "Metallic Materials Properties Development and Standardization (MMPDS)," Federal Aviation Administration, Battelle Memorial Institute, 2015.
29. Anon., "Rohacell WF Product Information," Rohacell, [<https://www.rohacell.com/product/peek-industrial/downloads/rohacell%20wf%20product%20information.pdf>], February 2018.

Appendix A. MTS Calibration Testing

Due to the expired calibration of the force transducer installed on the test stand used for the tensile tests, a series of tests were performed to verify the system was calibrated. Calibration tests were performed by collecting data to determine the Young's Modulus of the material being tested. Calibration was performed with a 5052-H32 aluminum coupon. To perform the calibration tests the yield strength of the 5052-H32 aluminum could not be exceeded, because the coupon had to be loaded multiple times. During testing a limit load had to be programmed into the test stand to ensure it would not exceed the yield load.

The dimensions and mechanical properties of the 5052-H32 aluminum coupon are presented in Tables A.1 and A.2, respectively. Based on the cross sectional area and yield strength, the yield load was determine to be 5,676 pounds. Since the objective was to determine the Young's modulus, the final loading only needed to be able to produce large enough portion of the stress – strain curve to calculate the modulus, E; therefore, the limit load of the test stand was set to 3,000 lbs. The Young's modulus found during testing was then compared to the reported Young's modulus value from Military Handbook 5H [Ref. 26]. Any deviation was considered an error in the test stand.

Table A.1: Dimensions for 5052 Aluminum Calibration Coupon

Dimension (Units)	Value
Length (in.)	12.1
Width (in.)	0.987
Thickness (in.)	0.25
Area (in ²)	0.2468

Table A.2: Properties of 5052 Aluminum [Ref. 26]

Properties (Units)	Value
F _{tu} (ksi)	31
F _{ty} (ksi)	23
F _{cy} (ksi)	22
F _{su} (ksi)	19
E (msi)	10.1
E _c (msi)	10.2
G (msi)	3.85

The aluminum coupon was equipped with three longitudinal strain gages; two gages on one face, and one gage on the other face, as seen in Figure A.1. Using this three strain gage setup allows for observation of bending in two axis or twisting of the coupon.

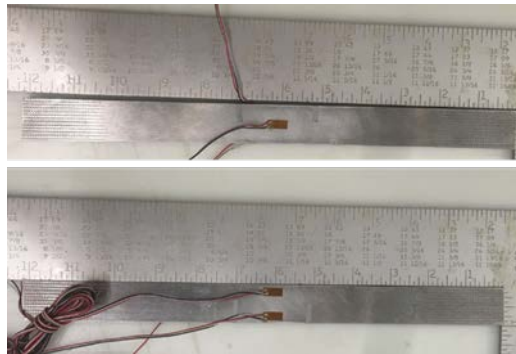


Figure A.1: 5052-H32 Aluminum Calibration Coupon

Four tests were run to calibrate the system. Tests 1, 2, and 4 were set-up with similar orientations for the coupon, and test 3 was set-up with the coupon rotated 180° from the other tests. These calibration tests were utilized to determine an appropriate setup procedure for testing as well as determining the calibration of the system. For test 1, the coupon was aligned in the test stand using an analog square. After test 1, this alignment method was considered inaccurate and the coupons were aligned using an electronic inclinometer for all future tensile tests.

Test 1 was also used to set the data collection rate for the output signal from the MTS stand so it would match the data rate programmed in the LabVIEW program. The data rate for test 1 was set at 8 Hz on the MTS operator's computer. The results for test 1 demonstrated the LabVIEW program was not

capable of this data rate. While the test stand operated at 8 Hz, the LabVIEW program recorded data at 2 Hz. To correct this, the data rate of the test stand was reduced to 2 Hz for all future tests.

Tests 2 and 3 were performed to calibrate the system following the test procedure outlined from the results of test 1. Then test 4 was performed to verify the results from test 2 by proving that the process was repeatable.

Table A.3 shows the results for calibration test 2. From Table A.3, E_1 and E_2 are the modulus values corresponding to the strain from the two strain gages on the same side of the coupon, and E_3 is the modulus value corresponding to the strain reading for the gage on the opposite side of the coupon. The upper and lower bound columns, shown in Table A.3, correspond to the position of the data point in a MATLAB table. For example, the third row in Table A.3 has a lower bound of 100 and an upper bound of 800. This means the stress and strain values located at (1, 100) and (1, 800) in the respective column vectors in MATLAB are the stress and strain values used to calculate the stiffness. For each test, 10 strain ranges were observed. The upper or lower bound was fixed, and the other was varied to find different stiffness values. Five data points were collected with the upper bound fixed, and five with the lower bound fixed. Then averages were found for the stiffness values calculated from each of the three strain gages.

Table A.3: Calibration Test #2 Results

Data points used		E ₁	E ₂	E ₃
Lower Bound	Upper Bound	ksi	ksi	ksi
100	800	1.00E+04	9.94E+03	9.63E+03
200	800	1.00E+04	9.91E+03	9.64E+03
250	800	1.00E+04	9.90E+03	9.63E+03
300	800	9.99E+03	9.90E+03	9.63E+03
400	800	9.97E+03	9.88E+03	9.64E+03
250	600	1.00E+04	9.89E+03	9.63E+03
250	700	1.00E+04	9.91E+03	9.63E+03
250	800	1.00E+04	9.90E+03	9.63E+03
250	900	9.99E+03	9.91E+03	9.64E+03
250	1000	9.97E+03	9.89E+03	9.65E+03
Averages		9.99E+03	9.90E+03	9.63E+03

Flexure can be seen in two directions. There is significant flexure in the longitudinal direction, as can be seen from the difference between E₃, and E₁ or E₃ and E₂. Flexure can also be seen in the lateral direction from the difference between E₁ and E₂. Also, this test stand is normally used for testing of structural steels, used in civil engineering, loaded up to 60,000 pounds. So it is possible that the test stand would appear to be calibrated properly at high loads and not the low loads used for this testing.

Figure A.2 shows the stress – strain curve for calibration test 2. This provides a further explanation for the selection of data points and the upper and lower bounds discussed for the two columns to the left of Table A.3. The asterisks shown on the plot represents the location of the data points used to calculate the moduli values for E₁, E₂, and E₃.

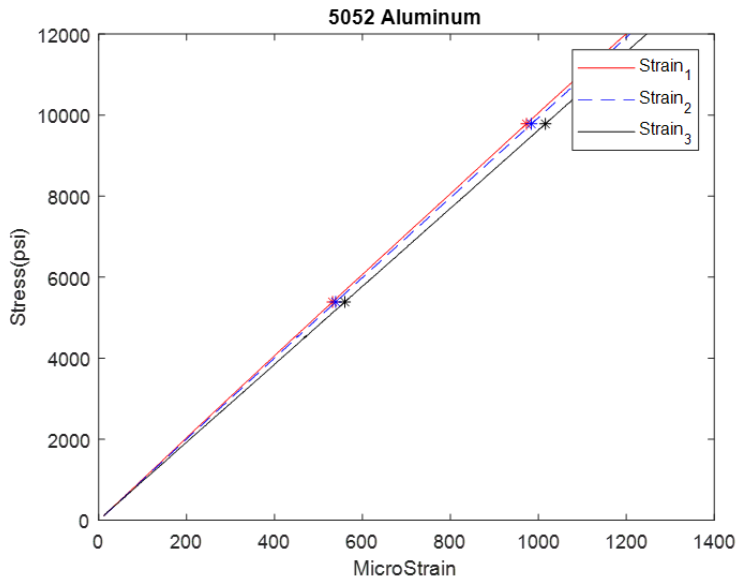


Figure A.2: Calibration Test #2 Results

As shown in Table A.4, the results for test 3 are reversed relative to the results for tests 2 and 4. This is because the coupon was rotated 180° in the test stand.

Table A.4: Average Results from each Calibration Test

Test #	E ₁ (Msi)	E ₂ (Msi)	E ₃ (Msi)
Test 2	9.99	9.90	9.63
Test 3	9.74	9.58	9.88
Test 4	9.92	9.80	9.73

The Young’s modulus values calculated for each test were lower than the expected 10.1 Msi reported in MIL-HDBK-5H. Table A.5 shows the overall average Young’s modulus calculated for the entire calibration test. This average was calculated by averaging all of the numbers included in Table A.4. Due to the operational errors in test 1, it was not included in the calculations to find the average results. The error shows the test results produced a modulus 2.99% lower than what was reported.

Table A.5: Final Results of Calibration Testing³

	Avg. Test Results E (Msi)	Reported E (Msi)	% error
Average for tests 2,3 and 4	9.80	10.1	2.99

For additional reference, the percent bending in both the y and z axes were also determined for each calibration tests to determine the amount of bending in each direction. Figure A.3 shows the percent bending for calibration test 2.

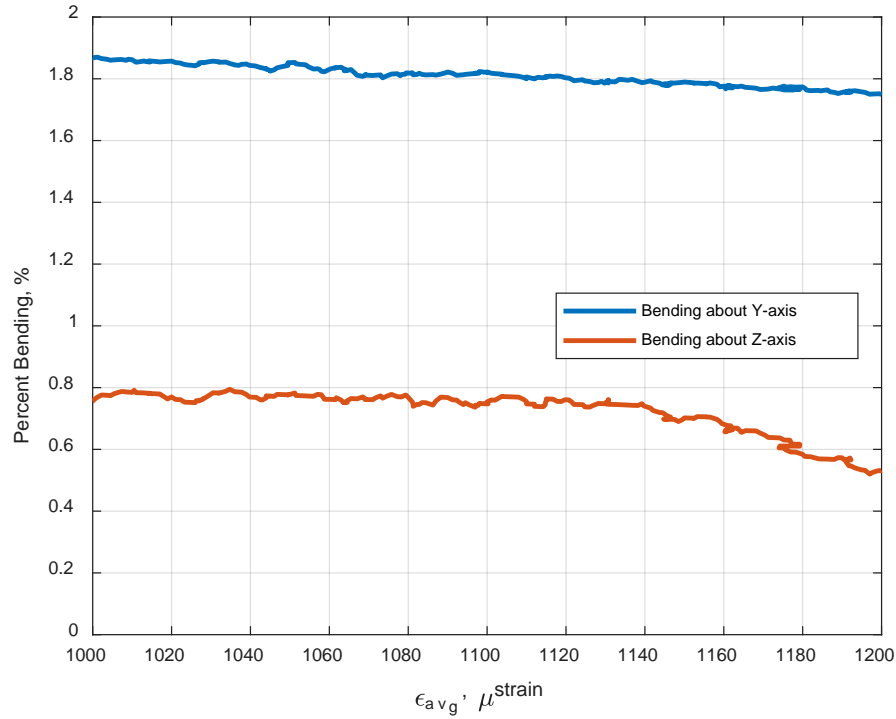


Figure A.3: Percent Bending in Calibration Test #2

Similar plots were created for calibration tests 3 and 4 as follows. Table A.6 includes the results for calibration test 3, while Table A.7 is the results for calibration test 4. Also included are the corresponding stress-strain plots for calibration tests 3 and 4 in Figures A.4 and A.6, respectively, with the corresponding percent error plots in Figures A.5 and A.7.

Table A.6: Calibration Test #3 Results

Data points used		E ₁	E ₂	E ₃
Lower Bound	Upper Bound	ksi	ksi	ksi
100	800	9.74E+03	9.60E+03	9.92E+03
200	800	9.75E+03	9.60E+03	9.91E+03
250	800	9.75E+03	9.58E+03	9.91E+03
300	800	9.74E+03	9.56E+03	9.88E+03
400	800	9.73E+03	9.54E+03	9.88E+03
250	600	9.75E+03	9.62E+03	9.90E+03
250	700	9.74E+03	9.62E+03	9.90E+03
250	800	9.75E+03	9.58E+03	9.91E+03
250	900	9.76E+03	9.56E+03	9.86E+03
250	1000	9.73E+03	9.51E+03	9.80E+03
Average		9.74E+03	9.58E+03	9.88E+03

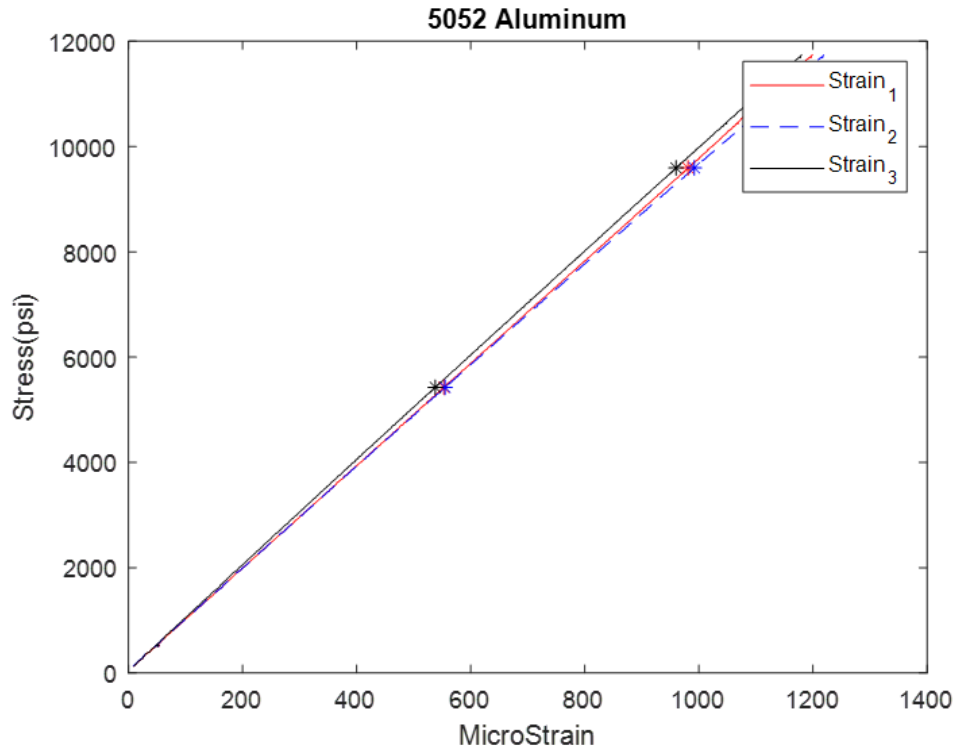


Figure A.4: Calibration Test #3 Results

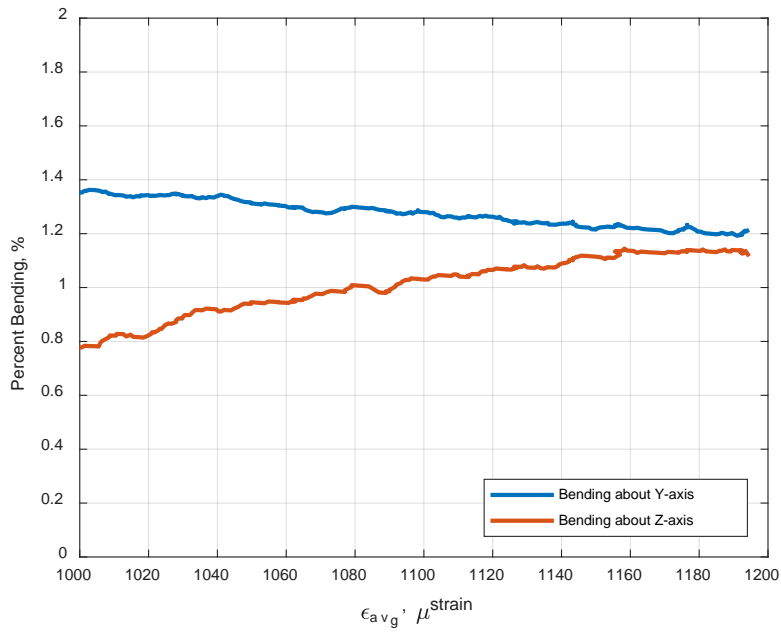


Figure A.5: Percent Bending in Calibration Test #3

Table A.7: Calibration Test #4 Results

Data points used		E ₁	E ₂	E ₃
Lower Bound	Upper Bound	ksi	ksi	ksi
100	800	9.99E+03	9.85E+03	9.74E+03
200	800	9.96E+03	9.84E+03	9.76E+03
250	800	9.94E+03	9.80E+03	9.74E+03
300	800	9.90E+03	9.79E+03	9.74E+03
400	800	9.89E+03	9.77E+03	9.72E+03
250	600	9.95E+03	9.79E+03	9.73E+03
250	700	9.91E+03	9.77E+03	9.72E+03
250	800	9.94E+03	9.80E+03	9.74E+03
250	900	9.90E+03	9.77E+03	9.72E+03
250	1000	9.87E+03	9.78E+03	9.71E+03
Average		9.92E+03	9.80E+03	9.73E+03

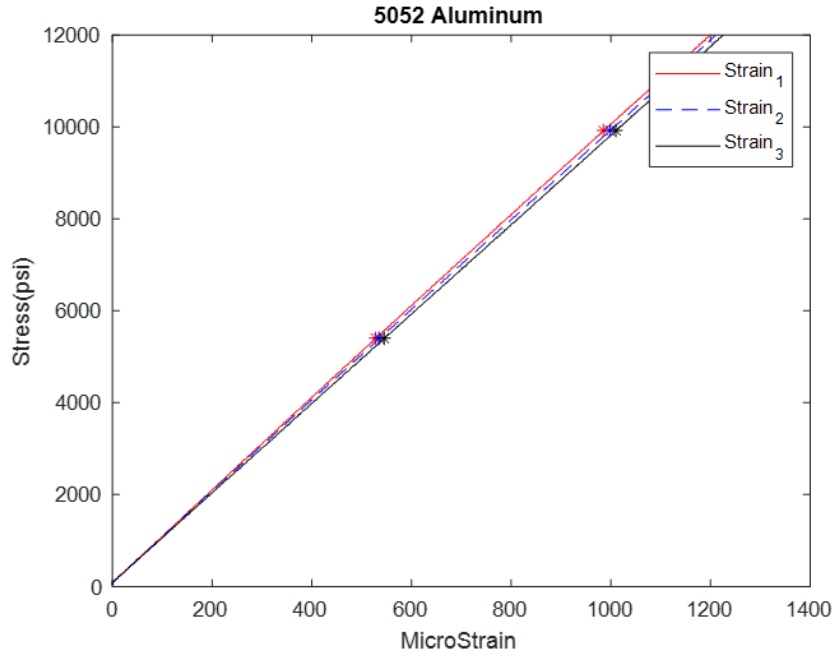


Figure A.6: Calibration Test #4 Results

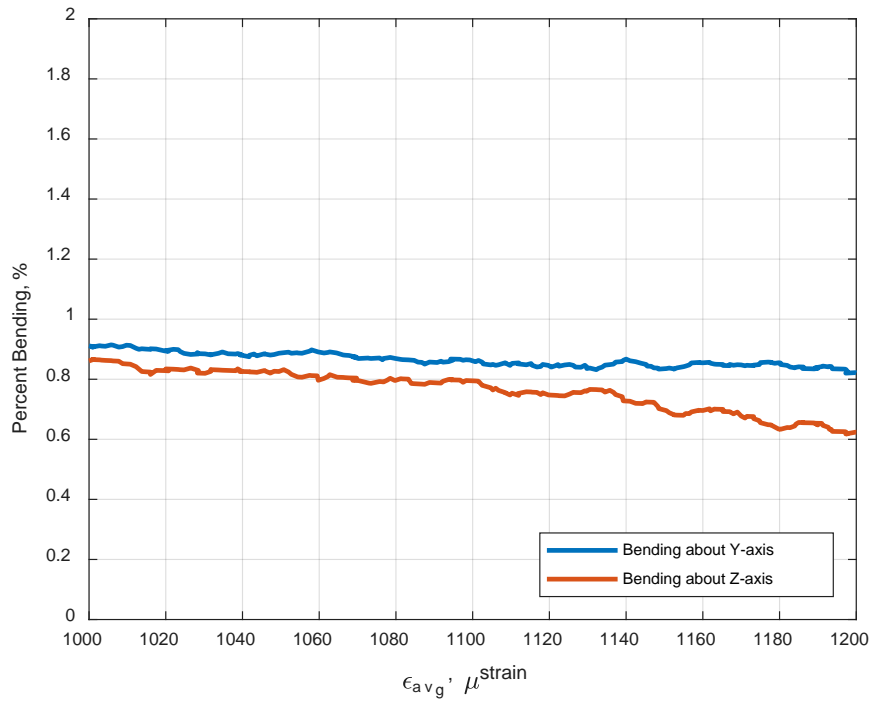


Figure A.7: Percent Bending in Calibration Test #4

Appendix B. Additional Results for 0° Testing

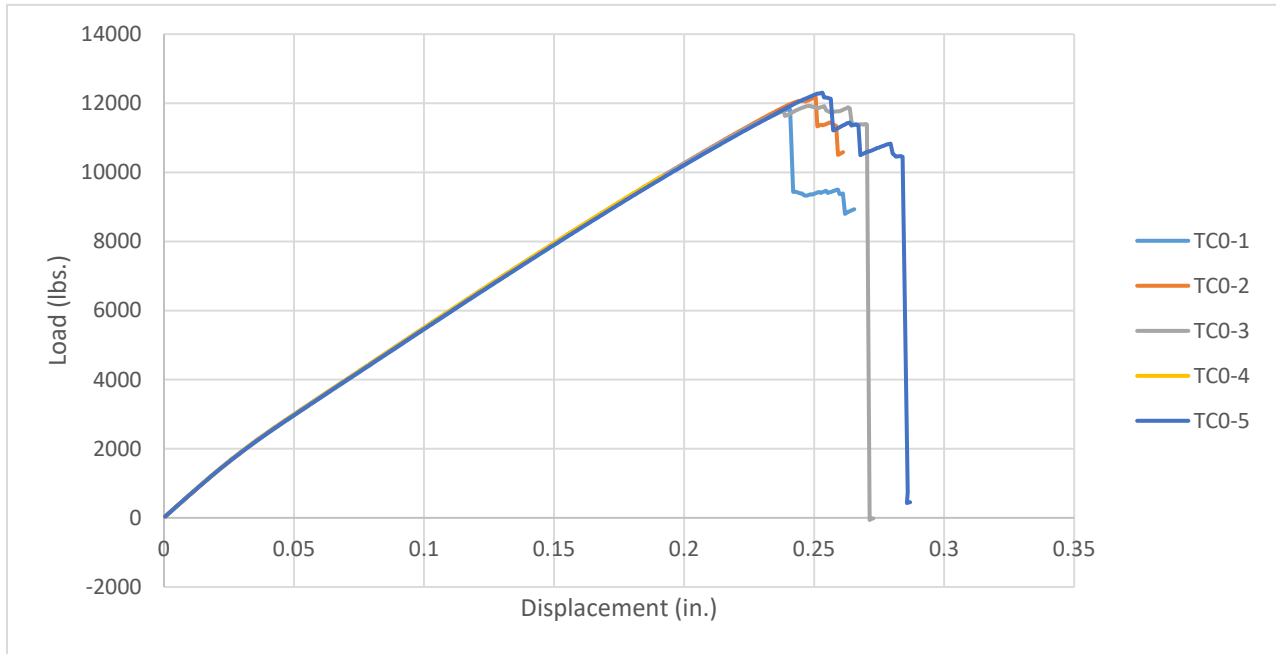


Figure B.1: Load versus Displacement curves for All 0° Coupons

Table B.1: Final Dimensions for 0° Coupons

Coupon I.D.	Length (in.)	Width (in.)	Thickness (in.)
TC0-1	9.950	1.009	0.143
TC0-2	9.950	1.010	0.142
TC0-3	9.960	1.018	0.140
TC0-4	9.960	1.014	0.141
TC0-5	9.950	1.011	0.143
Average	9.954	1.012	0.142

Table B.2: Final Load and Elongation of 0° Coupon Testing

Coupon I.D.	Actual Peak Load	Elongation at Peak Load	Failure Mode	Length of Test
	Pounds (Lbs.)	δL (in.)		HH:MM:SS
TC0-1	11824	0.24	X/MWT (1 st) X/SGM (2 nd)	0:03:22
TC0-2	12179	0.251	X/MAB	0:03:19
TC0-3	11921	0.249	SAB (1 st) X/MWT (2 nd)	0:03:28
TC0-4	12255	0.251	X/MGT	0:03:23
TC0-5	12307	0.253	X/MGT	0:03:38
Average	12097	0.249		0:03:26

Appendix C. Additional Results for 45° Testing

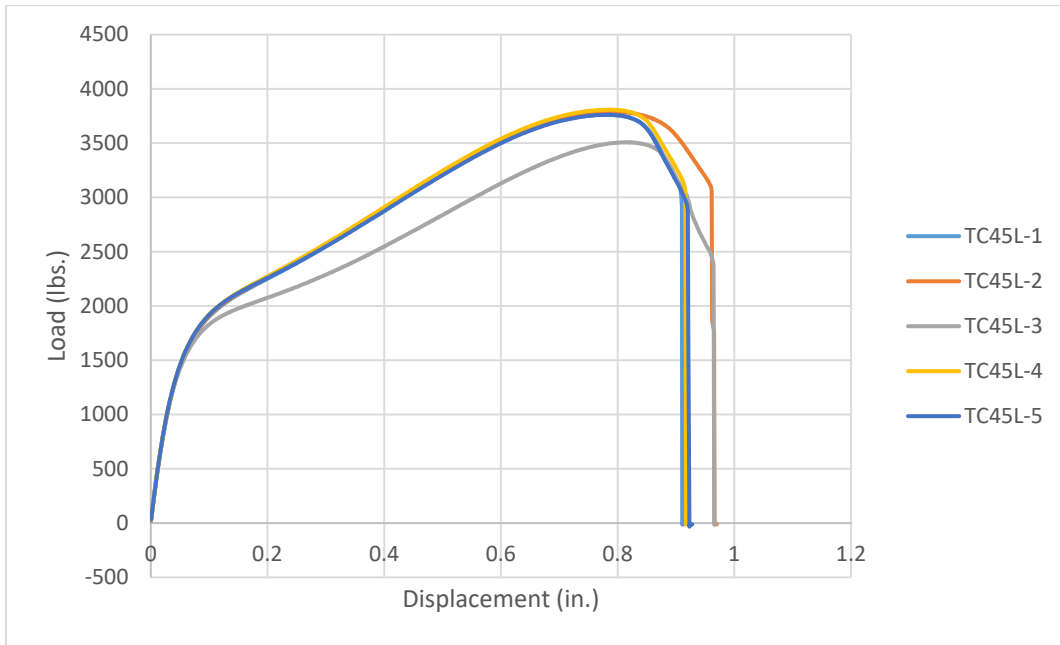


Figure C.1: Load versus Displacement Curves for All 45° Coupons

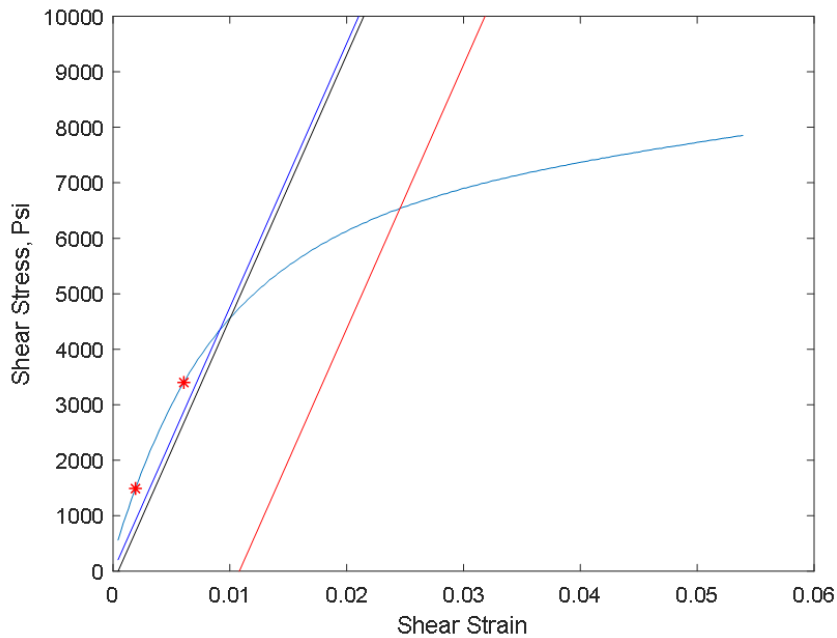


Figure C.2: Typical Plot for finding $F_{s0.2\%}$ and $F_{s5\%}$

Table C.1: Final Dimensions for 45° Coupons

Coupon I.D.	Length (in.)	Width (in.)	Thickness (in.)
TC45L-1	10.000	1.018	0.142
TC45L-2	10.000	1.014	0.140
TC45L-3	10.000	1.018	0.141
TC45L-4	10.000	1.018	0.141
TC45L-5	10.000	1.019	0.141
Average	10.000	1.017	0.141

Table C.2: Final Mode and Load for 45° Coupons

Coupon I.D.	Actual Failure Load	Elongation at Peak Load	Failure Mode	Test Rate	Length of Test
	Pounds (Lbs.)	δL (in.)		mm/min	HH:MM:SS
TC45L-1	3762.7	0.7762	X/LGT	2	0:11:39
TC45L-2	3790	0.7926	X/LGT	2	0:12:19
TC45L-3	3508	0.8153	X/AGT	2.5	0:09:50
TC45L-4	3808	0.7864	X/AGT	3	0:07:48
TC45L-5	3762	0.7883	X/AGT	3	0:07:51
Average	3726	0.7917			

Appendix D. Additional Results for 25/50/25 Testing

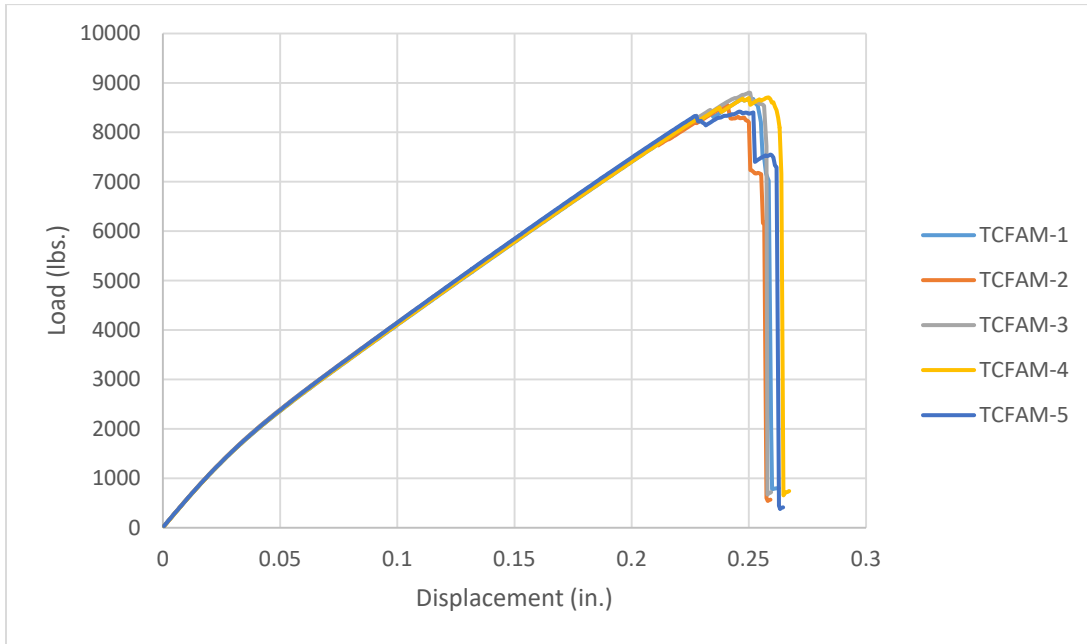


Figure D.1: Load versus Displacement Curve for All Family Coupons

Table D.1: Final Dimensions of 25/50/25 Coupons

Coupon I.D.	Length (in.)	Width (in.)	Thickness (in.)
TC-FAM-1	9.950	1.000	0.138
TC-FAM-2	9.950	1.019	0.137
TC-FAM-3	9.950	1.016	0.136
TC-FAM-4	9.960	1.013	0.138
TC-FAM-5	9.950	1.015	0.139
Average	9.952	1.013	0.137

Table D.2: Final Failure Modes and Loads for 25/50/25 Coupons

Coupon I.D.	Actual Failure Load	Elongation at Peak Load	Failure Mode	Length of Test
	Pounds (Lbs.)	δL (in.)		HH:MM:SS
TCFAM-1	8680	0.247	DGM	0:03:20
TCFAM-2	8557	0.241	DGM	0:03:17
TCFAM-3	8803	0.250	DGM	0:03:18
TCFAM-4	8706	0.259	DGM	0:03:23
TCFAM-5	8419	0.246	DGM	0:03:21
Average	8633	0.249		0:03:20

Appendix E. Additional Results for Compression Testing

Table E.1: Failure loads for Compressive Strength Tests

Coupon I.D.	Ply Orientation	Failure Load (lbs.)	Ultimate Strength (ksi)
CCS00-1	0	5018	70.15
CCS00-2	0	4878	68.33
CCS00-3	0	5179	72.9
CCS00-4	0	5167	72.1
CCS00-5	0	5109	71.56
Averages	0	5070.20	71.01
CCSFam-1	25/50/25	4197	61.84
CCSFam-2	25/50/25	4110	59.84
CCSFam-3	25/50/25	4259	62.75
CCSFam-4	25/50/25	4345	63.64
CCSFam-5	25/50/25	4201	61.29
Averages	25/50/25	4222.4	61.872

Table E.2: Loads for Calculating Compressive Modulus and Poisson's Ratio

Coupon I.D.	Ply Orientation	Young's Modulus (Msi)	Poisson's Ratio	P1(lbs.)	P3 (lbs.)
CCE00-1	0	3.44	0.12	348	835
CCE00-2	0	2.31	0.08	167	496
CCE00-3	0	3.28	-	331	800
CCE00-4	0	3.53	0.16	321	820
CCE00-5	0	3.8	0.15	405	937
Averages	0	3.513	0.143	351.250	848.000
CCEFam-1	25/50/25	-	-	-	-
CCEFam-2	25/50/25	2.87	0.28	291	679
CCEFam-3	25/50/25	2.76	0.25	491	865
CCEFam-4	25/50/25	2.81	0.27	378	762
CCEFam-5	25/50/25	3.05	0.28	409	821
Averages	25/50/25	2.873	0.270	392.250	781.750

Appendix F. Results for Tested Quartz Patran Analysis

Table F.1: Margins of Safety in OML Carbon Fuselage Panel

Direction	Layer	Stress (ksi)	MS
Longitudinal	2	5.07	4.92
Longitudinal	17	-6.32	3.22
Transverse	17	6.00	4.00
Transverse	13	-8.24	2.24
Shear	8	0.03696	2.39

Table F.2: Margins of Safety in Tested Quartz Ventilation Panel

Direction	Layer	Stress (ksi)	MS
Longitudinal	1	3.45	5.03
Longitudinal	12	-3.05	6.08
Transverse	2	2.99	5.69
Transverse	11	-2.94	5.26
Shear	11	0.88	4.08

Table F.3: Margins of Safety in Tested Quartz Design for 2 - 18 GHz Horn Antenna Bracket

Direction	Layer	Stress (ksi)	MS
Longitudinal	1	0.590	34.24
Longitudinal	12	-0.774	26.88
Transverse	2	0.851	22.50
Transverse	11	-0.281	64.47
Shear	11	0.181	23.68

Table F.4: Margins of Safety in Metallic Doublers for Tested Quartz Design

Max/Min	Stress (ksi)	MS
Max	10.163	2.94
Min	-9.021	3.10
shear	4.570	4.54

Table F.5: Margins of Safety in Metallic Shims for Tested Quartz Design

Max/Min	Stress (ksi)	MS
Max	1.870	17.72
Min	-0.687	48.49
shear	0.937	17.50

Table F.6: Fastener Loads for Tested Quartz Design

Bolt Number	Global Load			
	X (lbs.)	Y (lbs.)	Z(lbs.)	Max Shear(lb)
1	1.38	35.77	-6.21	36.3
2	200.2	580.2	28.7	613.5
3	-200.3	551.1	35.4	586.7
4	-189.6	385.4	-1.2	429.4
5	-2.6	213.8	0.5	213.8
6	-9.4	29.3	4.7	30.6
7	42.8	-2.6	0.4	42.9
8	182.1	-68.2	17.3	194.3
9	336.9	-236.7	47.2	412.6
10	271.0	-293.3	47.6	401.2
11	241.3	-329.4	47.5	410.4
12	202.4	-357.9	50.6	413.9
13	119.8	-383.1	52.6	404.8
14	99.7	-337.0	80.5	359.9
15	130.5	-211.2	95.1	261.3
16	169.5	-117.2	101.0	207.1
17	153.6	-37.0	92.0	120.4
18	46.6	5.3	37.3	59.8
19	69.9	8.0	4.1	70.4
20	62.3	6.5	-20.5	65.8
21	43.4	5.2	-24.7	50.1
22	21.6	3.5	-23.7	32.2
23	4.5	2.6	-20.4	20.9
24	-9.7	1.9	-17.1	19.6
25	-23.0	0.9	-13.1	26.3
26	-36.8	0.2	-3.6	36.9
27	-45.0	-0.7	15.8	47.6
28	-49.7	-2.4	37.7	62.1
29	-40.4	-6.7	49.9	50.4
30	-122.2	-38.2	77.8	97.0
31	-188.6	-99.6	95.6	189.2
32	-146.6	-182.5	106.4	244.5
33	-33.2	-277.4	91.9	293.5
34	78.4	-314.3	52.1	327.6
35	-5.7	-223.2	36.9	226.0
36	1.6	-166.7	27.3	168.5
37	23.0	-129.4	28.8	133.3

38	62.2	-55.1	19.8	83.6
39	144.7	51.1	7.0	152.9
40	165.7	198.3	3.0	258.0
41	237.1	284.6	-0.1	370.3
42	231.9	356.2	0.9	424.9
43	224.0	505.8	13.0	552.9
44	217.1	673.4	37.0	707.5
45	-17.2	648.3	65.2	651.3
46	-267.7	527.7	55.8	594.3
47	-518.5	435.5	43.6	673.9
48	-571.5	349.9	20.2	664.5
49	-155.5	151.9	-12.9	215.5
50	-237.2	147.2	-0.2	275.8
51	-253.1	47.5	14.6	254.7
52	-243.0	-72.3	32.2	253.4
53	-198.5	-197.7	49.7	283.7
54	-130.3	-338.6	70.7	369.6
55	-86.2	-440.8	83.8	456.8
56	20.4	-604.0	101.4	612.3
57	-18.5	-202.4	41.7	204.8
58	6.5	-118.1	14.5	118.9

The following is a sample calculation for the critical bearing margin of safety of the design sized with the tested quartz properties included in Section 3.4.7.

$$P_{\max shear \text{ Fastener } 2} = \sqrt{Fx^2 + Fy^2} = \sqrt{200.2^2 + 580.2^2} = 613.5 \text{ lbs}$$

$$MS_{bearing \text{ carbon}} = \frac{F_{bru} * d * t}{FF * FS * P_{shear}} - 1$$

$$MS_{bearing \text{ carbon Node 714, Fastener } 2} = \frac{40 \text{ ksi} * 0.1875 \text{ in.} * 0.1218 \text{ in.}}{1.15 * 1.5 * 613.5} - 1 = -0.14$$

Appendix G. Results for Reported Quartz Patran Analysis

Table G.1: Margins of Safety in OML Carbon Fuselage Panel

Direction	Layer	Stress (ksi)	MS
Longitudinal	2	5.295	4.67
Longitudinal	17	-6.32	3.22
Transverse	17	5.98	4.02
Transverse	13	-8.17	2.26
Shear	8	0.03706	2.38

Table G.2: Margins of Safety in Reported Quartz Ventilation Panel

Direction	Layer	Stress (ksi)	MS
Longitudinal	1	3.91	7.12
Longitudinal	12	-3.55	5.75
Transverse	2	4.54	5.81
Transverse	11	-3.54	5.97
Shear	11	0.999	5.61

Table G.3: Margins of Safety in Reported Quartz Design for 2 - 18 GHz Horn Antenna Bracket

Direction	Layer	Stress (ksi)	MS
Longitudinal	2	0.859	35.96
Longitudinal	8	-0.939	24.52
Transverse	2	1.55	18.94
Transverse	7	-0.232	105.35
Shear	7	0.202	31.67

Table G.4: Margins of Safety in Reported Quartz Design for Metallic Doublers

Type	Stress (ksi)	MS
Max	9.82	3.07
Min	-8.99	3.12
shear	4.59	4.52

Table G.5: Margins of Safety in Reported Quartz Design for Metallic Shims

Type	Stress (ksi)	MS
Max	1.78	18.66
Min	-0.638	52.29
shear	0.891	18.45

Table G.6: Fastener Loads for the Design sized with the Reported Quartz Properties

Bolt Number	Global Load			
	X (lbs.)	Y (lbs.)	Z (lbs.)	Max Shear(lb)
1	3.16	38.48	-6.59	39.1
2	210.1	584.6	29.4	620.9
3	-197.9	551.8	36.2	586.6
4	-192.1	389.6	-1.7	434.3
5	-8.1	218.4	0.5	218.4
6	-14.0	33.2	4.2	35.9
7	38.6	-1.5	0.1	38.6
8	174.4	-69.7	16.8	187.8
9	329.0	-234.4	46.7	404.8
10	268.2	-292.3	47.6	398.5
11	240.6	-330.2	47.6	410.7
12	202.3	-359.4	50.8	415.1
13	120.1	-384.5	52.7	406.2
14	100.3	-337.7	80.7	360.8
15	130.9	-211.4	95.1	261.7
16	169.8	-117.2	101.0	207.2
17	153.5	-36.9	91.8	120.2
18	46.5	5.3	37.2	59.7
19	69.7	7.9	4.0	70.3
20	62.2	6.5	-20.5	65.7
21	43.3	5.2	-24.7	50.0
22	21.6	3.5	-23.7	32.1
23	4.5	2.7	-20.4	20.9
24	-9.7	1.9	-17.2	19.6
25	-23.0	0.9	-13.1	26.3
26	-36.8	0.2	-3.7	36.8
27	-45.0	-0.7	15.8	47.5
28	-49.6	-2.4	37.7	62.1
29	-40.4	-6.7	49.9	50.4
30	-122.3	-38.2	77.8	97.0
31	-189.0	-99.6	95.7	189.4
32	-147.3	-182.7	106.5	244.9
33	-34.1	-277.8	92.1	294.0
34	77.3	-315.1	52.2	328.1
35	-6.5	-224.1	37.0	226.9
36	1.0	-167.5	27.4	169.4
37	22.4	-130.4	28.9	134.2

38	61.4	-56.1	19.9	83.6
39	144.0	50.0	7.1	151.8
40	165.1	197.1	3.1	256.7
41	236.9	283.5	-0.1	369.3
42	232.2	355.1	0.9	424.1
43	224.9	504.5	12.9	552.0
44	218.5	671.7	36.9	706.3
45	-15.5	646.6	64.9	649.5
46	-265.9	526.2	55.6	592.2
47	-515.9	434.0	43.4	671.0
48	-568.6	348.2	20.1	661.2
49	-154.5	151.0	-12.8	214.2
50	-235.5	145.7	-0.2	273.6
51	-251.1	46.0	14.7	252.6
52	-240.9	-73.9	32.3	251.8
53	-196.3	-199.0	49.8	283.2
54	-128.6	-339.3	70.7	369.6
55	-84.9	-440.4	83.7	456.2
56	21.4	-602.1	101.1	610.4
57	-16.0	-200.2	41.4	202.6
58	7.8	-115.1	14.2	115.9

The following is a sample calculation for the critical bearing margin of safety of the design sized with the reported quartz properties included in Section 3.4.7.

$$P_{\max shear Fastener 2} = \sqrt{Fx^2 + Fy^2} = \sqrt{210.1^2 + 584.6^2} = 620.9 \text{ lbs}$$

$$MS_{bearing carbon} = \frac{F_{bru} * d * t}{FF * FS * P_{shear}} - 1$$

$$MS_{bearing carbon Node 714, Fastener 2} = \frac{40 \text{ ksi} * 0.1875 \text{ in.} * 0.1218 \text{ in.}}{1.15 * 1.5 * 620.9} - 1 = -0.15$$

Appendix H. Results for Pre-Preg Glass Patran Analysis

Table H.1: Margins of Safety in OML Carbon Fuselage Panel

Direction	Layer	Stress (ksi)	MS
Longitudinal	2	5.3	4.66
Longitudinal	17	-6.31	3.23
Transverse	17	6	4.00
Transverse	13	-8.23	2.24
Shear	8	0.036948	2.39

Table H.2: Margins of Safety in Pre-Preg Fiberglass Ventilation Panel

Direction	Layer	Stress (ksi)	MS
Longitudinal	1	4.27	4.01
Longitudinal	12	-3.79	5.51
Transverse	2	3.75	4.48
Transverse	11	-3.77	4.59
Shear	11	0.982	5.25

Table H.3: Margins of Safety in Pre-Preg Fiberglass Design for 2 - 18 GHz Horn Antenna Bracket

Direction	Layer	Stress (ksi)	MS
Longitudinal	2	0.691	29.97
Longitudinal	12	-0.939	25.27
Transverse	2	1.06	18.37
Transverse	11	-0.314	66.09
Shear	11	0.197	30.13

Table H.4: Margins of Safety in Pre-Preg Fiberglass Design for Metallic Doublers

Type	Stress (ksi)	MS
Max	9.816	3.07
Min	-9.027	3.10
shear	4.6	4.51

Table H.5: Margins of Safety in Pre-Preg Fiberglass Design for Metallic Shims

Type	Stress (ksi)	MS
Max	1.93	17.13
Min	-0.787	42.20
shear	0.963	17.00

Table H.6: Fastener Loads for the Design sized with the Pre-Preg Fiberglass Properties

Bolt Number	Global Load			
	X (lbs.)	Y (lbs.)	Z (lbs.)	Max Shear(lb)
1	2.98	38.26	-6.55	38.9
2	206.5	584.0	29.8	619.2
3	-200.9	554.4	36.4	590.0
4	-192.2	393.2	-1.8	437.5
5	-5.1	220.4	0.4	220.4
6	-10.5	34.0	4.6	35.4
7	46.8	-2.5	0.3	46.8
8	188.6	-71.9	17.4	201.8
9	342.8	-246.3	47.8	423.0
10	271.5	-299.1	47.9	405.9
11	240.7	-332.3	47.6	412.4
12	201.7	-359.4	50.7	414.8
13	119.5	-383.9	52.7	405.4
14	99.7	-337.2	80.5	360.0
15	130.4	-211.1	95.0	261.2
16	169.4	-117.1	100.9	206.9
17	153.4	-36.9	91.8	120.2
18	46.5	5.3	37.3	59.7
19	69.7	7.9	4.1	70.3
20	62.2	6.5	-20.5	65.7
21	43.3	5.2	-24.6	50.0
22	21.5	3.5	-23.7	32.1
23	4.5	2.6	-20.3	20.8
24	-9.7	1.9	-17.1	19.6
25	-23.0	0.9	-13.1	26.3
26	-36.8	0.2	-3.6	36.9
27	-45.0	-0.7	15.8	47.6
28	-49.7	-2.4	37.7	62.1
29	-40.4	-6.7	49.9	50.4
30	-122.2	-38.2	77.8	97.0
31	-188.8	-99.6	95.6	189.3
32	-146.9	-182.6	106.4	244.7
33	-33.8	-277.7	92.0	293.8
34	77.6	-314.9	52.2	328.0
35	-6.5	-223.9	36.9	226.6
36	0.8	-167.4	27.4	169.3
37	22.0	-130.4	28.9	134.1

38	60.6	-56.2	19.9	83.1
39	142.7	49.7	7.1	150.5
40	162.7	196.8	3.1	254.9
41	234.0	283.7	0.0	367.6
42	229.0	355.5	1.0	422.7
43	221.1	505.1	13.0	551.1
44	214.5	673.4	37.1	706.7
45	-18.5	648.8	65.3	651.8
46	-268.2	528.0	55.8	594.7
47	-518.4	435.5	43.6	673.9
48	-570.8	349.6	20.2	663.8
49	-155.2	151.7	-12.9	215.1
50	-236.6	146.6	-0.2	275.0
51	-252.3	46.8	14.7	253.9
52	-242.1	-73.3	32.3	252.8
53	-197.5	-198.7	49.8	283.8
54	-129.6	-339.2	70.8	369.9
55	-85.8	-440.3	83.7	456.2
56	20.7	-602.2	101.1	610.4
57	-16.2	-199.5	41.4	201.9
58	7.4	-114.8	14.1	115.6

The following is a sample calculation for the critical bearing margin of safety of the design sized with the pre-preg fiberglass properties included in Section 3.4.7.

$$P_{\max shear \text{ Fastener } 2} = \sqrt{Fx^2 + Fy^2} = \sqrt{206.5^2 + 584.0^2} = 619.2 \text{ lbs}$$

$$MS_{bearing \text{ carbon}} = \frac{F_{bru} * d * t}{FF * FS * P_{shear}} - 1$$

$$MS_{bearing \text{ carbon Node 714, Fastener } 2} = \frac{40 \text{ ksi} * 0.1875 \text{ in.} * 0.1218 \text{ in.}}{1.15 * 1.5 * 619.2} - 1 = -0.15$$

Appendix I. Results for Sandwich Fiberglass Patran Analysis

Table I.1: Margins of Safety in OML Carbon Fuselage Panel

Direction	Layer	Stress (ksi)	MS
Longitudinal	2	5.89	4.09
Longitudinal	17	-6.36	3.19
Transverse	17	5.94	4.05
Transverse	13	-7.11	2.75
Shear	8	0.0375	2.34

Table I.2: Margins of Safety in Sandwich Ventilation Panel

Direction	Layer	Stress (ksi)	MS
Longitudinal	1	9.01	0.74
Longitudinal	12	-6.05	1.75
Transverse	2	7.01	1.04
Transverse	11	-7.89	1.11
Shear	11	1.81	3.97
Shear	3	0.0143	7.76

Table I.3: Margins of Safety in Sandwich Design for 2 - 18 GHz Horn Antenna Bracket

Direction	Layer	Stress (ksi)	MS
Longitudinal	2	2.13	6.36
Longitudinal	1	-1.03	15.18
Transverse	2	3.53	3.06
Transverse	11	-0.635	25.25
Shear	11	0.336	25.79

Table I.4: Margins of Safety in Sandwich Design for Metallic Doublers

Type	Stress (ksi)	MS
Max	8.83	3.53
Min	-9.106	3.06
shear	4.65	4.45

Table I.5: Margins of Safety in Sandwich Design for Metallic Shims

Type	Stress (ksi)	MS
Max	1.815	18.28
Min	-1.165	28.18
shear	0.908	18.09

Table I.6: Fastener Loads for Sandwich Design

Bolt Number	Global Load			
	X (lbs.)	Y (lbs.)	Z (lbs.)	Max Shear(lb)
1	6.81	42.70	-7.18	43.8
2	237.3	587.3	29.9	633.0
3	-186.6	538.9	37.9	570.6
4	-195.4	387.3	-0.8	433.7
5	-29.8	217.9	2.6	219.9
6	-42.9	31.0	6.1	52.8
7	-1.5	6.5	1.9	6.6
8	130.7	-54.1	17.0	141.5
9	309.7	-212.7	44.7	376.5
10	261.3	-278.5	46.8	383.7
11	239.9	-323.5	47.2	404.8
12	203.8	-357.0	50.7	413.7
13	121.7	-384.3	52.8	406.5
14	102.0	-338.7	81.0	362.2
15	132.3	-212.3	95.6	263.1
16	171.0	-117.6	101.4	208.3
17	154.1	-37.0	92.1	120.6
18	46.6	5.3	37.3	59.8
19	69.8	8.0	4.0	70.4
20	62.3	6.5	-20.7	65.9
21	43.4	5.3	-24.9	50.2
22	21.7	3.6	-23.9	32.3
23	4.6	2.7	-20.5	21.0
24	-9.6	1.9	-17.3	19.6
25	-22.9	1.0	-13.2	26.3
26	-36.7	0.3	-3.8	36.7
27	-44.8	-0.6	15.7	47.3
28	-49.5	-2.4	37.7	62.0
29	-40.3	-6.7	49.9	50.4
30	-122.3	-38.2	77.7	97.0
31	-189.6	-99.7	95.7	189.7
32	-148.3	-183.0	106.7	245.7
33	-35.4	-278.8	92.4	295.2
34	76.4	-317.0	52.5	329.8
35	-6.6	-226.3	37.2	229.1
36	1.2	-169.6	27.6	171.5
37	23.1	-132.6	29.1	136.6

38	62.5	-58.4	20.0	86.0
39	146.3	48.1	7.2	153.4
40	169.3	195.1	3.1	257.9
41	242.4	281.3	-0.2	371.1
42	238.7	353.2	0.8	426.1
43	233.1	502.8	12.7	553.9
44	227.9	669.2	36.5	706.9
45	-8.0	643.8	64.5	646.6
46	-260.4	523.7	55.2	587.4
47	-508.8	431.2	42.9	663.7
48	-561.0	344.2	19.9	652.6
49	-151.8	148.5	-12.6	210.5
50	-230.5	141.4	0.1	267.2
51	-245.2	40.8	15.1	246.0
52	-234.1	-79.8	32.7	247.5
53	-189.6	-204.8	50.2	282.8
54	-122.7	-343.2	70.9	371.2
55	-80.3	-441.2	83.4	456.0
56	24.9	-598.3	100.3	606.6
57	-10.5	-198.5	40.7	200.8
58	12.1	-111.2	13.8	112.4

The following is a sample calculation for the critical bearing margin of safety of the sandwich design sized with pre-preg fiberglass included in Section 3.4.7.

$$P_{\max shear \text{ Fastener } 2} = \sqrt{F_x^2 + F_y^2} = \sqrt{237.3^2 + 587.3^2} = 633 \text{ lbs}$$

$$MS_{bearing \text{ carbon}} = \frac{F_{bru} * d * t}{FF * FS * P_{shear}} - 1$$

$$MS_{bearing \text{ carbon Node 714, Fastener } 2} = \frac{40 \text{ ksi} * 0.1875 \text{ in.} * 0.1218 \text{ in.}}{1.15 * 1.5 * 633} - 1 = -0.16$$

Appendix J. Tested Quartz MCoRDS Patran Analysis

Table J.1: Margins of Safety in MCoRDS Radome Panel under Load Case 2

Direction	Layer	Stress (ksi)	MS
Longitudinal	23	6.38	1.48
Longitudinal	2	-3.88	2.95
Transverse	23	9.17	0.42
Transverse	1	-7.01	0.60
Shear	15	0.104	25.14

Table J.2: Margins of Safety in Rib Structure under Load Case 2

Direction	Layer	Stress (ksi)	MS
Longitudinal	1	2.367	5.68
Longitudinal	13	-1.29	10.89
Transverse	2	2.039	5.40
Transverse	14	-1.32	7.48
Shear	14	0.269	9.11

Table J.3: Margins of Safety in MCoRDS Radome Panel under Load Case 3

Direction	Layer	Stress (ksi)	MS
Longitudinal	23	8.48	1.45
Longitudinal	2	-4.82	3.48
Transverse	23	9.52	1.10
Transverse	1	-9.64	0.91
Shear	1	0.203	21.00

Table J.4: Margins of Safety in Rib Structure under Load Case 3

Direction	Layer	Stress (ksi)	MS
Longitudinal	2	3.49	4.96
Longitudinal	14	-3.93	4.49
Transverse	2	3.86	4.18
Transverse	14	-4.15	3.43
Shear	13	0.5556	7.04

Appendix K. Reported Quartz MCoRDS Patran Analysis

Table K.1: Margins of Safety in MCoRDS Radome Panel under Load Case 2

Direction	Layer	Stress (ksi)	MS
Longitudinal	23	7.43	2.25
Longitudinal	2	-4.86	2.50
Transverse	23	10.6	0.90
Transverse	1	-8.21	0.91
Shear	1	1.025	2.92

Table K.2: Margins of Safety in Rib Structure under Load Case 2

Direction	Layer	Stress (ksi)	MS
Longitudinal	1	2.56	8.43
Longitudinal	13	-1.52	10.21
Transverse	2	2.33	7.66
Transverse	14	-1.62	8.69
Shear	14	0.288	12.95

Table K.3: Margins of Safety in MCoRDS Radome Panel under Load Case 3

Direction	Layer	Stress (ksi)	MS
Longitudinal	23	9.89	2.21
Longitudinal	2	-5.46	3.39
Transverse	23	11.1	1.78
Transverse	1	-11.3	1.18
Shear	1	1.95	2.38

Table K.4: Margins of Safety in Rib Structure under Load Case 3

Direction	Layer	Stress (ksi)	MS
Longitudinal	2	4.1	6.74
Longitudinal	14	-4.62	4.19
Transverse	2	4.46	5.93
Transverse	14	-4.89	4.05
Shear	13	0.62	9.59